

AD-A162 467

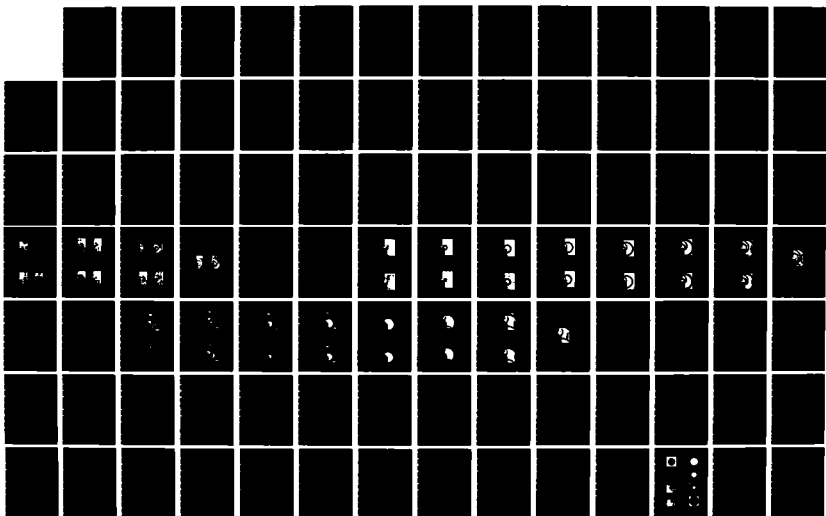
GROUND RESPONSE IN ALLUVIAL BASINS DUE TO SEISMIC
DISTURBANCES(U) COLUMBIA UNIV NEW YORK J T KUO ET AL.
MAR 85 AFGL-TR-85-0062 F19628-81-K-0012

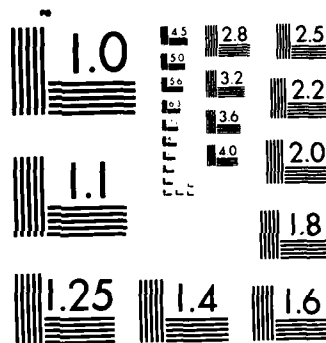
1/2

UNCLASSIFIED

F/G 8/11

NL





MICROCOPY RESOLUTION TEST CHART
NATIONAL BUREAU OF STANDARDS-1963-A

AFGL-TR-85-0062

GROUND RESPONSE IN ALLUVIAL BASINS
DUE TO SEISMIC DISTURBANCES

AD-A162 467

John T. Kuo
Yu-Chiung Teng

Columbia University
New York, NY 10027

March 1985

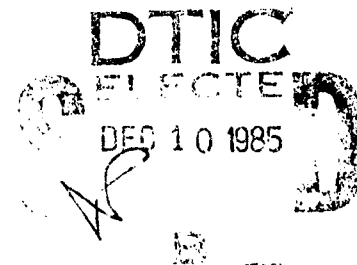
FINAL REPORT

Period Covered : March 1981 ~ September 1984

Approved for public release
distribution unlimited

DTIC FILE COPY


AIR FORCE GEOPHYSICS LABORATORY
AIR FORCE SYSTEMS COMMAND
UNITED STATES AIR FORCE
HANSCOM AFB, MASSACHUSETTS 01731




85 12 -9 074

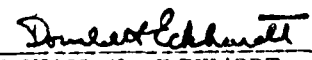
CONTRACTOR REPORTS

This technical report has been reviewed and is approved for publication.


JAMES C. BATTIS
Contract Manager


HENRY A. COSSING
Chief, Solid Earth Geophysics Branch

FOR THE COMMANDER


DONALD H. ECKHARDT
Director
Earth Sciences Division

This report has been reviewed by the ESD Public Affairs Office (PA) and is releasable to the National Technical Information Service (NTIS).

Qualified requesters may obtain additional copies from the Defense Technical Information Center. All others should apply to the National Technical Information Service.

If your address has changed, or if you wish to be removed from the mailing list, or if the addressee is no longer employed by your organization, please notify AFGL/DAA, Hanscom AFB, MA 01731. This will assist us in maintaining a current mailing list.

Unclassified

SECURITY CLASSIFICATION OF THIS PAGE

10. 416-2467

REPORT DOCUMENTATION PAGE

1a. REPORT SECURITY CLASSIFICATION Unclassified		1b. RESTRICTIVE MARKINGS	
2a. SECURITY CLASSIFICATION AUTHORITY		3. DISTRIBUTION/AVAILABILITY OF REPORT Approved for public release; distribution unlimited	
2b. DECLASSIFICATION/DOWNGRADING SCHEDULE		5. MONITORING ORGANIZATION REPORT NUMBER(S) AFGL-TR-85-0062	
4. PERFORMING ORGANIZATION REPORT NUMBER(S)		7a. NAME OF MONITORING ORGANIZATION	
6a. NAME OF PERFORMING ORGANIZATION Columbia University in the City of New York	6b. OFFICE SYMBOL (If applicable)	7b. ADDRESS (City, State and ZIP Code)	
6c. ADDRESS (City, State and ZIP Code) New York, NY 10027		9. PROCUREMENT INSTRUMENT IDENTIFICATION NUMBER F19628-81-K-0012	
8a. NAME OF FUNDING/SPONSORING ORGANIZATION Air Force Geophysics Laboratory	8b. OFFICE SYMBOL (If applicable)	10. SOURCE OF FUNDING NOS.	
8c. ADDRESS (City, State and ZIP Code) Hanscom AFB, MA 01731		PROGRAM ELEMENT NO. 61102F	PROJECT NO. 2309
11. TITLE (Include Security Classification) Ground Response in Alluvial Basins Due to Seismic Disturbances		TASK NO. G2	WORK UNIT NO. AH
12. PERSONAL AUTHOR(S) John T. Kuo and Yu-Chiung Teng			
13a. TYPE OF REPORT Final Report	13b. TIME COVERED FROM Mar. 1981 to Sept. 1984	14. DATE OF REPORT (Yr., Mo., Day) 1985 March	15. PAGE COUNT 170
16. SUPPLEMENTARY NOTATION This final report summarizes the scientific accomplishments of the present contract for the duration of three years. The accomplishments include four parts: (1) Five preliminary basin models for SH-waves and three for elastic (P and SV) waves have been studied using the finite element method. The results of these problems are presented either by synthetic seismograms or by snapshots; (2) Modification and improvement of the two dimensional finite element computer codes. Particular attention has been addressed to save computer in-core storage and computing time; (3) Development of a new finite element technique to simulate different types of seismic sources. An example of demonstrating the difference in waveforms due to different types of source is appended; (4) A detailed description and User's Guide for the two-dimensional elastodynamic finite element computer program developed at Aldridge and adapted to the VAX 11 computer at AFGL is provided.			
17. COSATI CODES		18. SUBJECT TERMS (Continue on reverse if necessary and identify by block number)	
FIELD	GROUP	SUB. GR.	
		Seismic Basins, Finite element modeling, Wave propagation, Source simulation.	
19. ABSTRACT (Continue on reverse if necessary and identify by block number) This final report summarizes the scientific accomplishments of the present contract for the duration of three years. The accomplishments include four parts: (1) Five preliminary basin models for SH-waves and three for elastic (P and SV) waves have been studied using the finite element method. The results of these problems are presented either by synthetic seismograms or by snapshots; (2) Modification and improvement of the two dimensional finite element computer codes. Particular attention has been addressed to save computer in-core storage and computing time; (3) Development of a new finite element technique to simulate different types of seismic sources. An example of demonstrating the difference in waveforms due to different types of source is appended; (4) A detailed description and User's Guide for the two-dimensional elastodynamic finite element computer program developed at Aldridge and adapted to the VAX 11 computer at AFGL is provided.			
20. DISTRIBUTION/AVAILABILITY OF ABSTRACT UNCLASSIFIED/UNLIMITED <input checked="" type="checkbox"/> SAME AS RPT. <input type="checkbox"/> DTIC USERS <input type="checkbox"/>		21. ABSTRACT SECURITY CLASSIFICATION Unclassified	
22a. NAME OF RESPONSIBLE INDIVIDUAL James C. Battis	22b. TELEPHONE NUMBER (Include Area Code) 617-861-3222	22c. OFFICE SYMBOL LWH	

TABLE OF CONTENTS

	<u>PAGE</u>
INTRODUCTION	1
SCIENTIFIC ACCOMPLISHMENTS	4
I. FINITE ELEMENT MODELING OF BASINS WITH DISPLAY OF SYNTHETIC SEISMOGRAMS	4
(1) SIMPLE MODELS FOR SH WAVES	4
(2) SIMPLE MODELS FOR ELASTIC WAVES (P & SV WAVES)	22
II. FINITE ELEMENT MODELING OF BASINS WITH DISPLAY OF SNAPSHOTS	35
III. MODIFICATION AND IMPROVEMENT OF TWO DIMENSIONAL FINITE ELEMENT COMPUTER CODES	60
(1) NON-REFLECTING BOUNDARIES	60
(2) EFFECTIVE EXCITATION (EE) METHOD	78
(3) INTRODUCING RELATIVE COORDINATES OF THE NODAL POINTS	80
(4) RESTART/BACK-UP OPTION	81
(5) AVERAGING 2CST FORMULATION	83
(6) NODAL-POINT-ORIENTED APPROACH	85

IV. FINITE ELEMENT SOURCE SIMULATION	86
(1) ONE DEGREE-OF-FREEDOM SH-WAVE PROBLEM	88
(2) TWO DEGREE-OF-FREEDOM ELASTIC WAVE PROBLEM	93
(3) REMARKS FOR THE FINITE ELEMENT SOLUTIONS	115
(4) DEMONSTRATION OF THE WAVEFORMS STRONGLY DEPENDS ON THE NATURE OF THE SOURCE	121
V. TWO-DIMENSIONAL FINITE ELEMENT COMPUTER PROGRAM FOR ELASTODYNAMIC PORBLEMS (THE USER'S GUIDE) ...	122
(1) FORMULATION	122
(2) PROGRAM DISCRIPTION	128
(3) MULTILAYERED MESH GENERATION	130
(4) GUIDE FOR DATA INPUT	134
(5) DEFINITION OF OTHER MAJOR VARIABLES	136
(6) FLOW CHARTS OF MAIN PROGRAM AND SUBROUTINES ...	137
APPENDIX A	145
ACKNOWLEDGEMENT	165
REFERENCES	166

INTRODUCTION

Under the present Air Force Contract F19628-81-K-0012, "Ground Response in Alluvial Basins Due to Seismic Disturbances", the accomplishments of the contract are:

(I) Five preliminary basin models for SH-waves and three for elastic (P and SV) waves have been studied using the finite element method. The results of these problems are presented either by the conventional synthetic seismograms or by the detailed snapshots of the wave fields. These results should give the effects of the basin and range like structure on wave scattering, diffraction, and propagation.

(II) The problem of undesired reflections and diffractions from artificially terminated boundaries in the finite element modeling has been re-investigated. A non-reflecting-boundary is implemented. By using this type of boundary, artificial reflections can be eliminated completely, before a given wave is reflected at that same boundary more than once.

(III) A new finite element technique has been successfully developed to simulate different types of earthquake and explosive source mechanisms, including the following cases:

(1) One Degree of Freedom SH-wave Problems with:

- (a) a concentrated line source,
 - (b) a concentrated coupled line source.
- (2) Two Degrees of Freedom Elastic-Wave (P and SV)
Problems with:

- (a) a directional-force line source,
- (b) an omni-directional line source,
- (c) a single-couple-without-moment line source,
- (d) a single-couple-with-moment line source,
- (e) a double-couple line source.

(IV) The two-dimensional element-oriented finite element codes for the cases of elastic (P and SV-wave) and SH-wave have been modified and improved by:

- (1) implementing the Effective Excitation (EE) method,
- (2) introducing the relative coordinates of the nodal points,
- (3) introducing the restart and back-up capability, and
- (4) replacing the 4CST(Four Constant Strain Triangles) algorithm instead of using the Averaging 2CST algorithm.

(V) The two-dimensional nodal-point-oriented finite

element codes for the case of elastic waves has been developed. By using this new version, a large amount of computing time can be saved.

(VI) The element-oriented finite element codes for the cases of elastic waves and SH wave, which were originally written for PRIME 750, have been adapted to VAX 11/780 at AFGL.

DTIC
ELECTE
DEC 10 1985

B



A-1

SCIENTIFIC ACCOMPLISHMENTS

I. FINITE ELEMENT MODELING OF BASINS WITH DISPLAY OF SYNTHETIC SEISMOGRAMS

(1) SIMPLE MODELS FOR SH WAVES

The following three simple basin models for SH waves have been investigated.

(a) Model 1:

At the suggestion of Mr. J. Battis at AFGL, we first model an homogeneous truncated medium as shown in Figure 1, with 500 quadrilateral finite elements. The model assumes shear velocity $v_s = 2,900$ m/sec, density $\rho = 2.67$ gm/cm³; grid size $\Delta x = \Delta y = 85$ m. A uniform SH wave forcing function of the first derivative of a Gaussian function (Figure 2) is loaded on the lower boundary AA' of the medium.

The synthetic seismograms of the displacement u along the vertical planes OA and BC, with a sampling space $x = 425$ m and time step $t = 0.02$ sec, are shown in Figures 3 and 4. These two seismogram-vertical profiles are exactly identical. Figures 5 and 6 show the identical responses along the horizontal surfaces OO' and MM'. As expected, all of these responses due to a uniform external SH forcing function along AA', are identical and assure the correctness of the finite element results. In Figures 3 and 4, the arrivals of the direct and reflected pulses from AA' and OO' can be clearly identified.

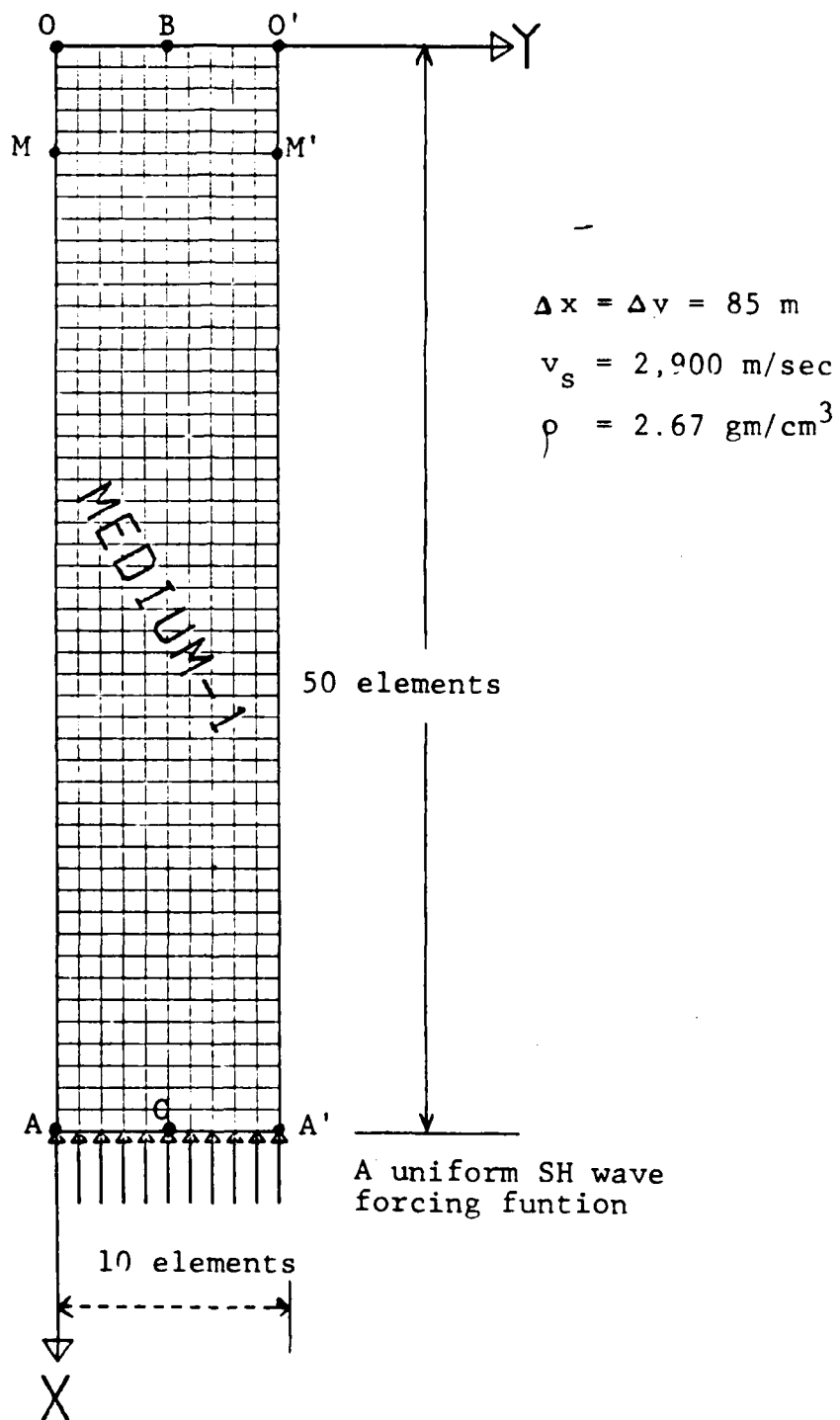


Figure 1. Finite Element Model 1.

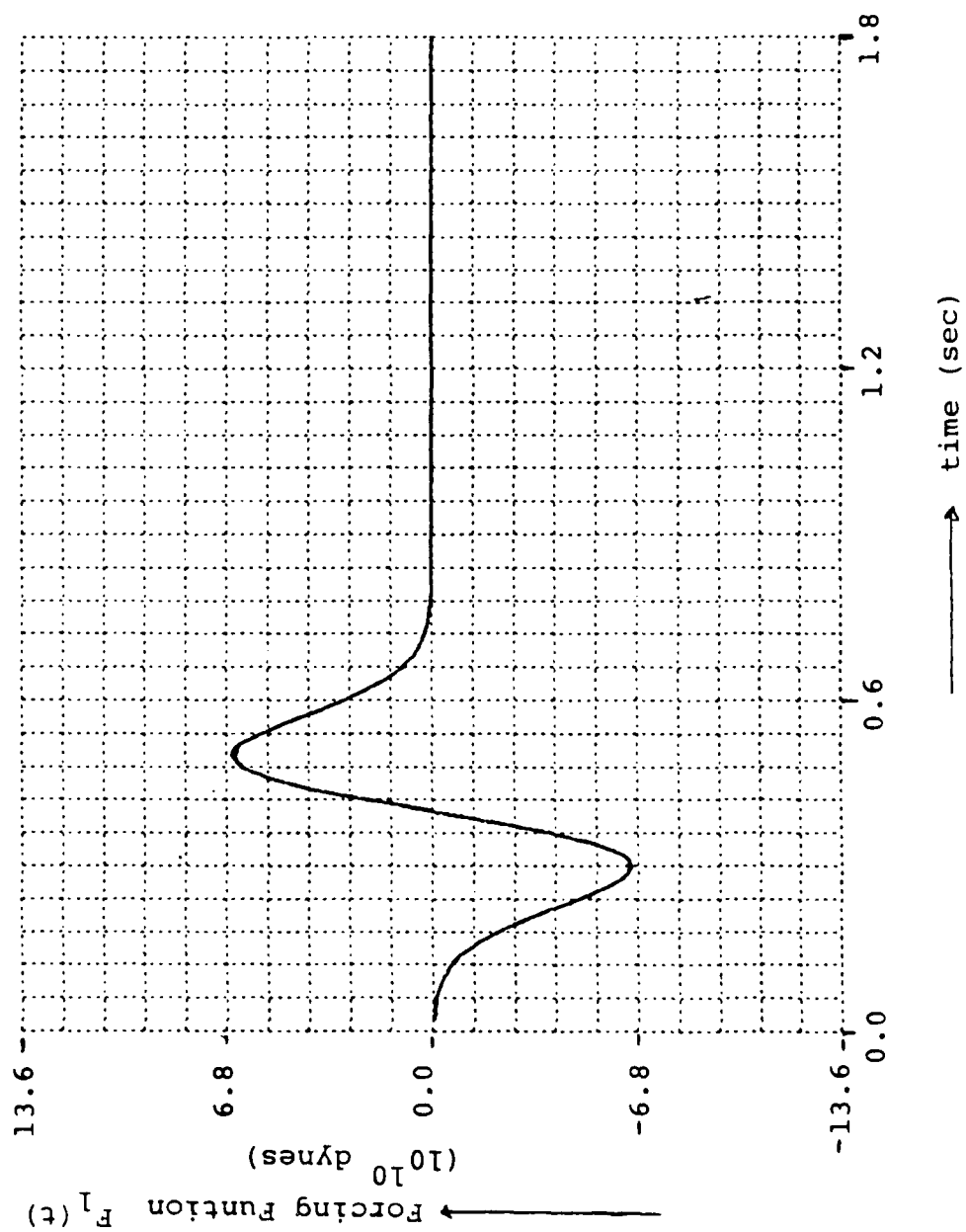


Figure 2. Source Function for SH-Wave Cases.

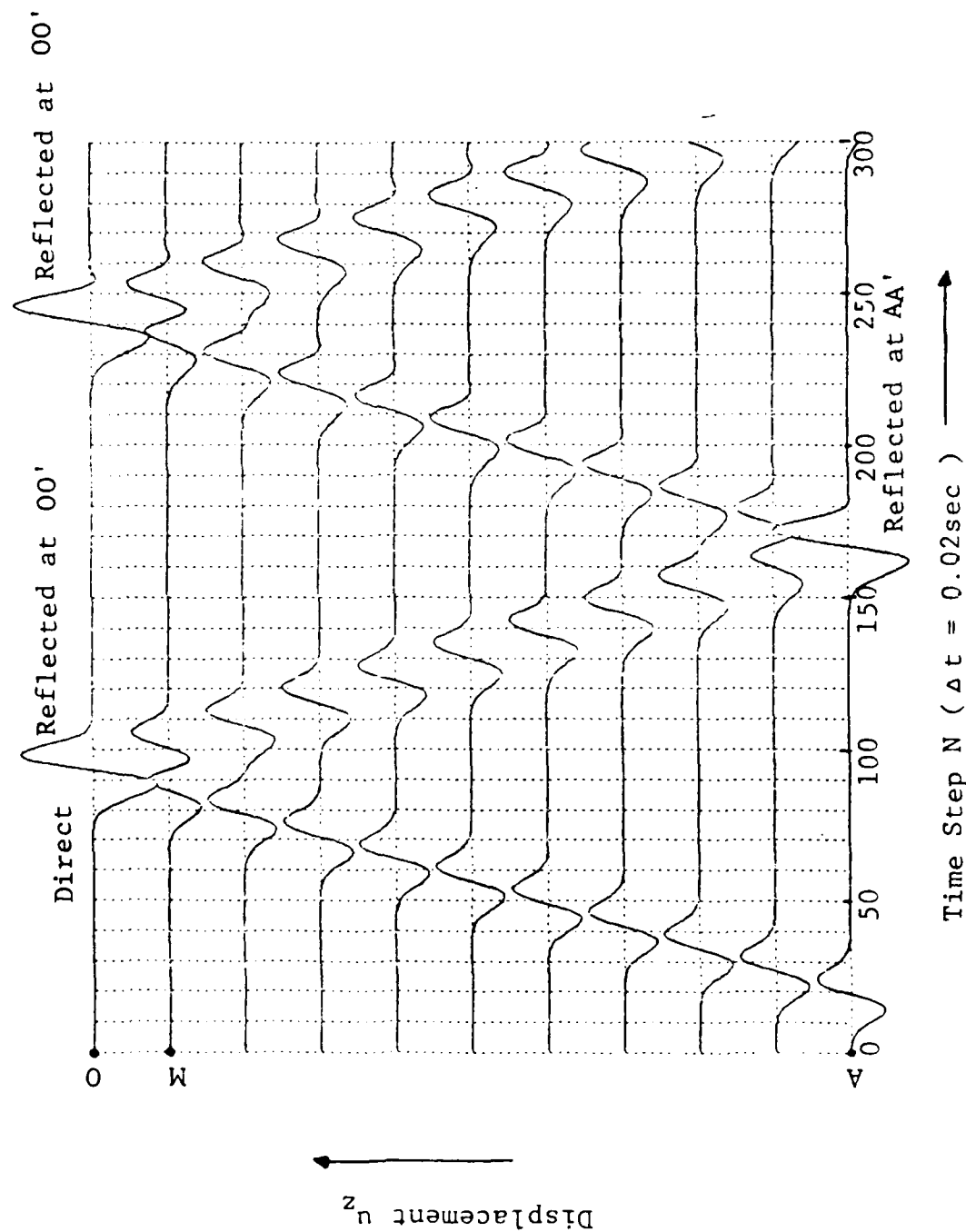


Figure 3. Synthetic Seismogram Along Vertical Plane OA For Model 1.

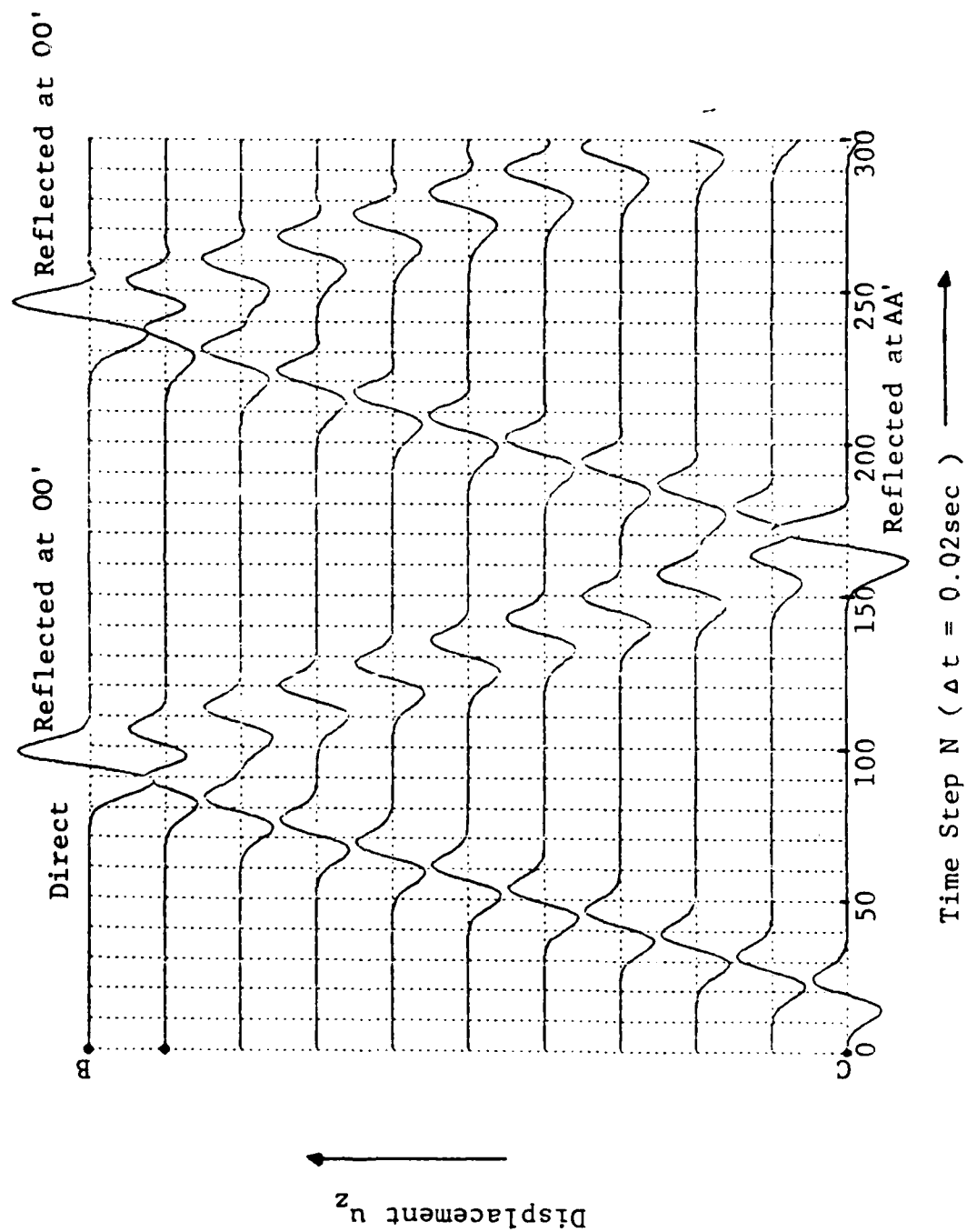


Figure 4. Synthetic Seismogram Along Vertical Plane BC For Model 1.

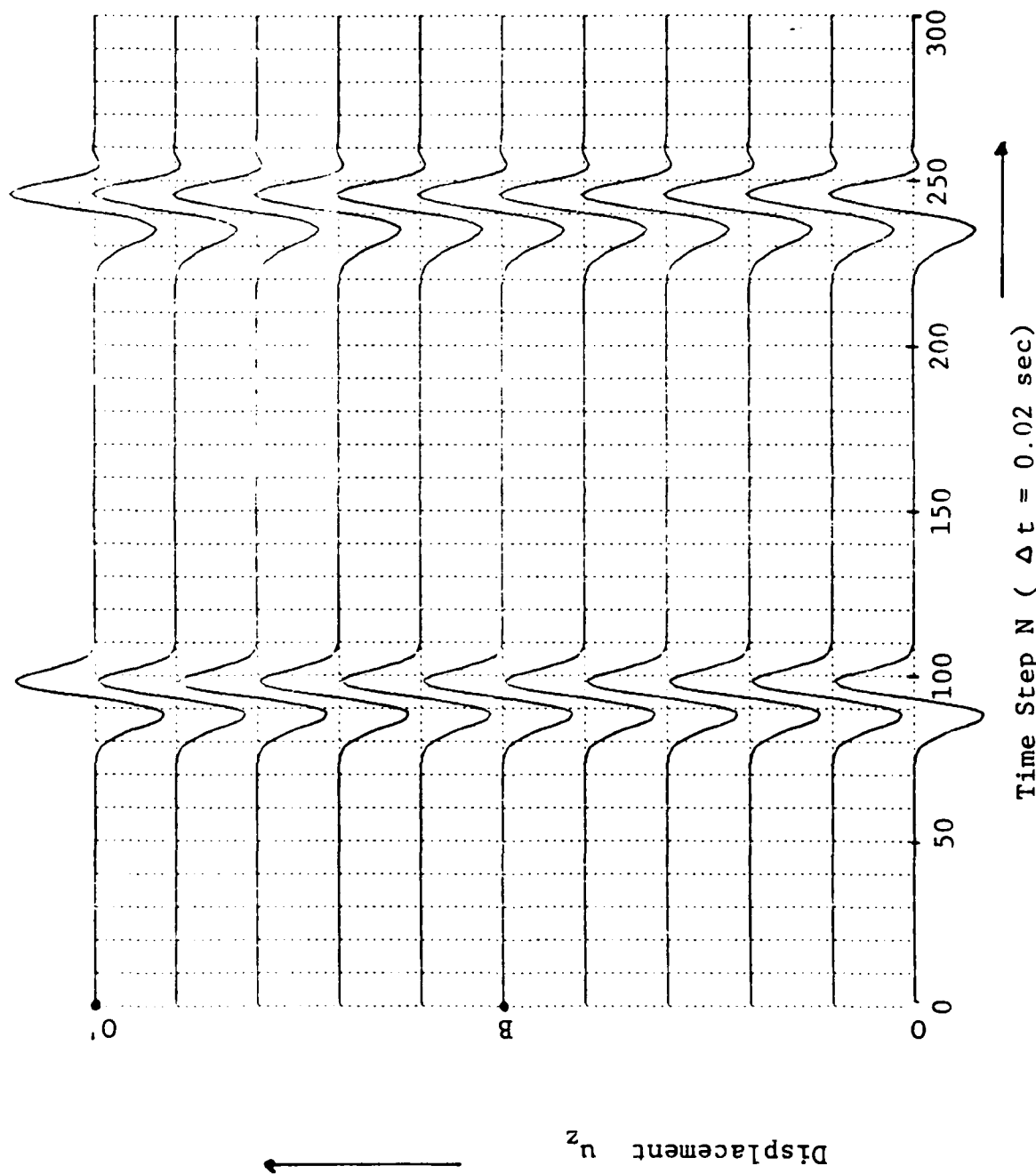


Figure 5. Synthetic Seismogram Along Free Surface 00' For Model 1.

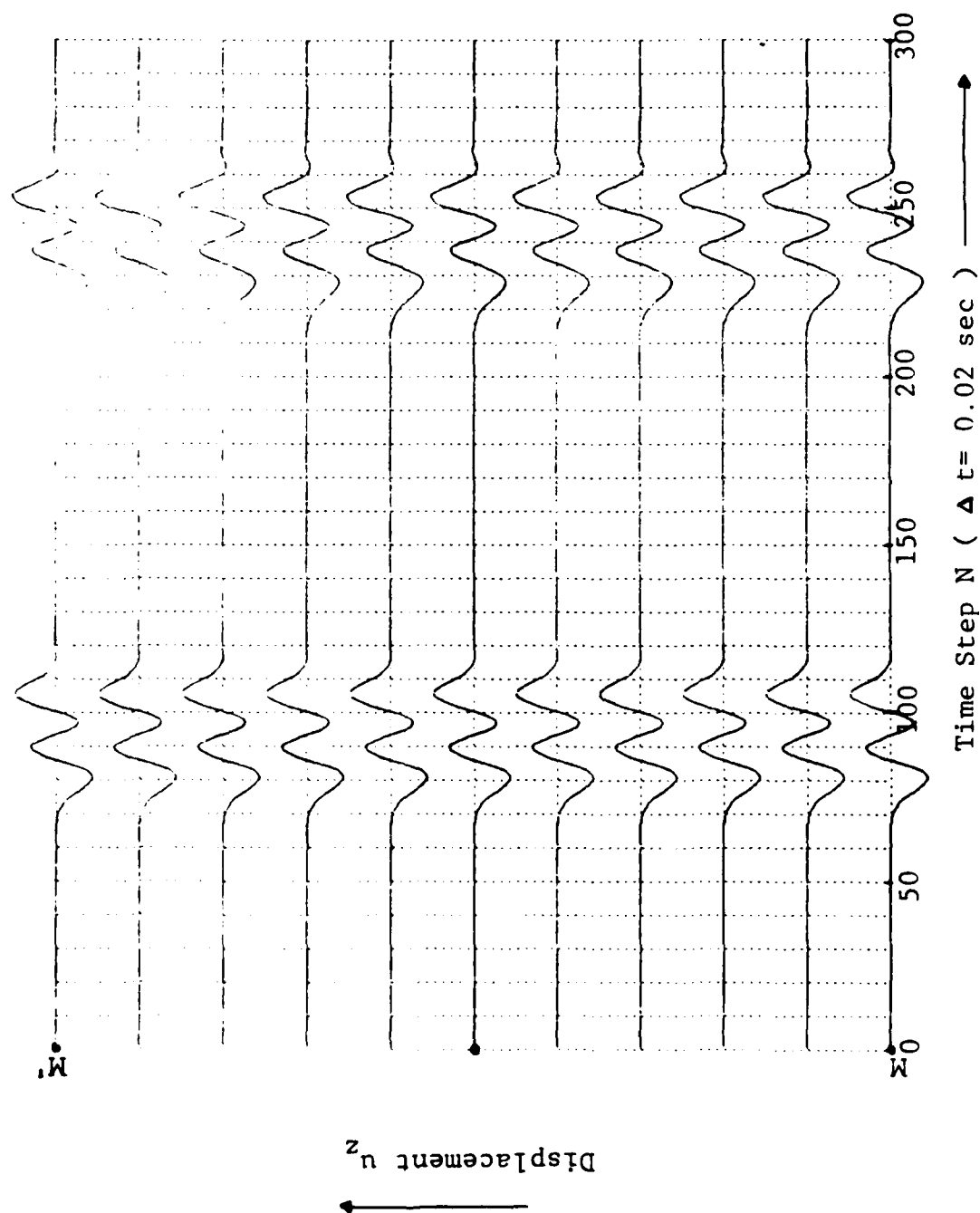


Figure 6. Synthetic Seismogram Along Horizontal Surface MM' For Model 1.

(b) Model 2:

The exact same model as (a) above, except the upper left corner of 25 elements of medium 1 is replaced by medium 2, with a shear wave velocity, $v_{s2} = 1,750$ m/sec, and density $\rho_2 = 2.4$ gm/cm³ (Figure 7). The excitation function is identical to that in Model 1.

Figures 8 and 9 show the complex results of the displacement u_z along the vertical planes OA and BC. The inclusion of medium 2 introduces a great deal of complexity of the waves. In Figures 8 and 9, the arrivals of the direct waves and first reflections from the free surface OO' are still identifiable; however, the diffracted waves and multi-reflected waves in medium 2 give the complex waveforms of the reflected waves at OO'; the reflected waves from AA' are distorted. As expected, the responses of the displacements u_z along any horizontal surfaces are no longer identical as compared with the situation in Figure 6. Figures 10 and 11 are the synthetic seismograms along the horizontal surfaces OO' and MM'.

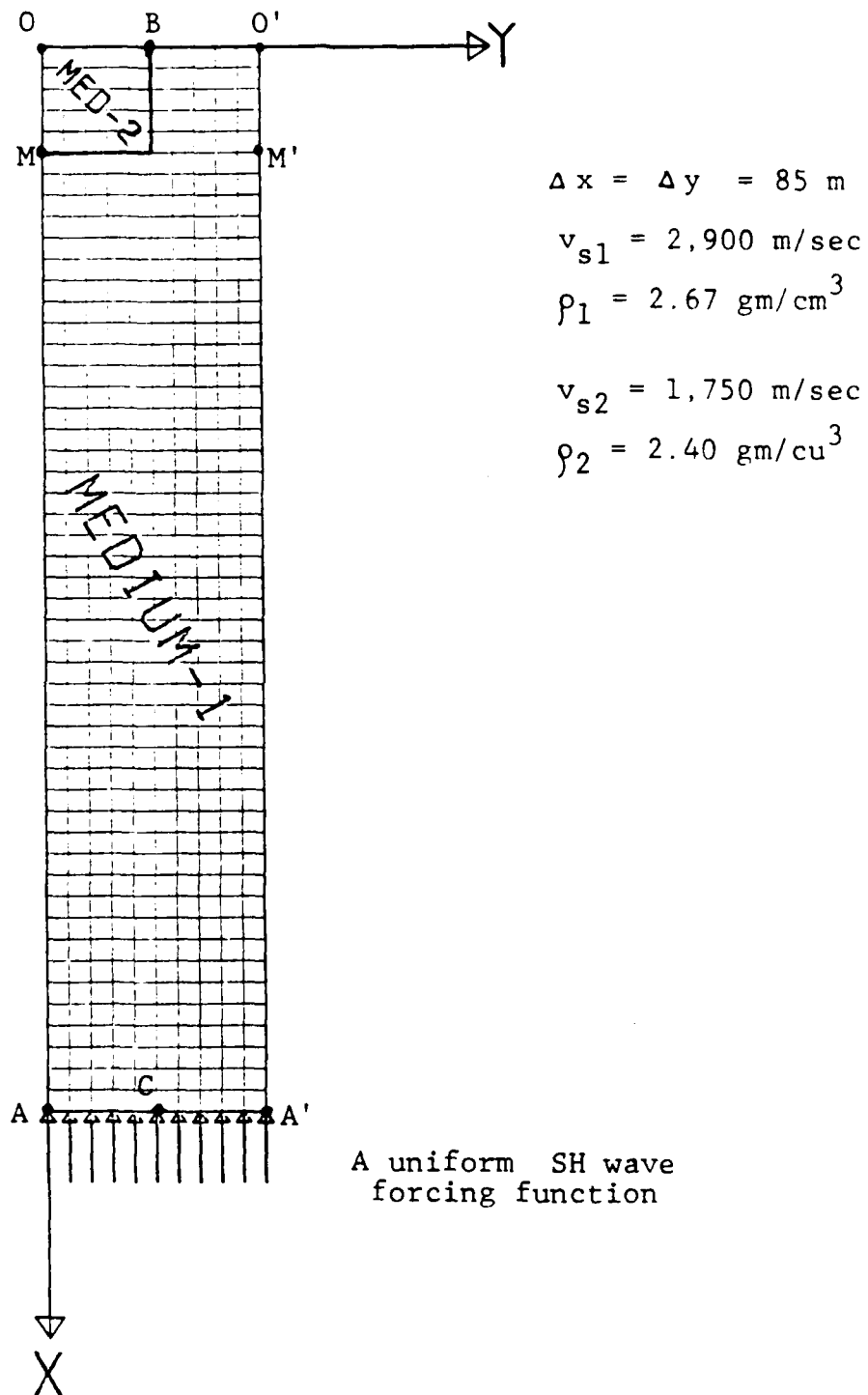


Figure 7. Finite Element Model 2.

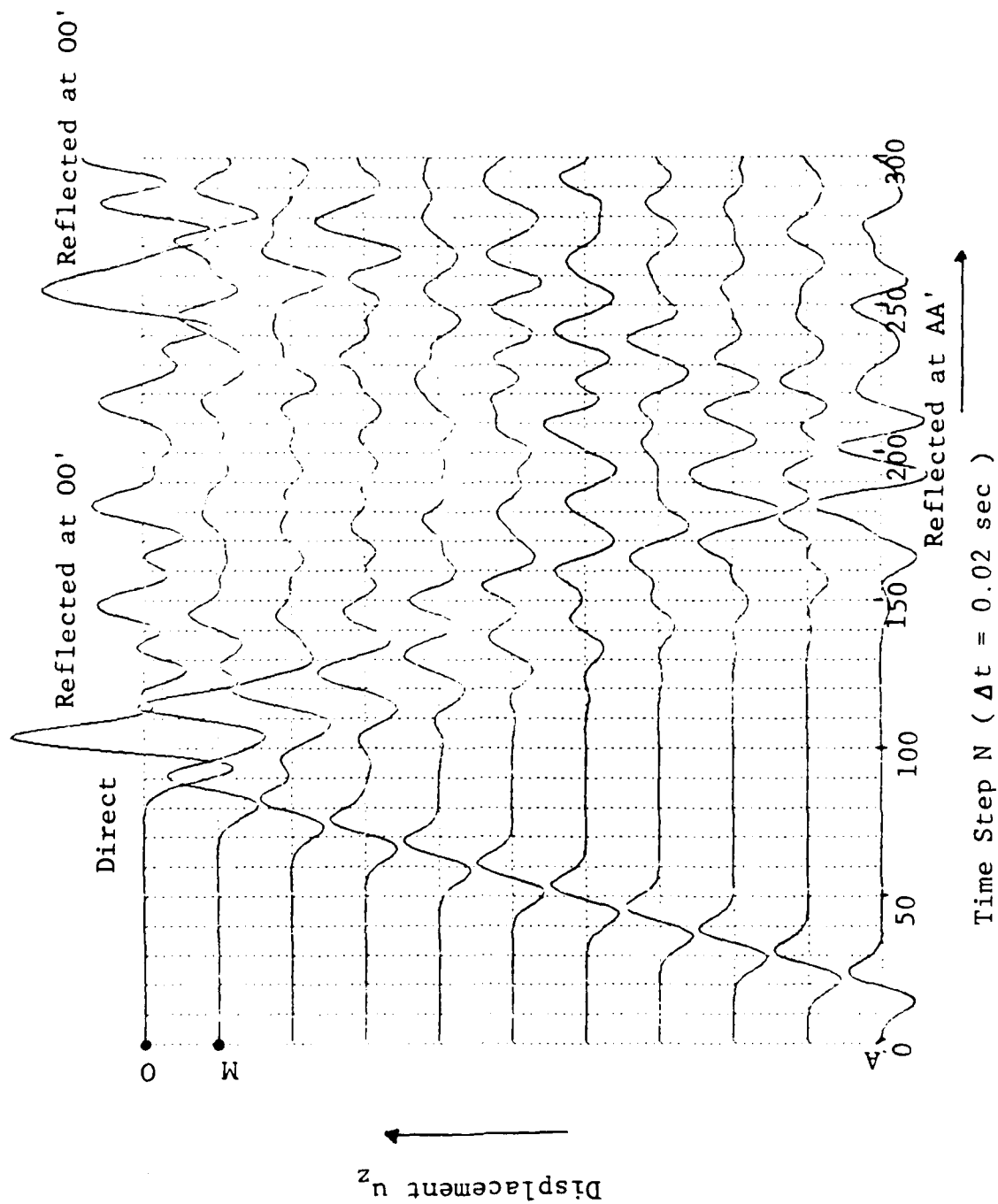


Figure 8. Synthetic Seismogram Along Vertical Plane OA for Model 2.

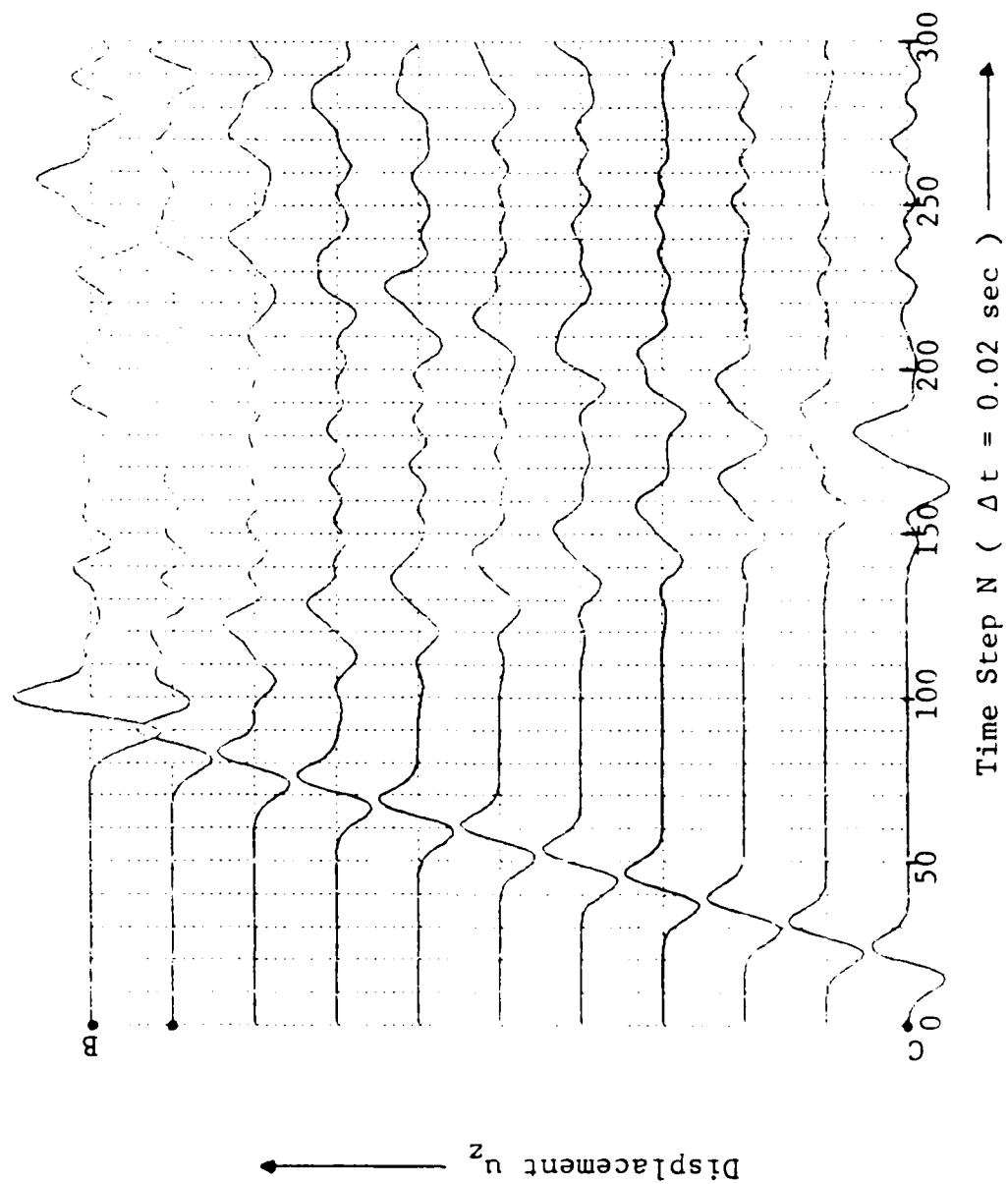


Figure 9. Synthetic Seismogram Along Vertical Plane BC For Model 2.

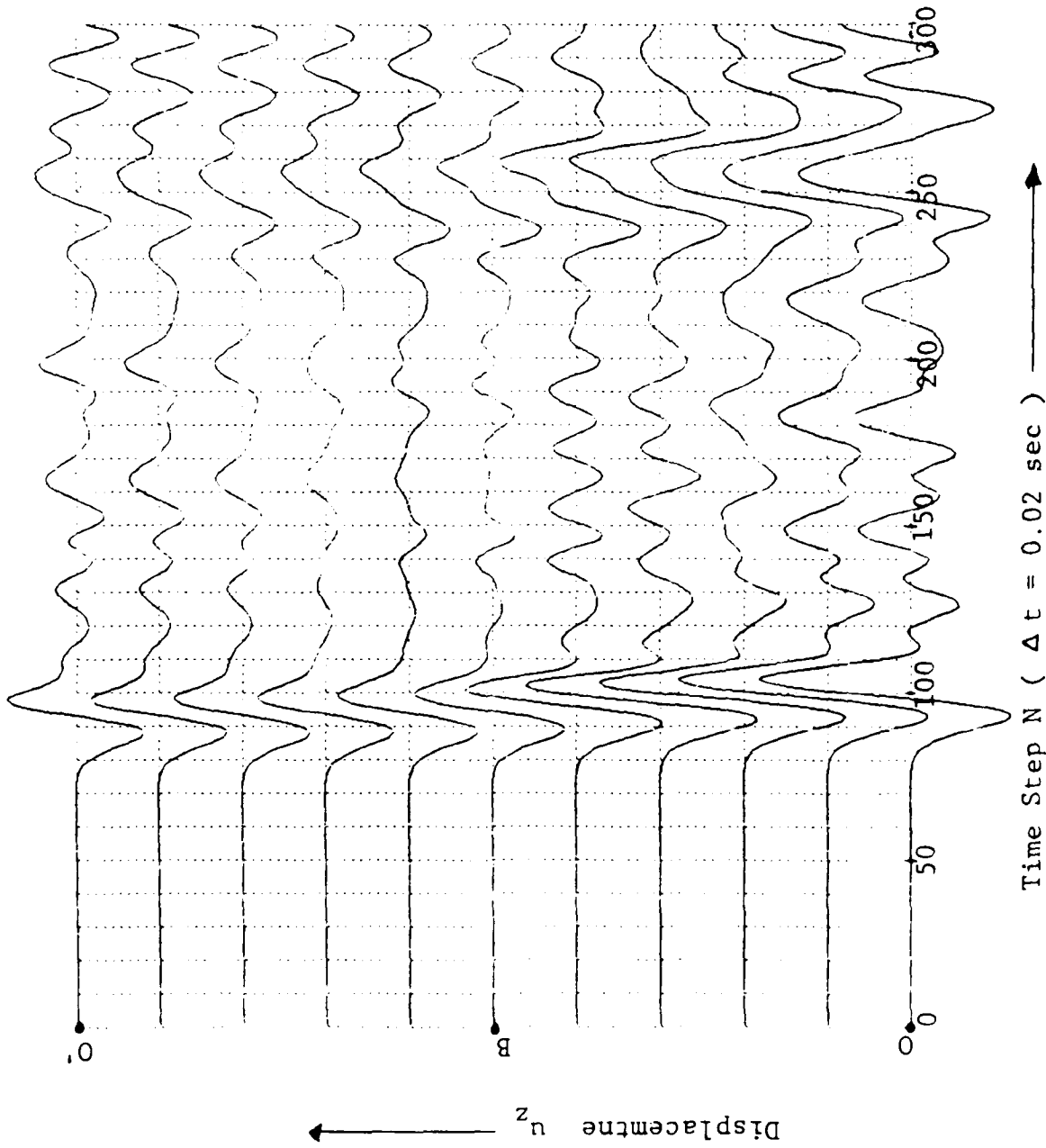


Figure 10. Synthetic Seismogram Along Free Surface 00' For Model 2.

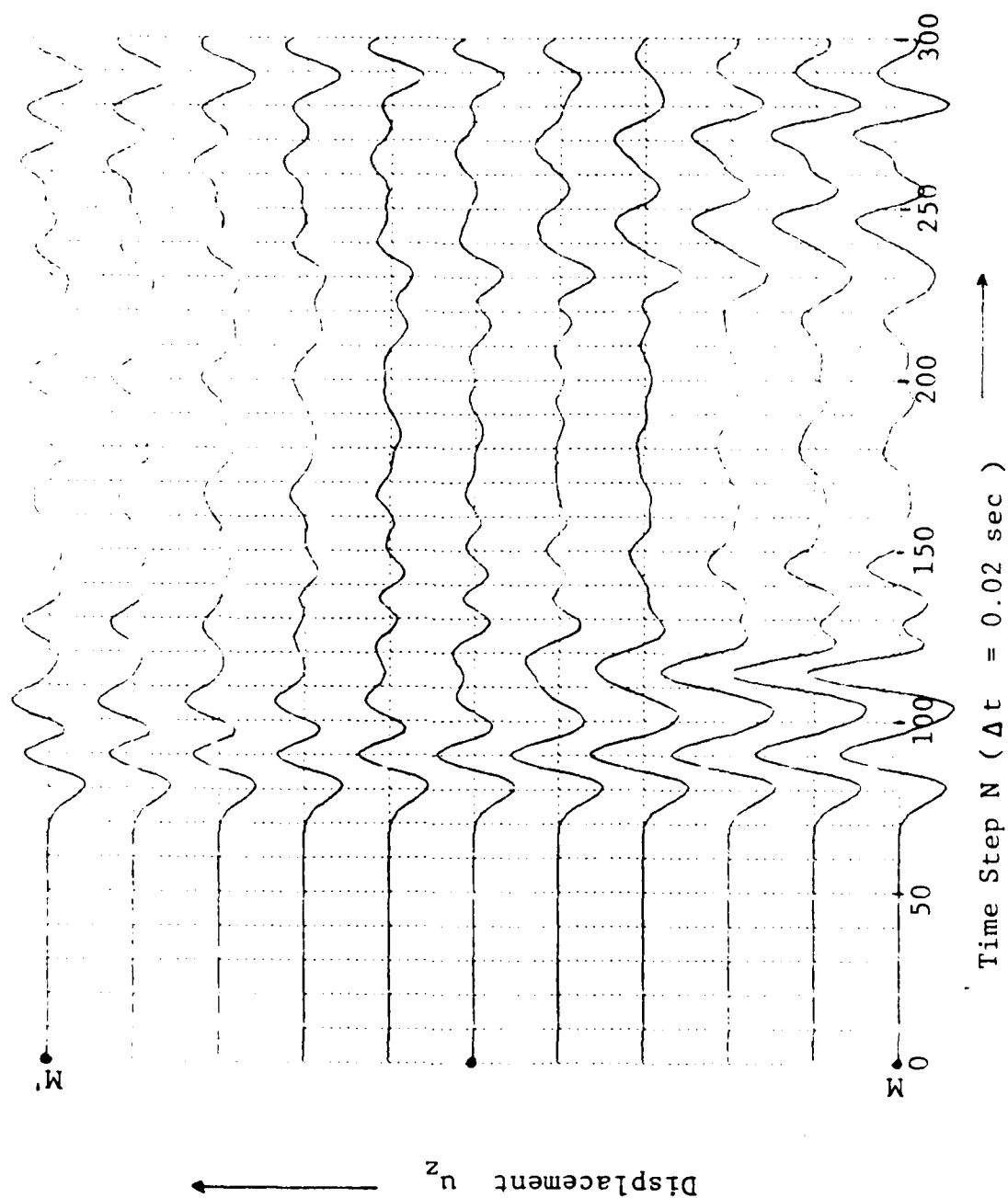


Figure 11. Synthetic Seismogram Along Horizontal Surface MM' For Model 2.

(c) Model 3:

In this section, two partial basins are modeled. Both basins use the same homogeneous material as Model 1 above, but with a different geometry, as shown in Figures 12 (Model 3-a) and 13 (Model 3-b). In Figure 12, an SH wave line source is excited at Point S on the free surface of the deeper basin, while the receivers are located on the free surface of the shallower basin, in the region BC. For Model 3-b (in Figure 13), an SH source is located in the shallower basin, while the receivers are in the deeper basin. Again, the forcing function is the first derivative of a Gaussian function with its center frequency $f_c \sim 2.5$ Hz. The calculated displacements u_z for Models 3-a and 3-b obtained along ABC in both models are shown in Figures 14 and 15, respectively. In Figures 14 and 15, at the corner B, as expected, waves change their magnitude and phase. In the case of Model 3-b, the reflection from plane DB causes drastic changes in phase and amplitude. From the distortion of these waves, shown in Figure 14, we may conclude that, since the arrivals at the position ABS' are the diffracted waves generated at O, the effect of the diffraction due to the corner is small in comparison with the arrivals of the direct waves received at the position ABS' in Model 3b (Figure 13).

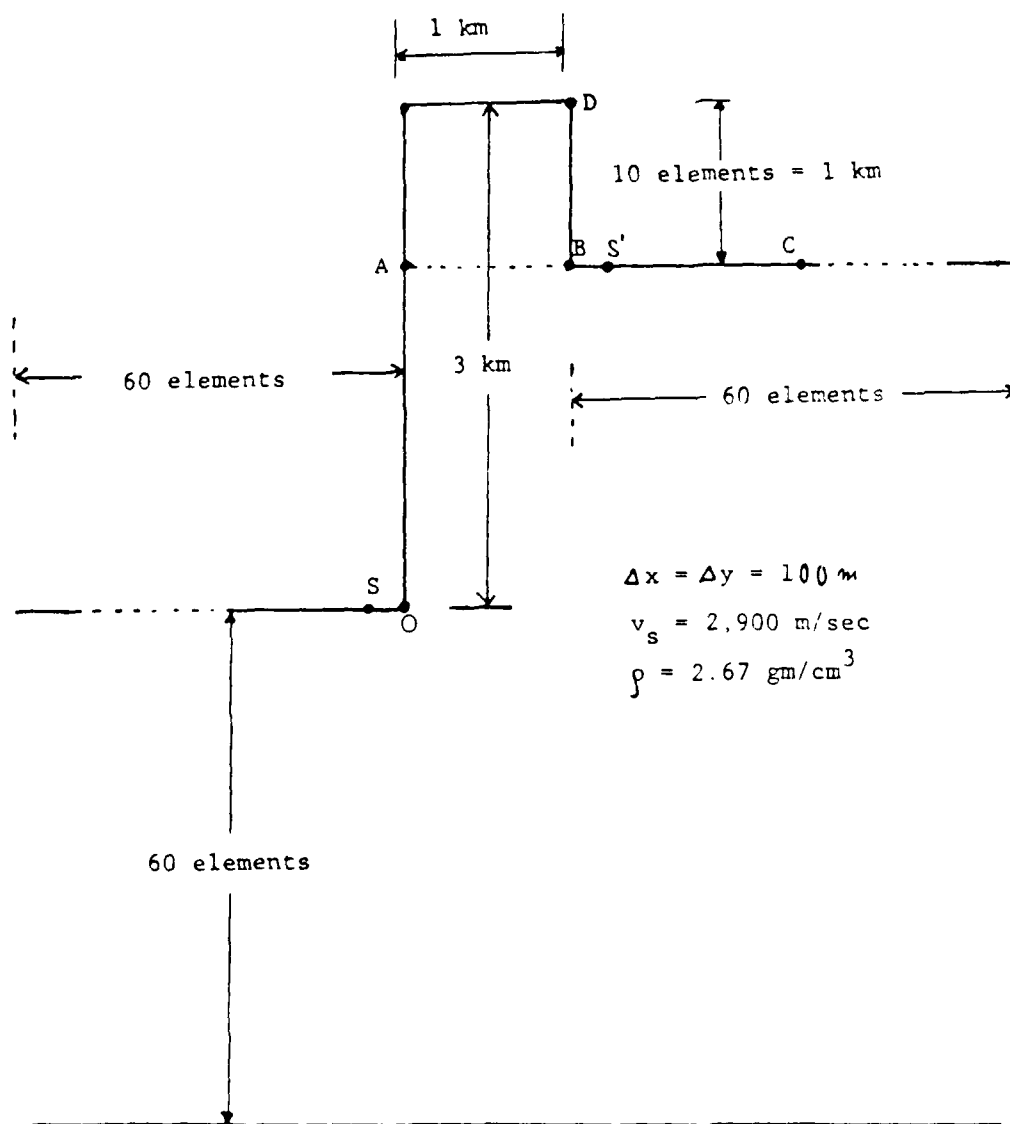


Figure 12. Preliminary Basin Model 3-a.

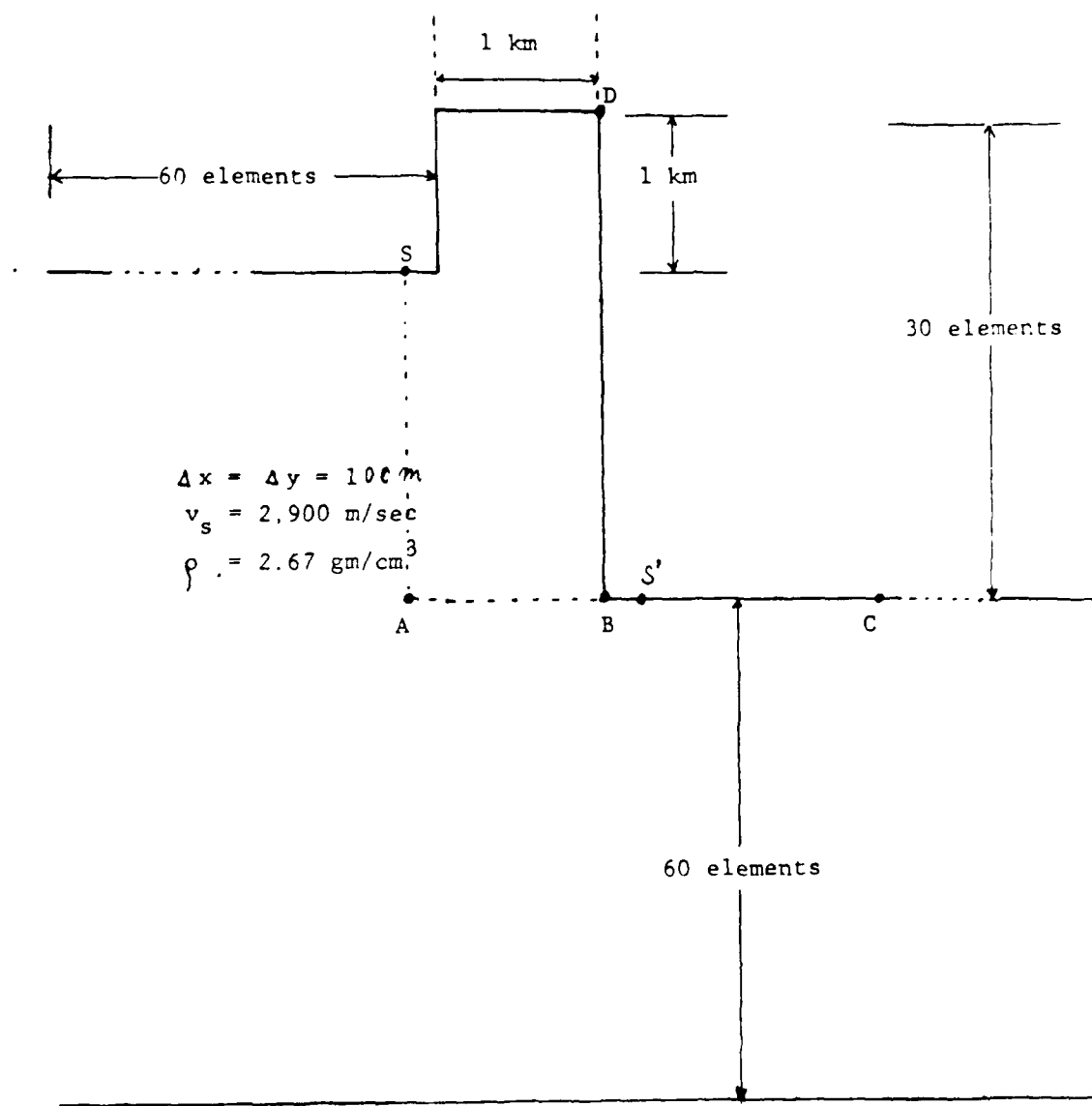


Figure 13. Preliminary Basin Model 3-b.

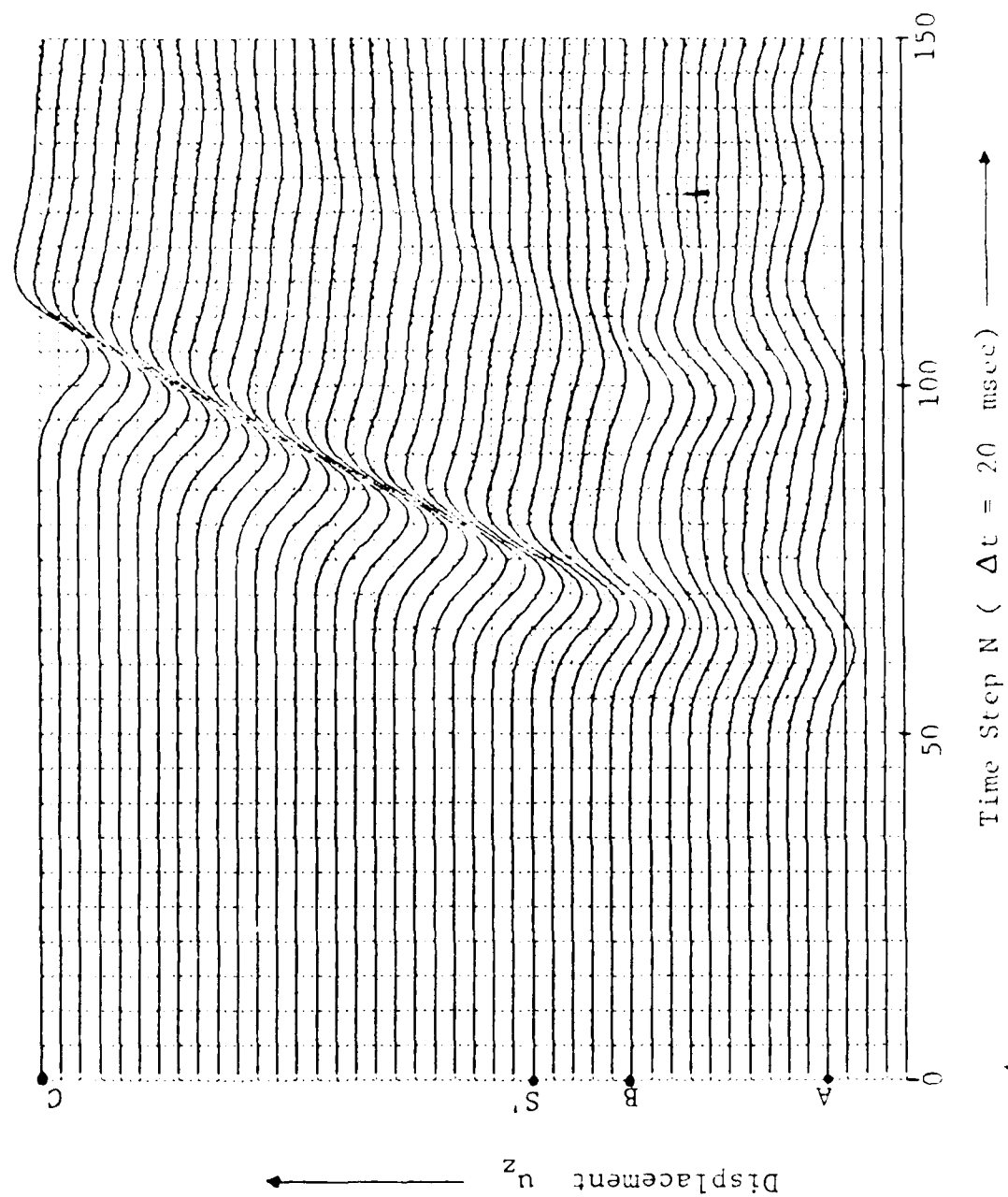


Figure 14. Synthetic Seismogram Along ABC of Model 3-a.

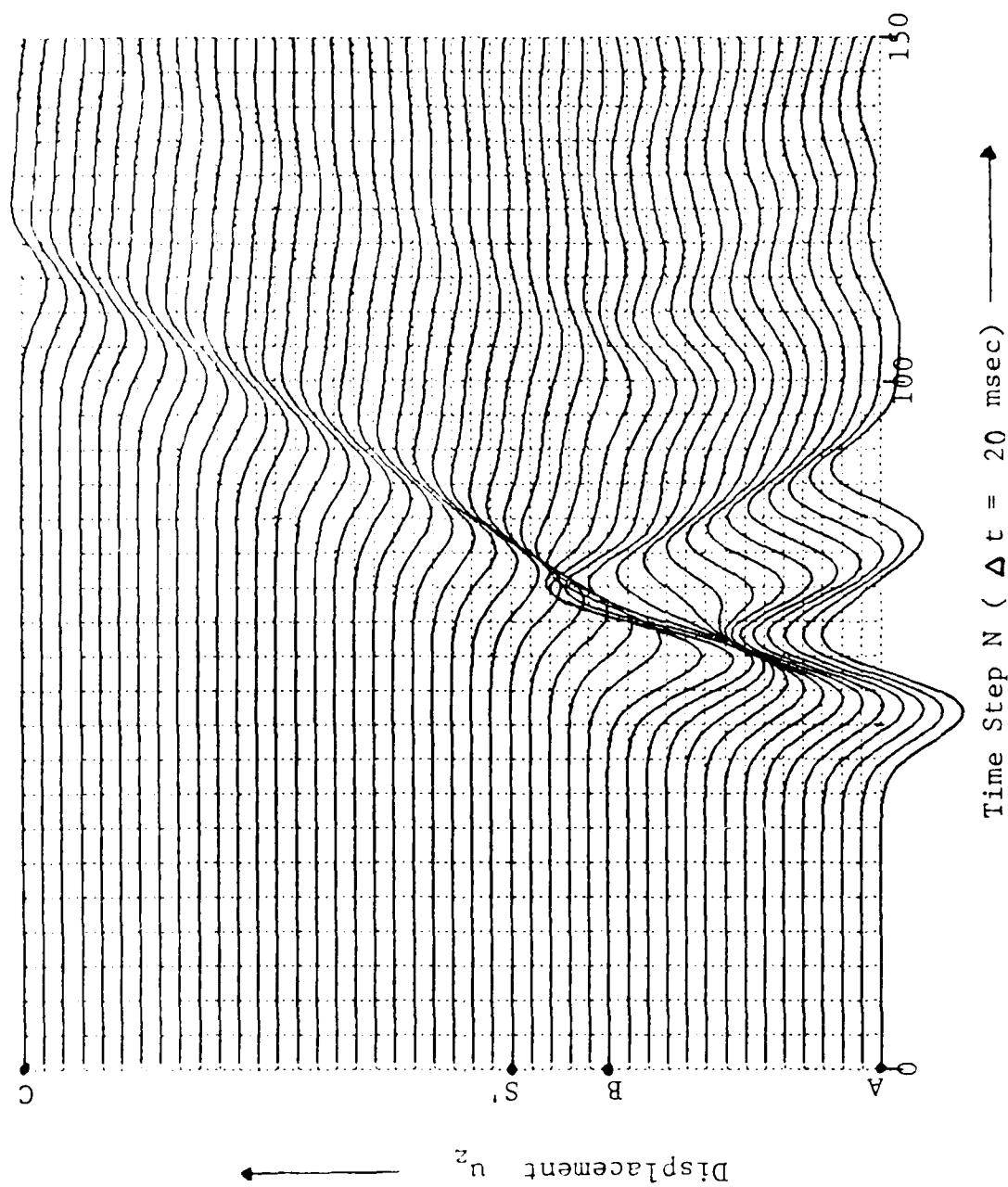


Figure 15. Synthetic Seismogram Along ABC of Model 3-b.

(2) SIMPLE MODELS FOR ELASTIC WAVES (P & SV WAVES)

(a) Preliminary Basins Model 3-A and Model 3-B

We have studied two preliminary basin models as shown in Figures 16 and 17 for the case of elastic (P and S) waves. In Figure 16, the homogeneous medium of the preliminary basin model ($v_p = 5,000$ m/sec, $v_s = 2,900$ m/sec, $\rho = 2.67$ gm/cm³) is excited by a vertical forcing function $F_0(t)$ as shown in Figure 18 at Point S on the free surface of the deeper basin DC. The receivers are located on the free surface of the shallower basin in the region BC. In Figure 18 the source of a vertical forcing function is located in the shallower basin. The receivers are located in the deeper basin. Again, the forcing function is the first derivative of a Gaussian function with its center frequency $f_c \sim 2.7$ Hz. Figures 19 and 20 are the results of the vertical and horizontal displacement components along plane ABC for both Model 3A and Model 3B, showing the complexity of the wave arrivals, respectively.

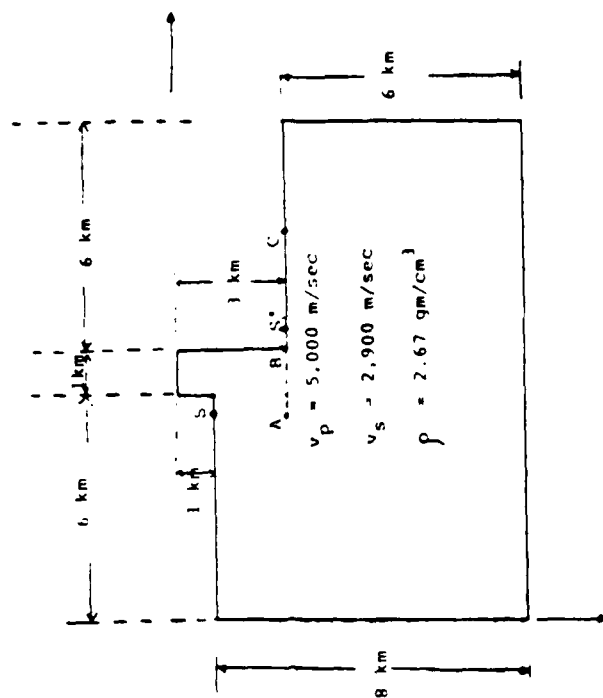


Figure 16. Preliminary Basin Model 3-A
for Elastic Waves.

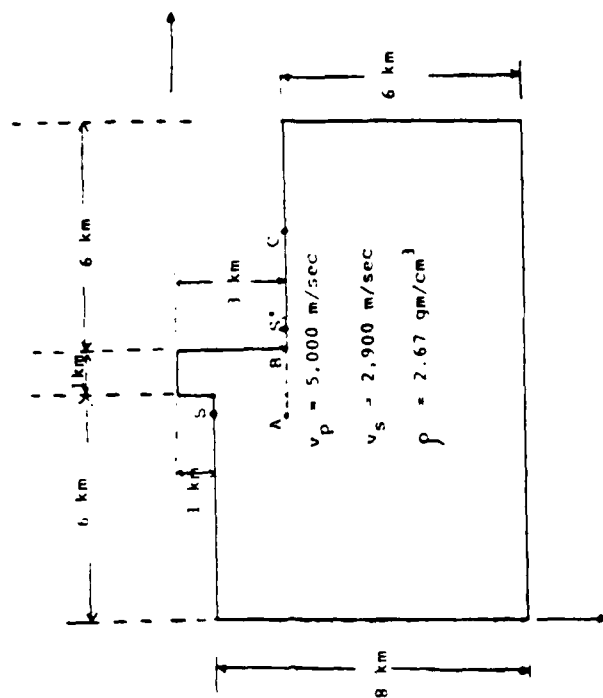


Figure 17. Preliminary Basin Model 3-B
for Elastic Waves.

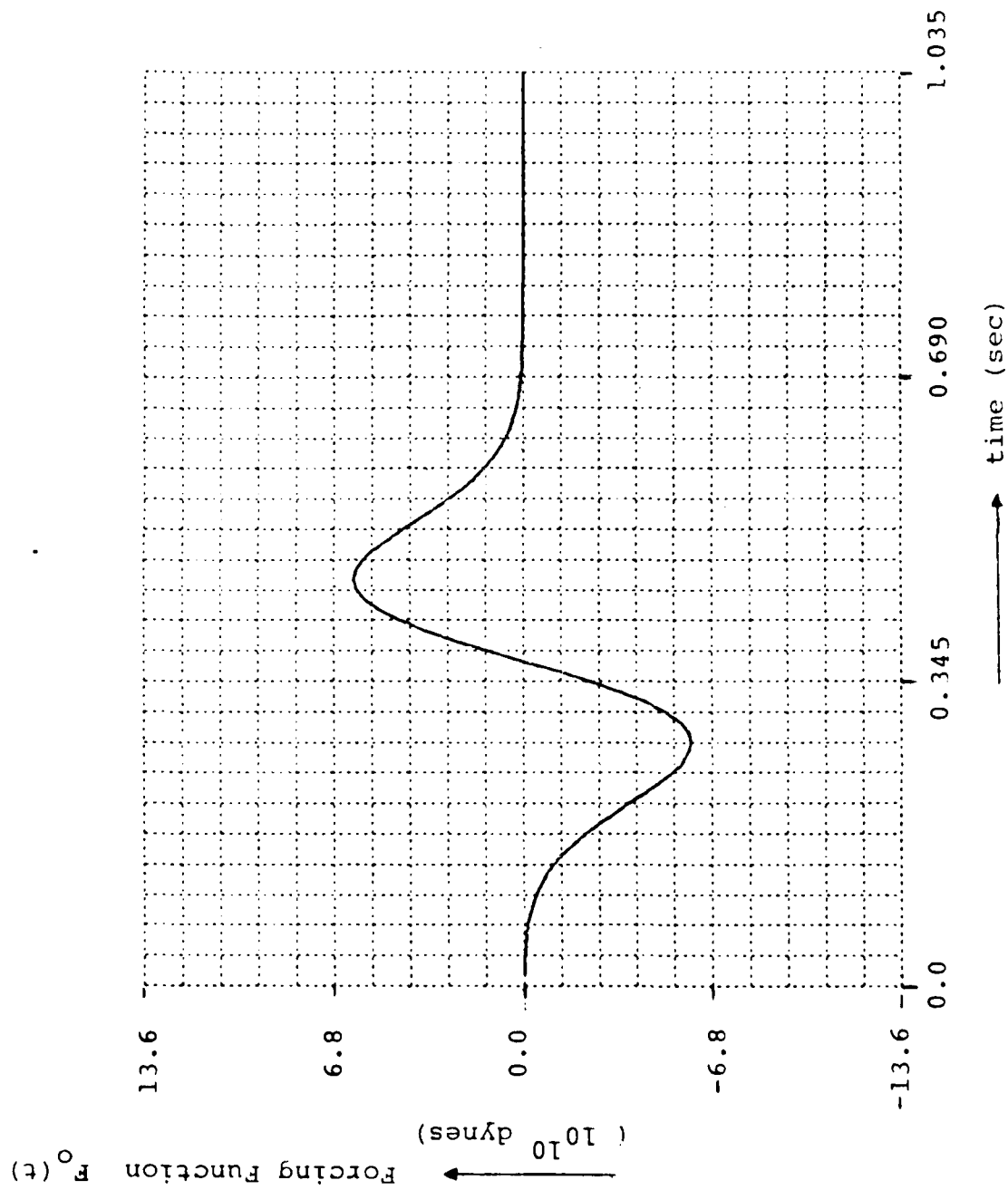


Figure 18. Source Function for Elastic Cases.

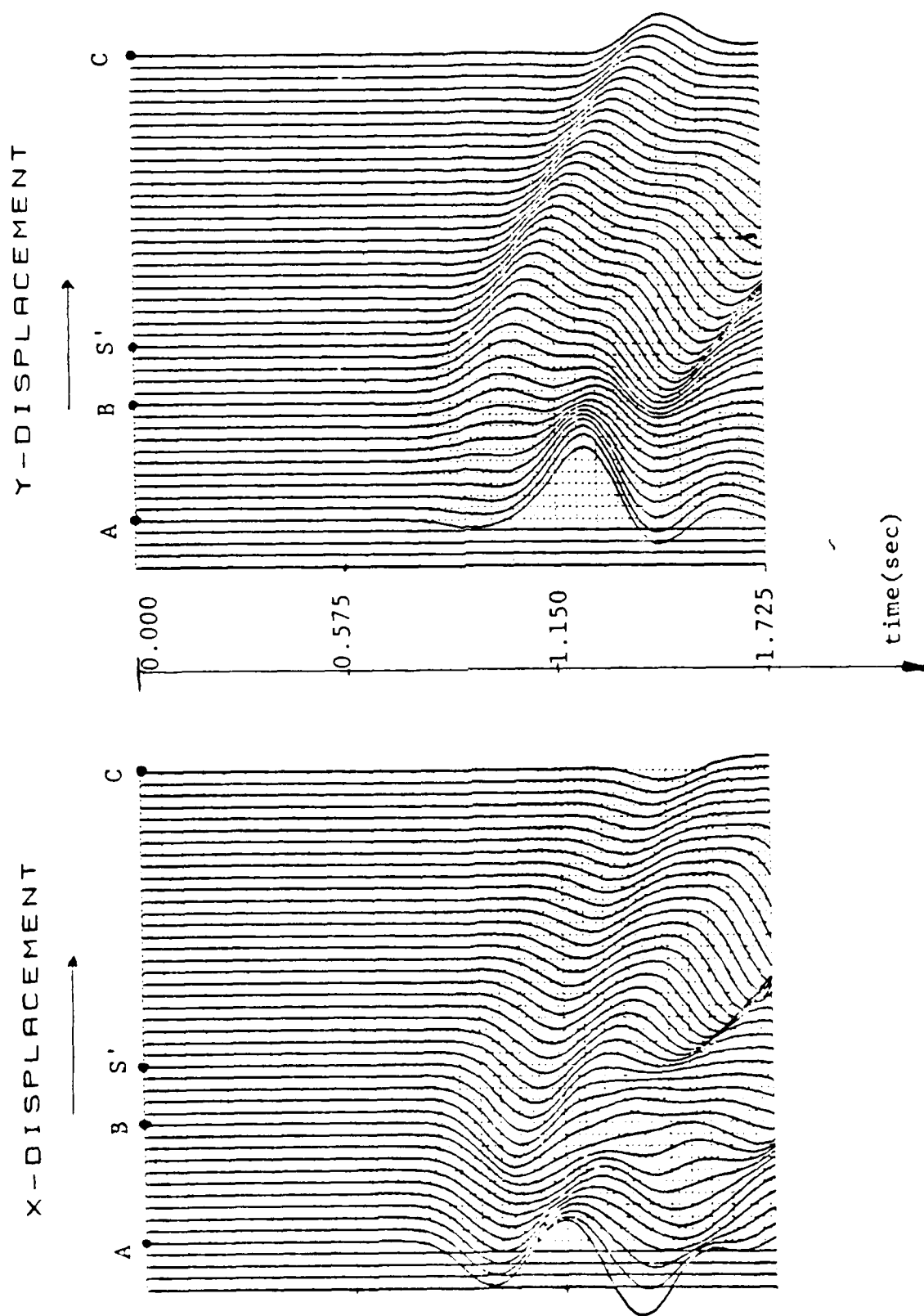


Figure 19 Synthetic Seismogram Along ABC of Model 3-A.

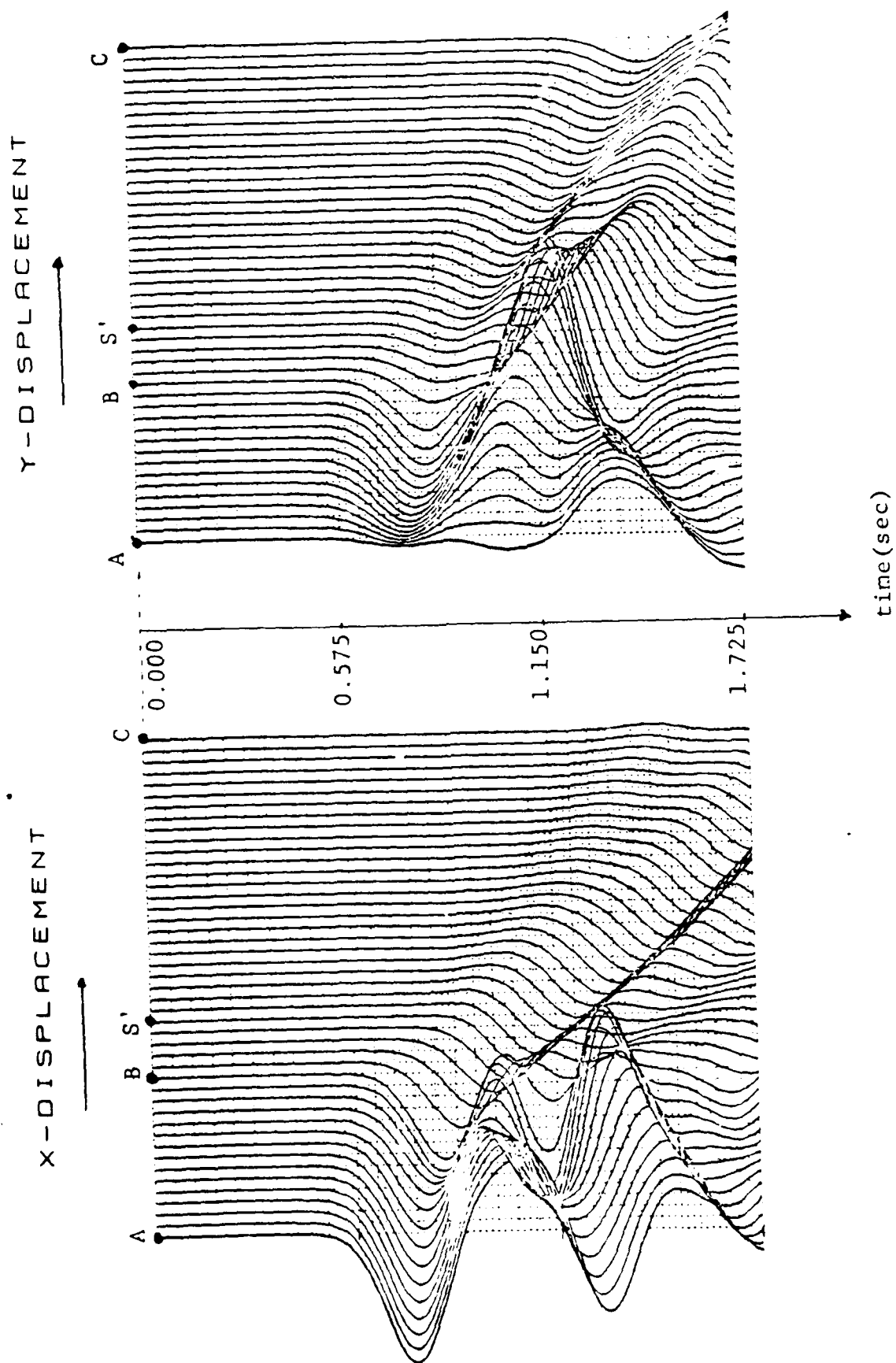


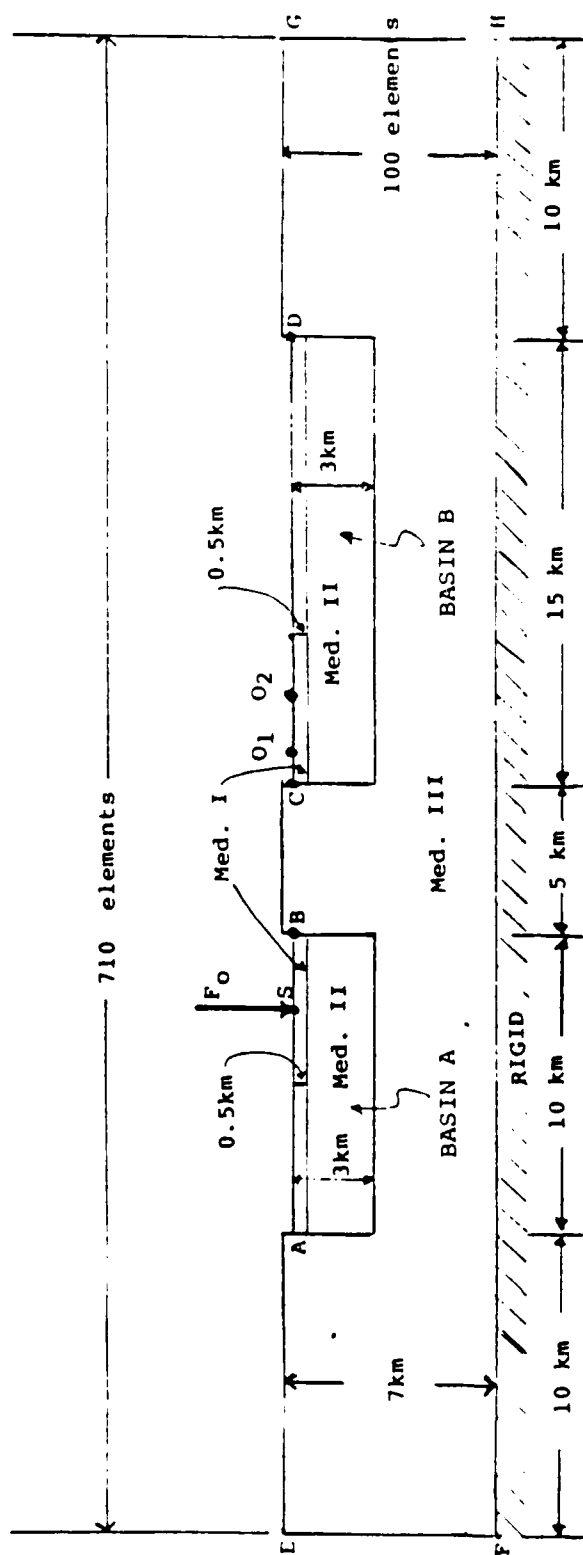
Figure 20. Synthetic Seismogram Along ABC of Model 3-R.

(b) Two Adjacent Alluvial Basins for
Elastic Waves (P and S Waves)

The finite element model of the two adjacent alluvial basins, A and B, is shown in Figure 21. The basin is filled with 3 km of sediments ($v_{p2} = 3,500$ m/sec, $v_{s2} = 1,905$ m/sec, $\rho_2 = 2.5$ gm/cm³), which are overlain by a surface low velocity layer (0.5 km thick, $v_{p1} = 2,200$ m/sec, $v_{s1} = 1,180$ m/sec, $\rho_1 = 2.3$ gm/cm³). The bedrock of the basement is assumed to have $v_{p3} = 5,500$ m/sec, $v_{s3} = 3,175$ m/sec, $\rho_3 = 2.7$ gm/cm³. The basin B is 15 km in width and filled with the same materials as basin A. The basement is bounded by a rigid halfspace. The total length of the two alluvial basin model is 50 km. The thickness of the model is 7 km. A vertical force load is located in a smaller basin (Basin A of Figure 21) with a width of 10 km. The source forcing function, F_0 , used in the finite element calculation is that of the first time derivative of a Gaussian function as shown in Figure 22. In order to obtain a stable and accurate solution, we choose a time step, Δt , that satisfies the Courant-Friedrickson-lewy (CFL) condition and an element dimension s to be small enough so that one wavelength can be approximately simulated by $10 \Delta s$. In doing so, the width of the forcing function $N \Delta t$ should be greater than a factor of about $(8.3 v_{\max} \Delta t) / v_{\min}$, where v_{\max} and v_{\min} are the largest and the smallest velocities in the whole finite element model.

For the finite element alluvial basin model, we use a source function having a pulse width of $160 \Delta t$ ($N=40$). A total of approximately 70,000 elements is required for such a model. Using a center frequency of the forcing function of about 1 Hz, the total number of equations of motion is

140,000. Figures 23-A to 24-B are the preliminary results obtained from the model. Figures 23-A and 23-B are the synthetic seismograms of the vertical and horizontal displacements at various nodal points along the surface S0 (see Figure 21). These displacements are normalized to the displacement of the forcing function at the loading position. Figure 24-A and 24-B are these synthetic seismograms along nodal points B0 with a scale 10 times larger than that used in Figures 23-A and 23-B. At the corners B and C, the arrivals are drastically changed in magnitude and phase due to the complexity of the basin structure.



$$\rho_1 = 2.3 \text{ gm/cm}^3, \quad V_{p1} = 2,200 \text{ m/sec}, \quad V_{s1} = 1,180 \text{ m/sec},$$

$$\rho_2 = 2.5 \text{ gm/cm}^3, \quad V_{p2} = 3,300 \text{ m/sec}, \quad V_{s2} = 1,905 \text{ m/sec},$$

$$\rho_3 = 2.7 \text{ gm/cm}^3, \quad V_{p3} = 5,500 \text{ m/sec}, \quad V_{s3} = 3,175 \text{ m/sec}.$$

Figure 21. Finite Element Model for the Problem of Ground Response in Two Basins Due to Seismic Disturbances.

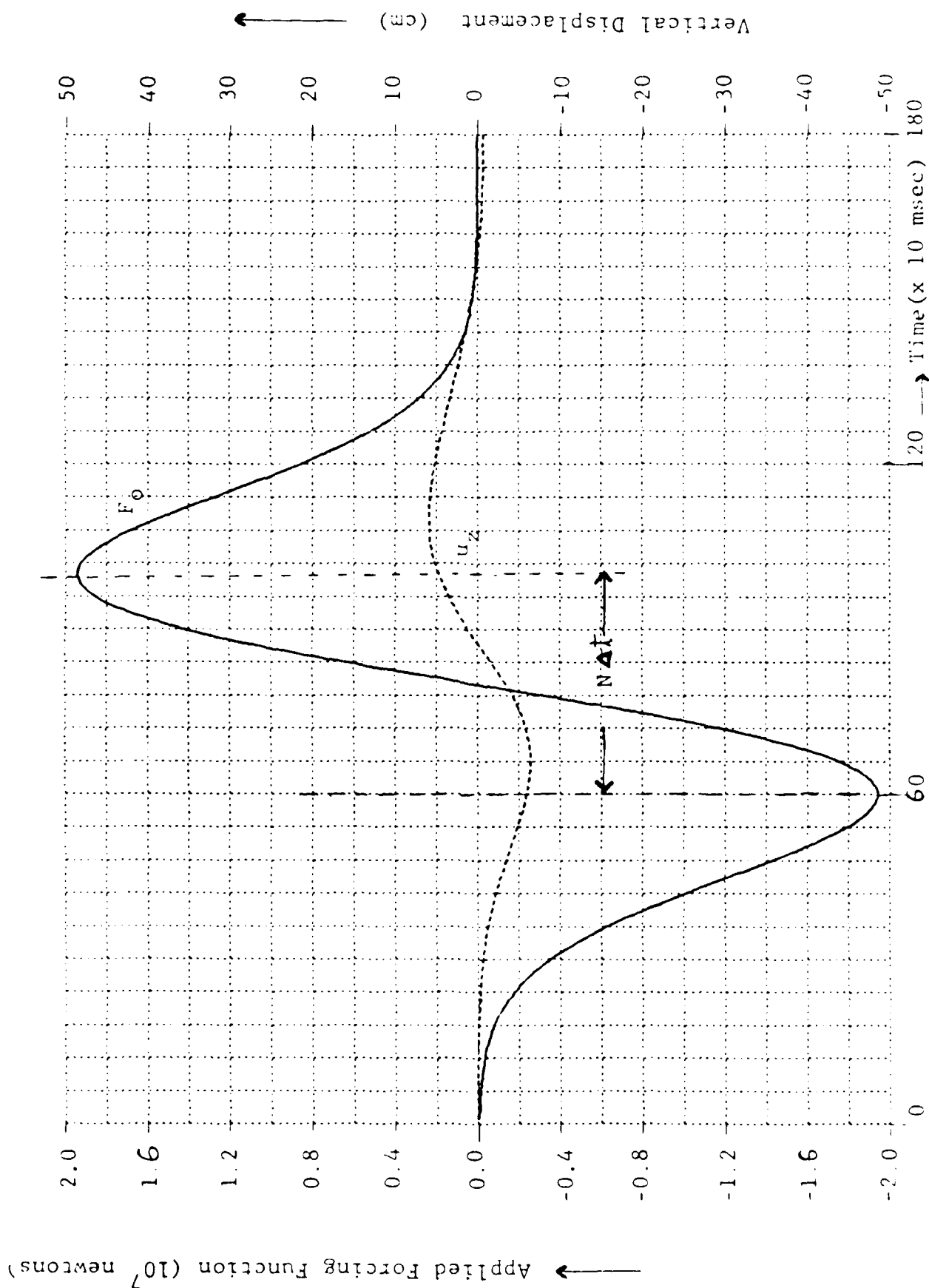


Figure 22. ——— Distribution of Time Dependent Forcing Function.

----- Distribution of Vertical Displacement at the Loading Position.

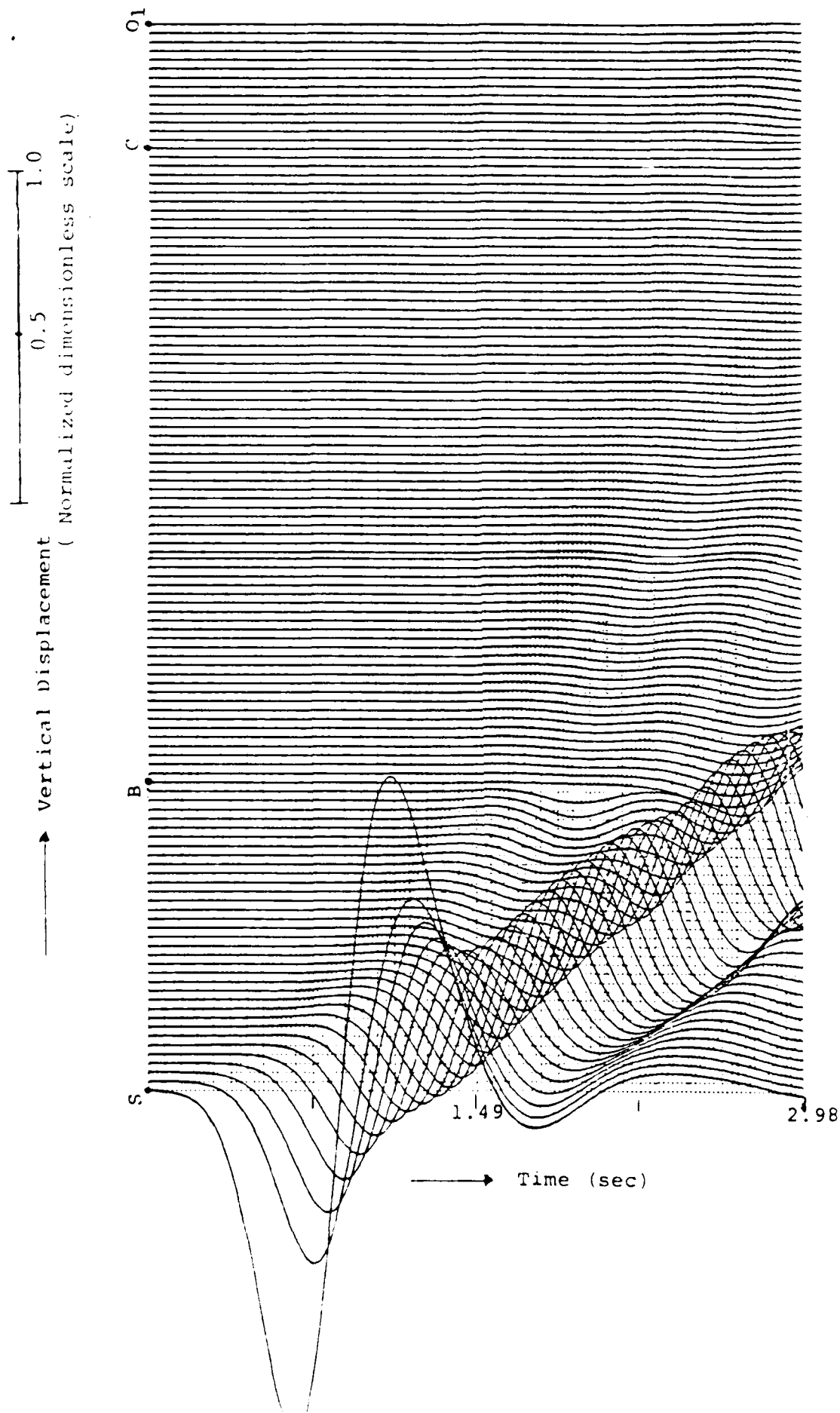


Figure 23a. Vertical Displacement Along Surface SO_1 .

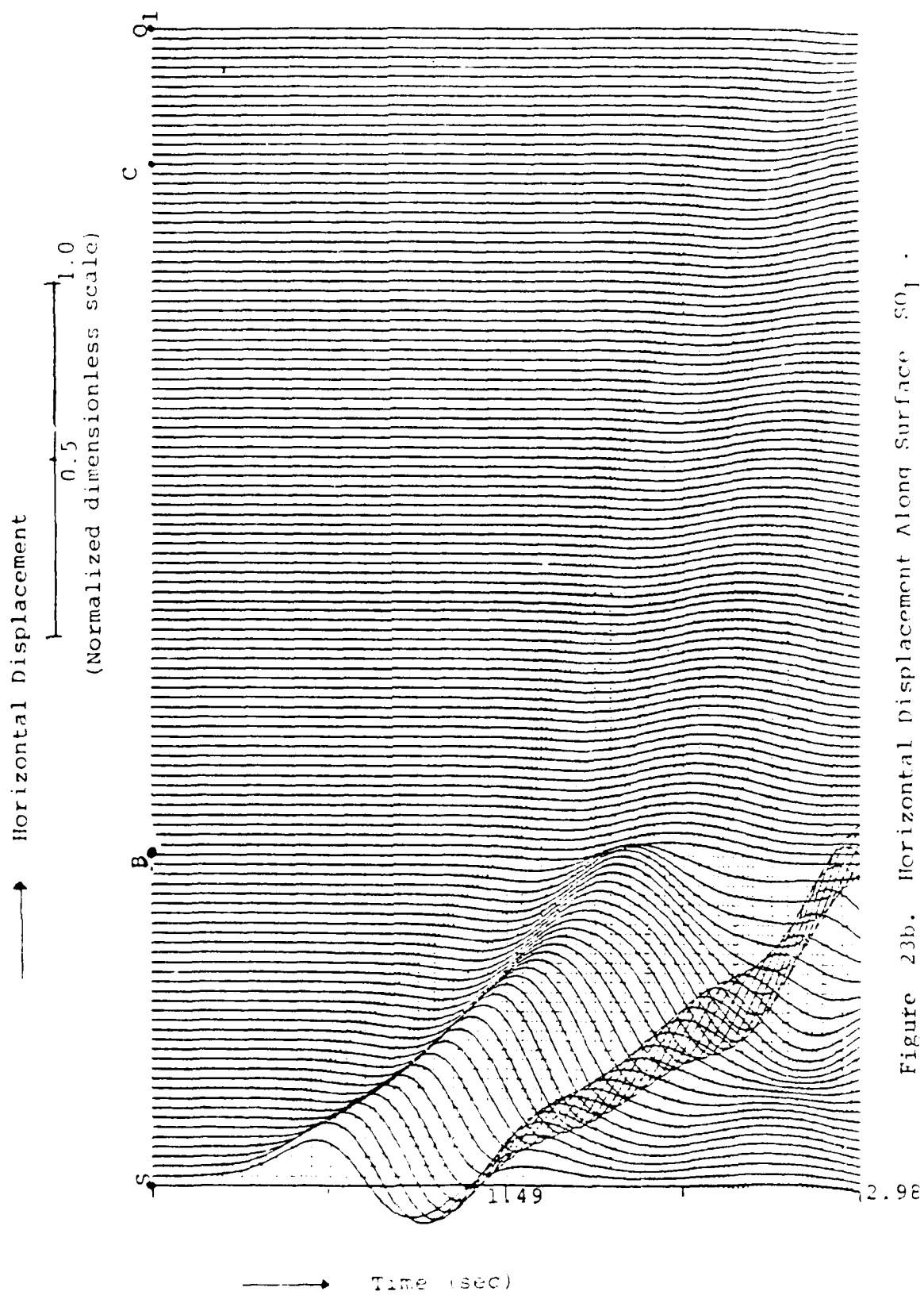


Figure 23b. Horizontal Displacement Along Surface S01.

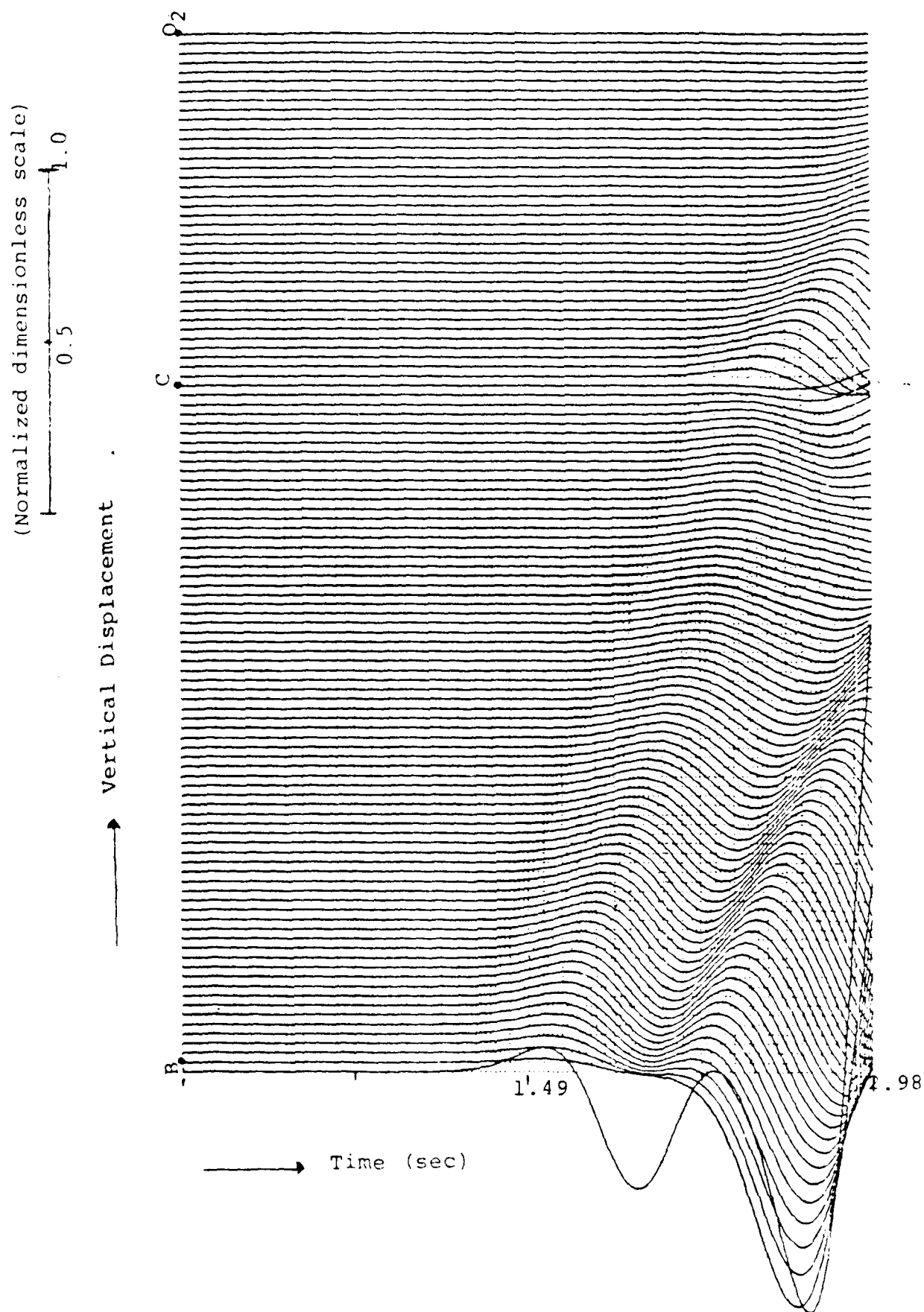
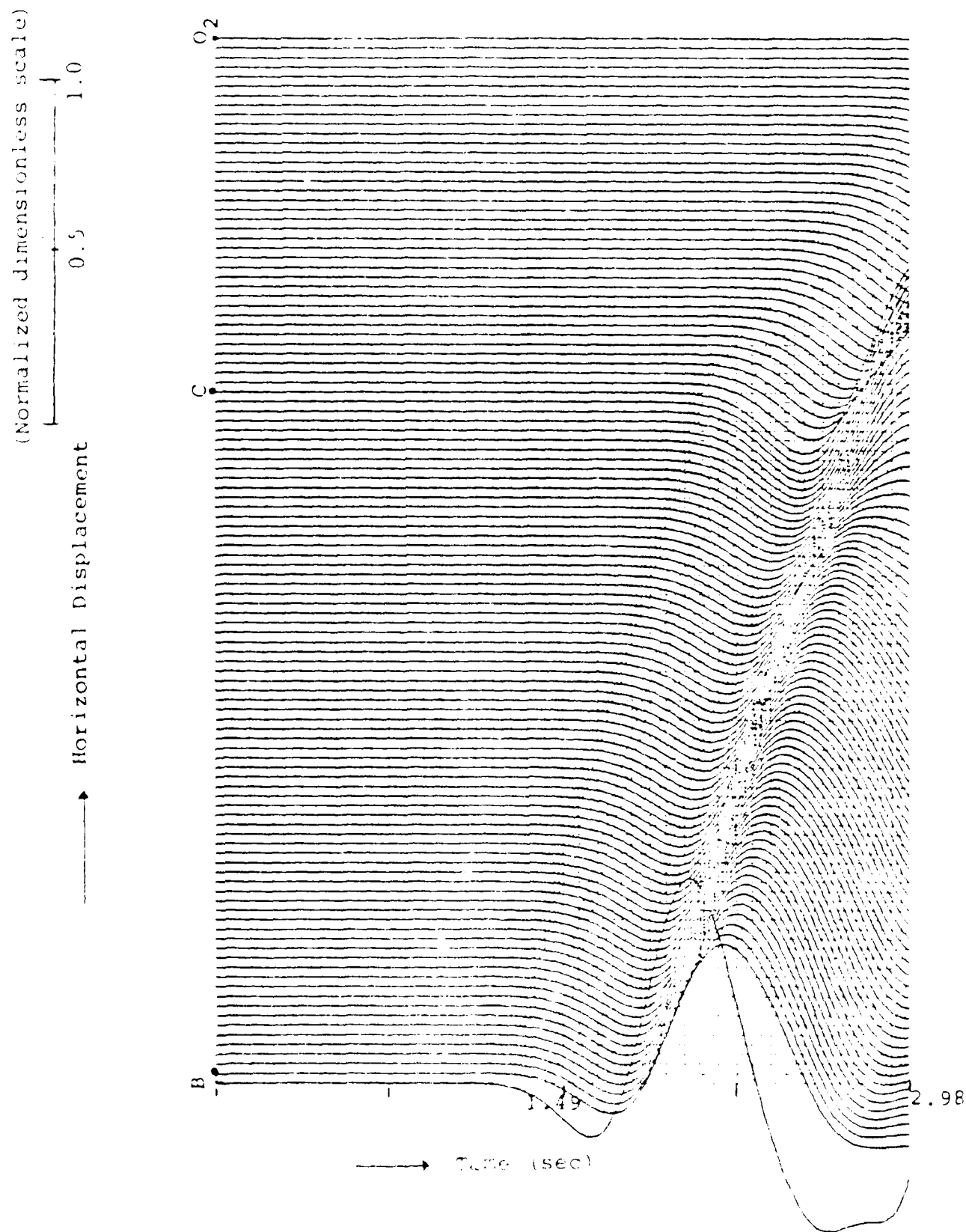


Figure 24a. Vertical Displacement Along Surface P02.

Figure 241. Horizontal Displacement Along Surface PO₂.

II. FINITE ELEMENT MODELING OF BASINS WITH DISPLAY OF SNAPSHOTS

In order to obtain a clear display of the results of basin modeling, an Aldridge Laboratory computer code for snapshots has been implemented to our present finite element computer programs. These snapshots provide a means to visualize the time history of the wave interactions and to identify the resulting wave shapes, the direction of propagation, and the nature of mode conversion. For demonstration, snapshots have been made for the following three cases:

Case I: Model 3-A for Elastic Waves

Figures 25-A to 25-G are snapshots of the synthetic wavefield at 0.3 sec intervals. Vertical and horizontal displacement components are given separately. Each snapshot is independently scaled and the amplitude is magnified 10 times. Black is positive displacement and white is negative displacement. Diffracted waves from the square corners are clearly identified after 0.9 sec.



FIGURE 25-B. A Snapshot view of Wave Pattern at 0.6 sec after the Detonation of the Source.

FIGURE 25-A. A Snapshot view of Wave Pattern at 0.3 sec after the Detonation of the Source.



Figure 25-D. A Snapshot View of Wave Pattern at 1.2 sec after the Detonation of the Source.

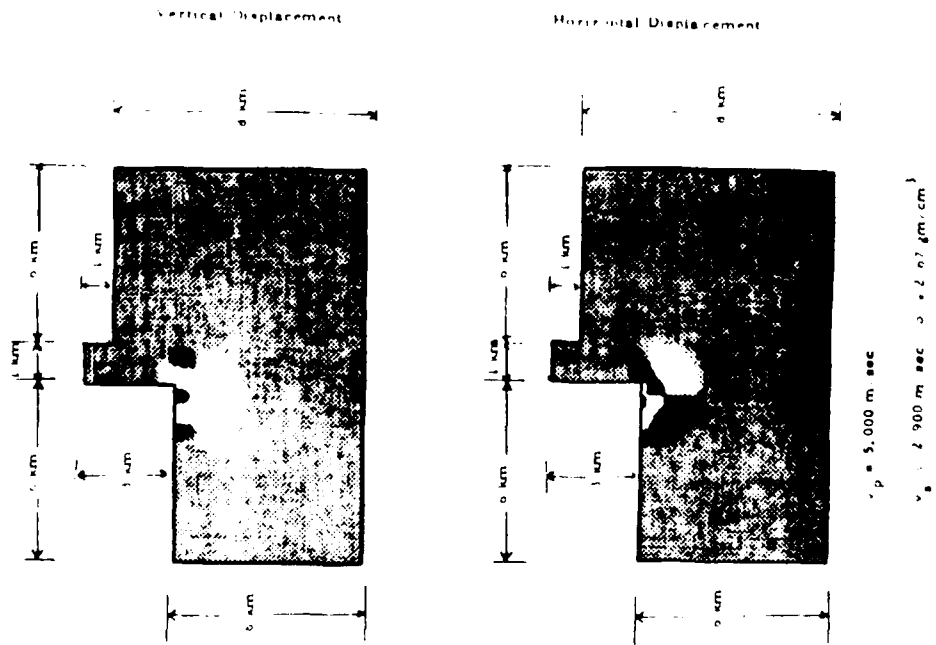


Figure 25-C. A Snapshot view of Wave Pattern at 0.9 sec after the Detonation of the Source.

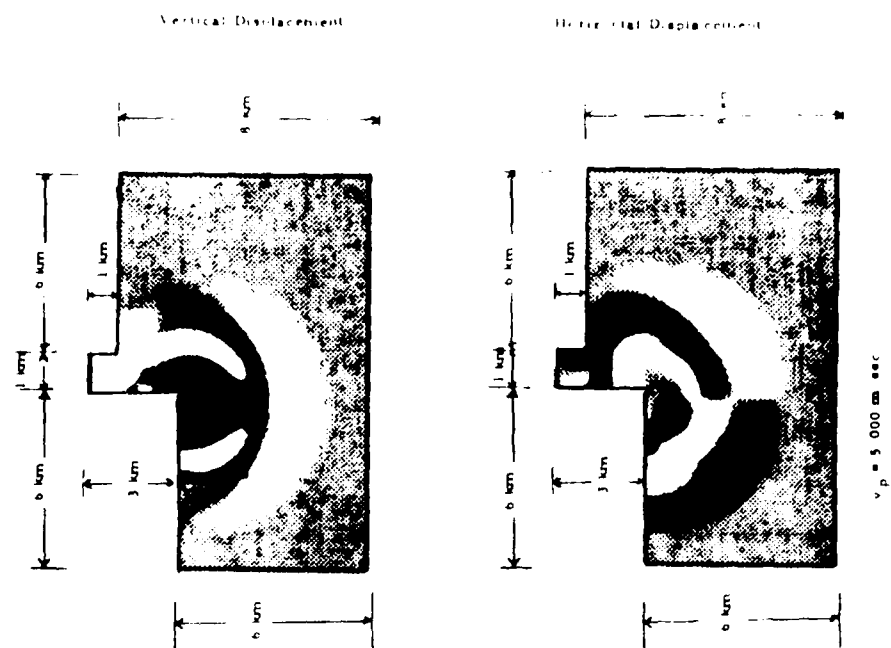


Figure 25-F. A Snapshot View of Wave Pattern at 1.8 secs after the Detonation of the Source.

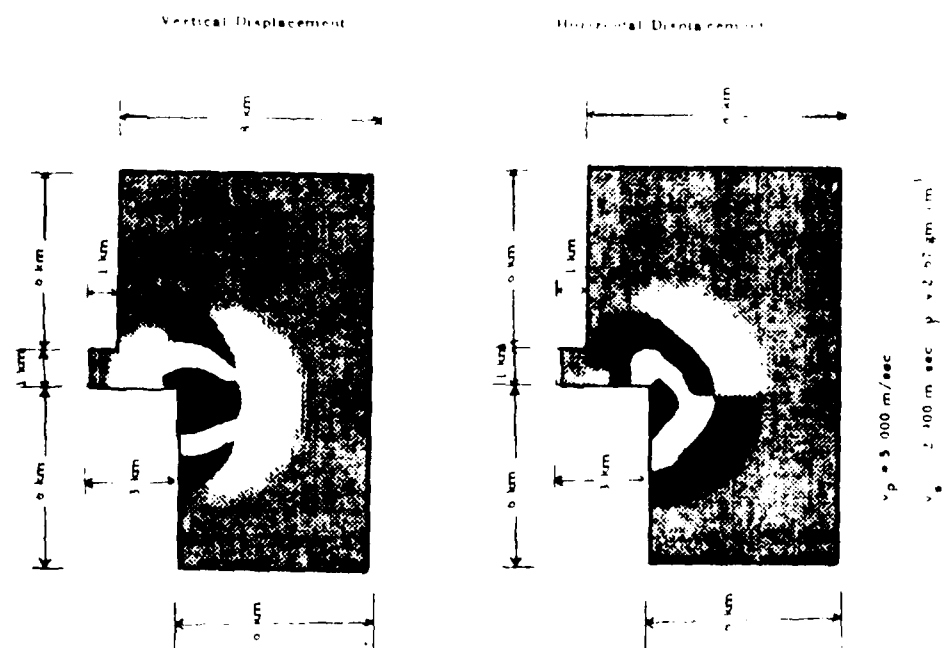
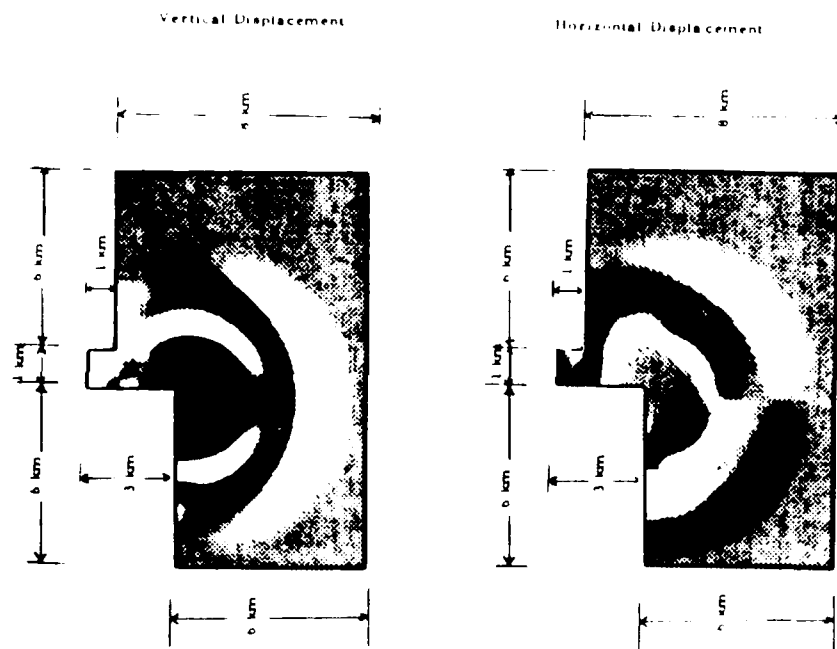


Figure 25-E. A Snapshot View of Wave Pattern at 1.5 secs after the Detonation of the Source.



$v_p = 5,000 \text{ m/sec}$

$\rho = 2,000 \text{ gm/cc}$

Figure 23-6. A Snapshot View of Wave Pattern at 2.1 secs after the Detonation of the Source.

Case 2: Model 3-A for SH-Wave

In Figure 26, a SH-wave source , $F_1(t)$, is located at the corner S of the lower basin. The source function is shown in Figure 2. Figures 27-A to 27-O are the snapshots of the synthetic wavefield at 0.2 sec intervals. In this simple one-degree-of-freedom problem, reflections from the free surfaces and diffractions from the corners can be clearly identified. In Figures 27-M to 27-O, we observe that the wavefields are contaminated by the undesired reflections from the side and the bottom boundaries.

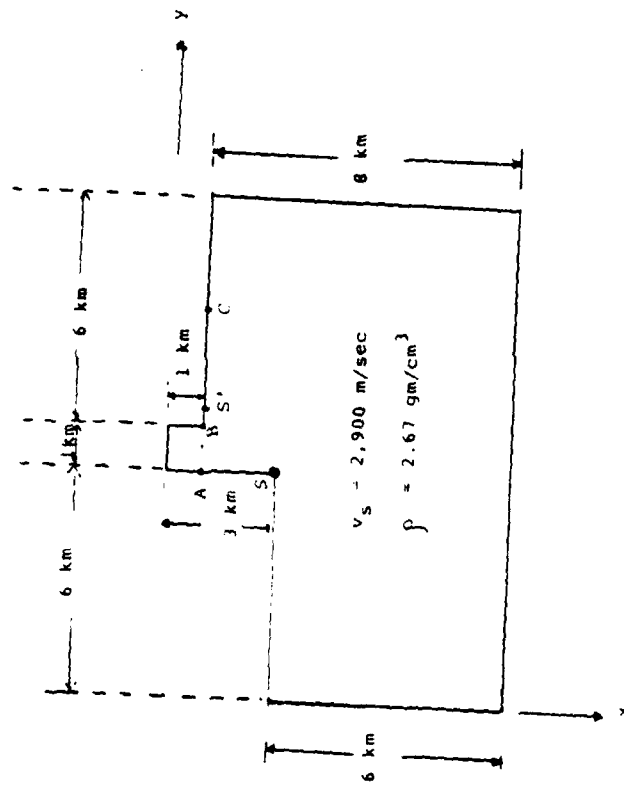


Figure 26. Preliminary Basin Model 3-A.

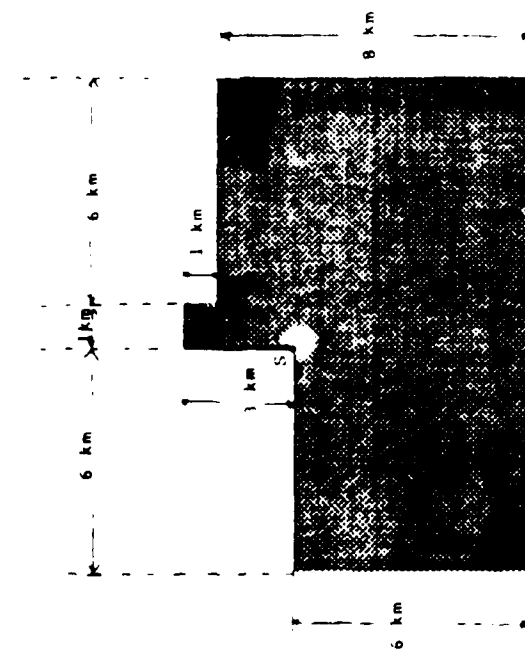


FIGURE 27-A. A Snapshot View of Wave Pattern at 0.2 sec after the Detonation of the Source.

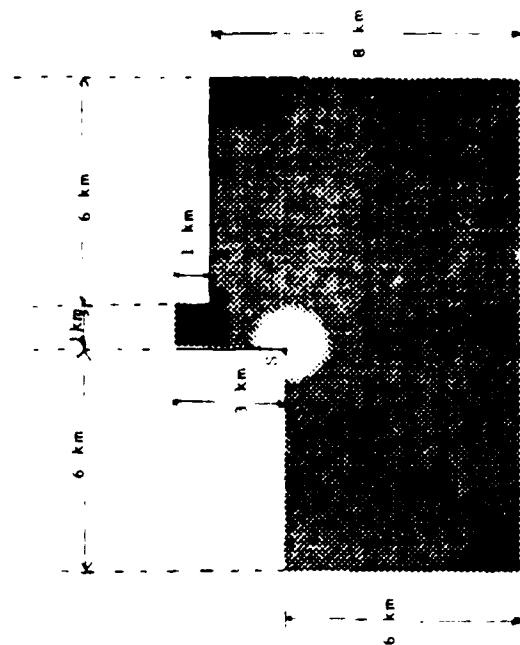


FIGURE 27-B. A Snapshot View of Wave Pattern at 0.4 sec after the Detonation of the Source.

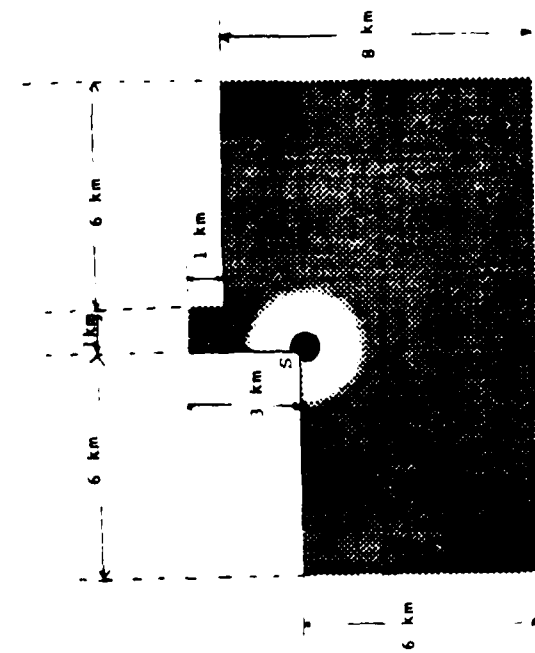


Figure 27-C. A Snapshot View of Wave Pattern at 0.6 sec after the Detonation of the Source.

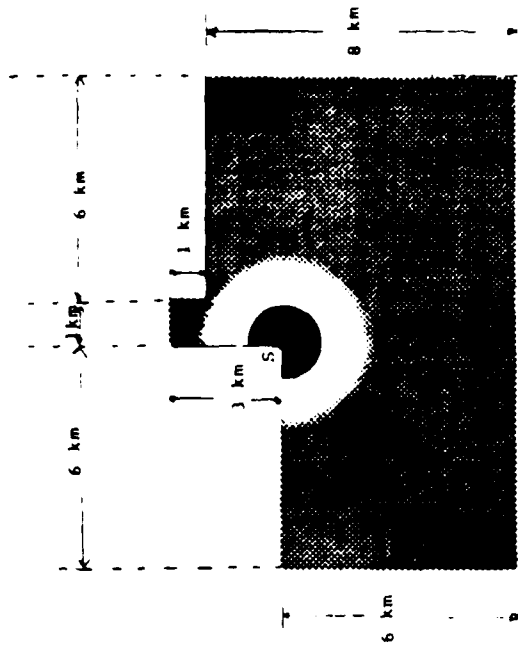


Figure 27-D. A Snapshot View of Wave Pattern at 0.8 sec after the Detonation of the Source.

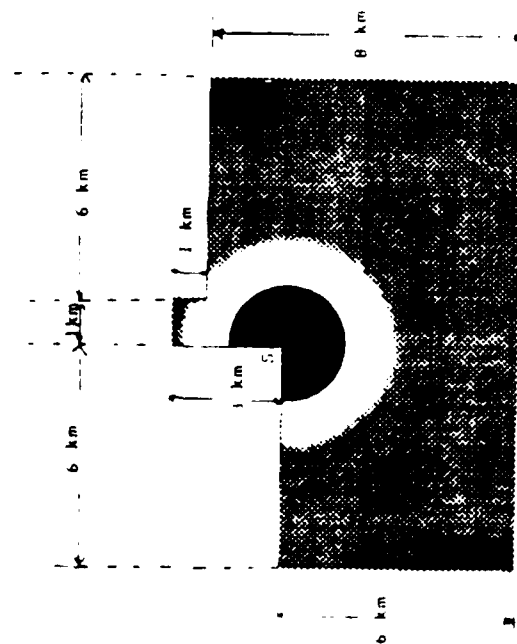


Figure 27-E. A Snapshot View of Wave Pattern at 1.0 sec after the Detonation of the Source.

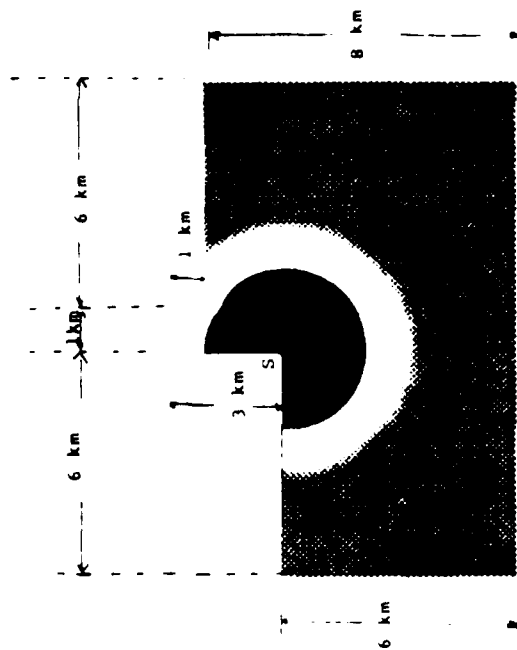


Figure 27-F. A Snapshot View of Wave Pattern at 1.2 sec after the Detonation of the Source.

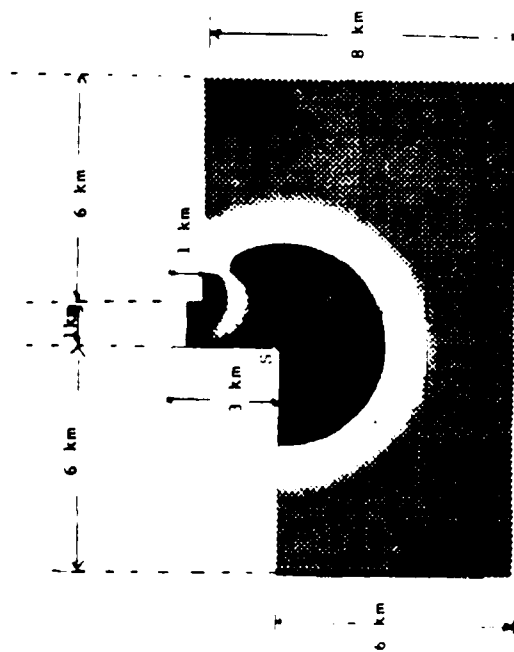


Figure 27-G. A Snapshot View of Wave Pattern at 1.4 sec after the Detonation of the Source.

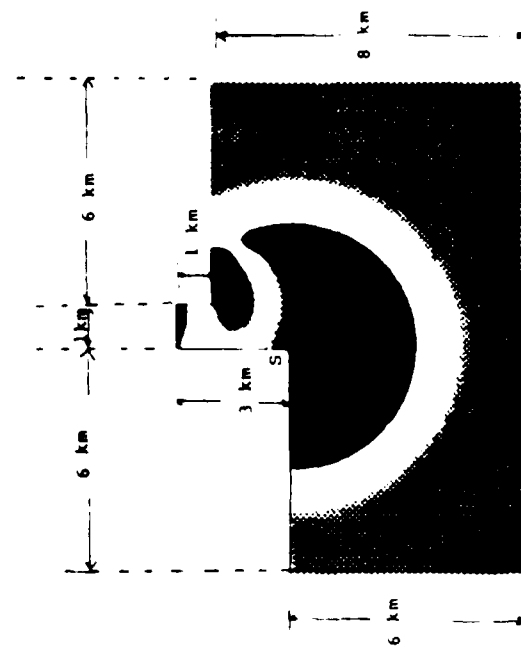


Figure 27-H. A Snapshot View of Wave Pattern at 1.6 sec after the Detonation of the Source.

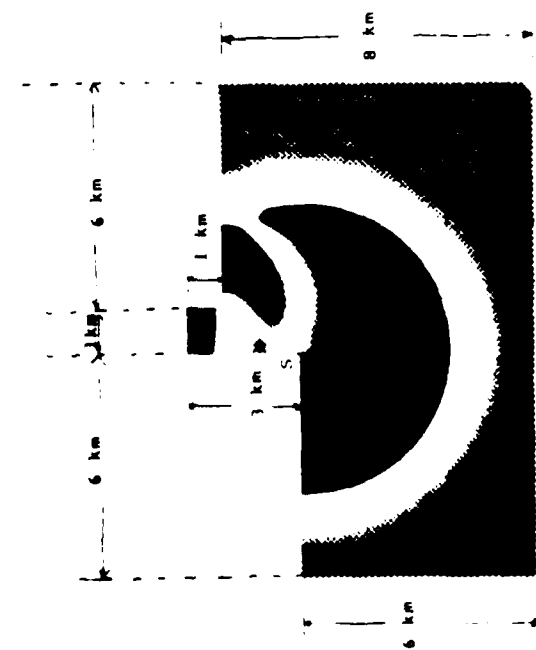


Figure 27-1. A Snapshot View of Wave Pattern at 1.8 sec after the Detonation of the Source.

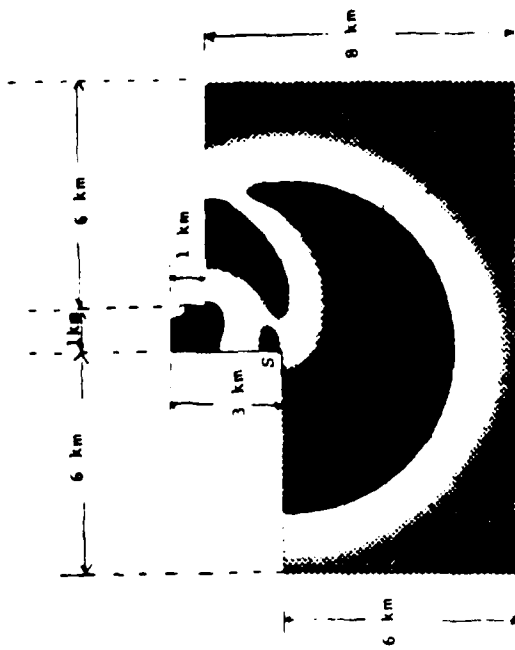


Figure 27-2. A Snapshot View of Wave Pattern at 2.0 sec after the Detonation of the Source.

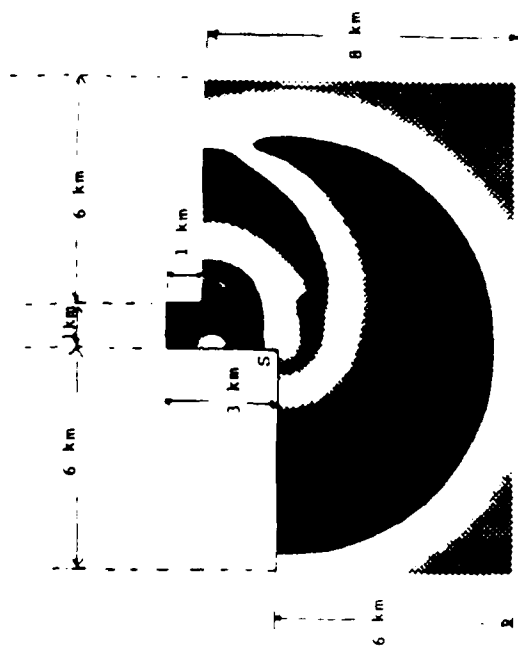


Figure 27-K. A Snapshot View of Wave Pattern at 2.2 sec after the Detonation of the Source.

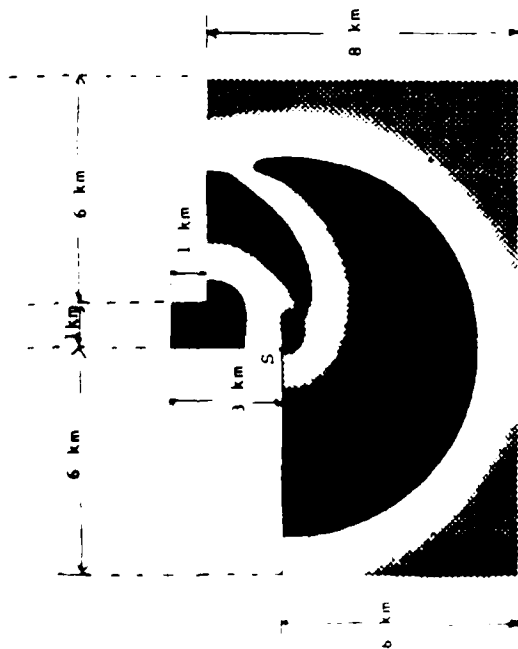


Figure 27-L. A Snapshot View of Wave Pattern at 2.4 sec after the Detonation of the Source.

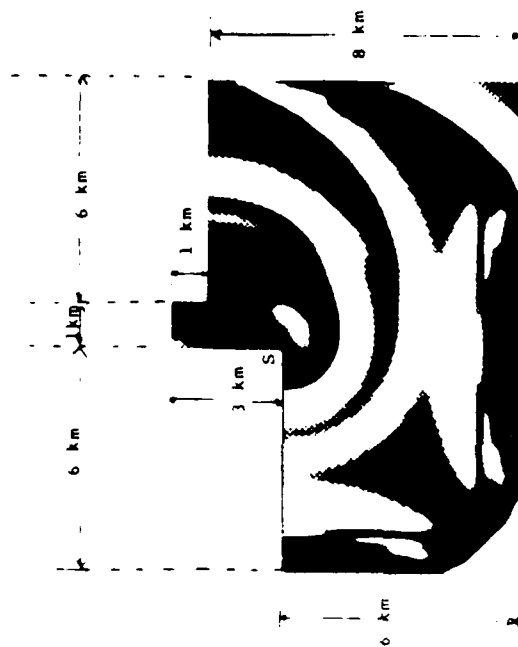


FIGURE 2/11. A Snapshot View of Wave Pattern at 1.0 sec after
The Detonation of the Source.

Case 3: Model 4 for SH-Wave

Figure 28 is the geometry of a preliminary basin model with an inclined slope of 45° . A SH-wave source function, $F_0(t)$, of the type shown in Figure 18 is located at the corner S. Figures 29-A to 29-O are the snapshots of the synthetic wavefield at 0.2 sec intervals. Two seconds after detonation of the source undesired reflections appear (after Figure 29-L) as a result of reflections from the left side of the artificially terminated boundary and 2.6 seconds (after Figure 29-M) due to the bottom boundary. Comparing the results of this case with those of Case 2, different phenomena can be seen in Figures 29-K to 29-O. Because of the sloped structure in the neighborhood of the source location, the medium is quiescent until 2.2 sec after detonation of the source. However, in Case 2, as the basin wall boundaries is vertical, there is no such quiescent period. Reflections from the vertical portion of the basin free surface wall boundaries appear to cause diffractions as soon as the waves arrive at the walls.

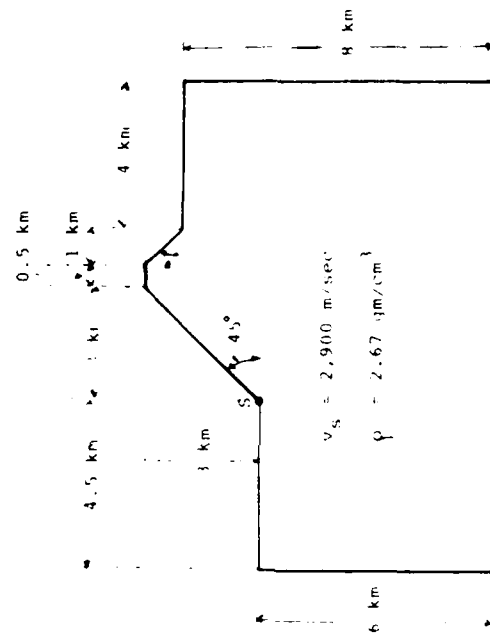


Figure 28. Preliminary Basin Model 4.

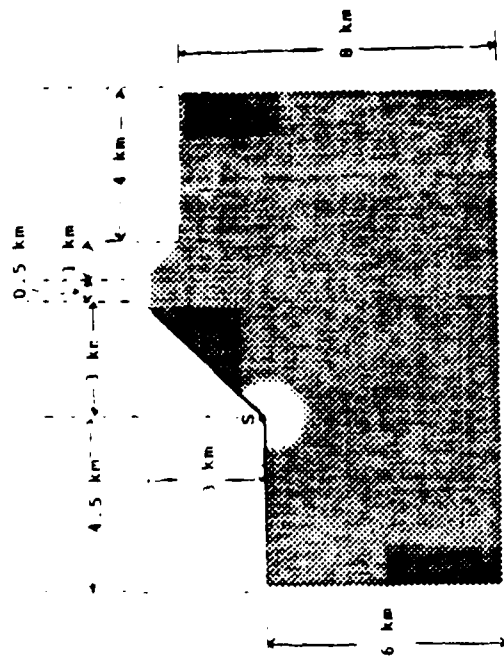


Figure 29-B. A Snapshot View of Wave Pattern at 0.4 sec after the Detonation of the Source.

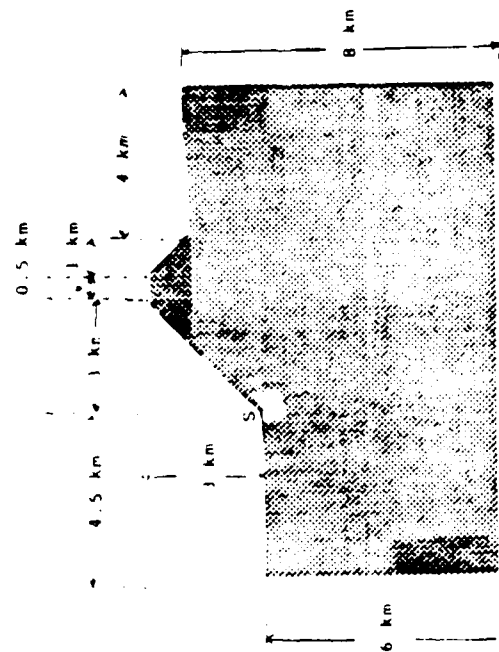


Figure 29-A. A Snapshot View of Wave Pattern at 0.2 sec after the Detonation of the Source.

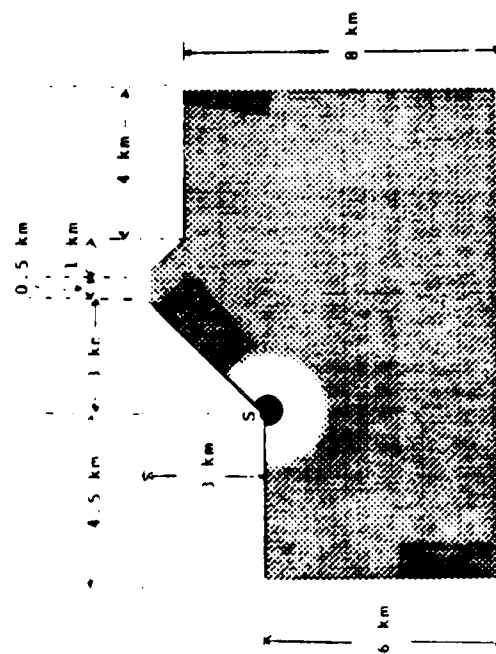


FIGURE 29-C. A Snapshot View of Wave Pattern at 0.6 sec after the detonation of the Source.

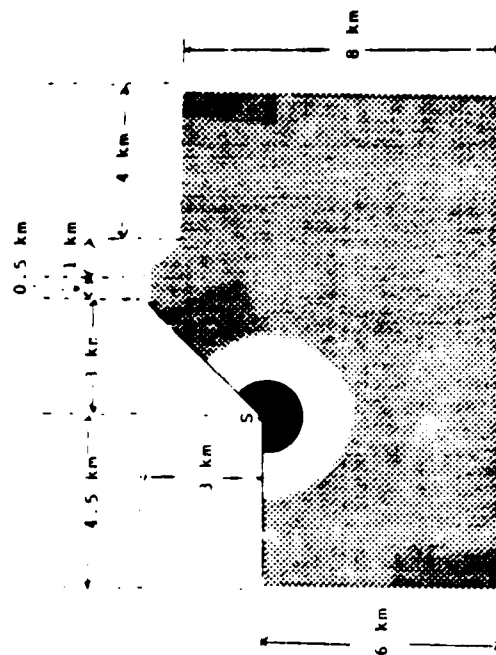


FIGURE 29-D. A Snapshot View of Wave Pattern at 0.8 sec after the detonation of the Source.

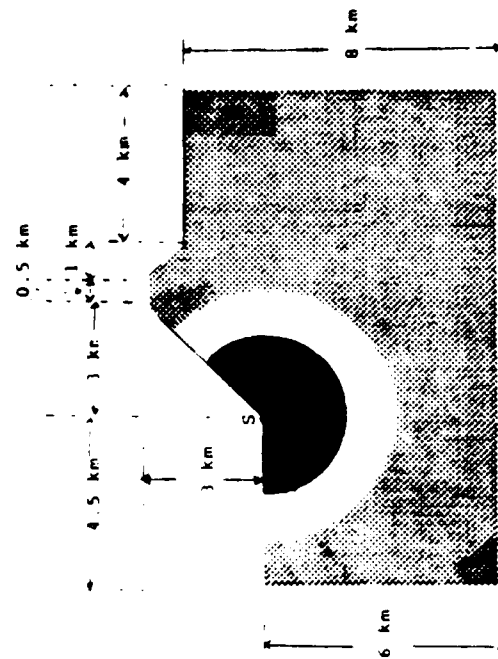


FIGURE 29-F. A Snapshot View of Wave Pattern at 1.2 sec after the Detonation of the Source.

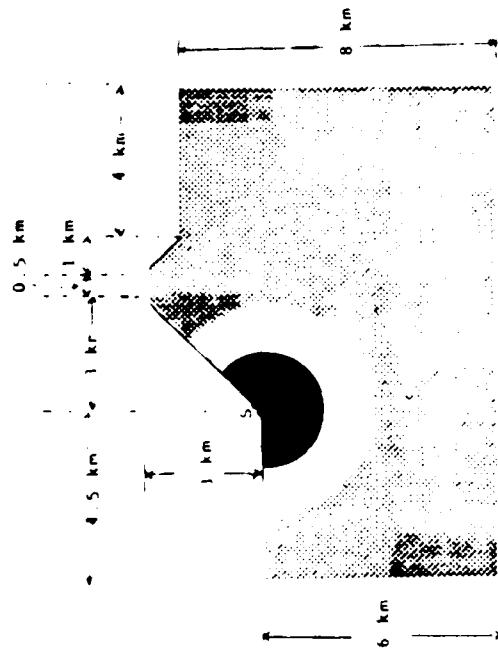


FIGURE 29-E. A Snapshot View of Wave Pattern at 1.0 sec after the Detonation of the Source.

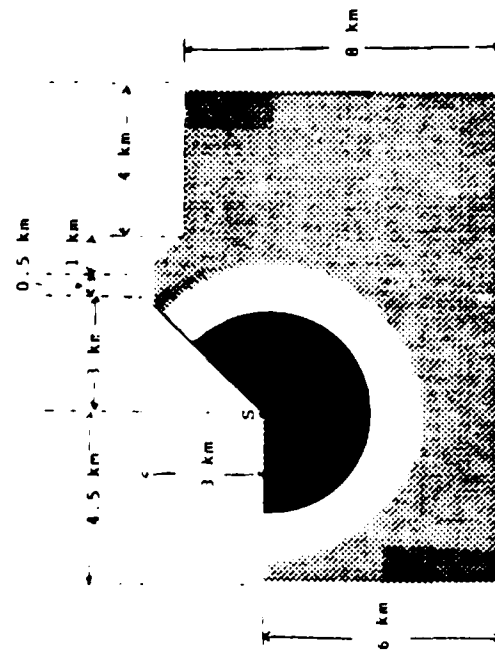


Figure 29-G. A Snapshot View of Wave Pattern at 1.4 sec after the Detonation of the Source.

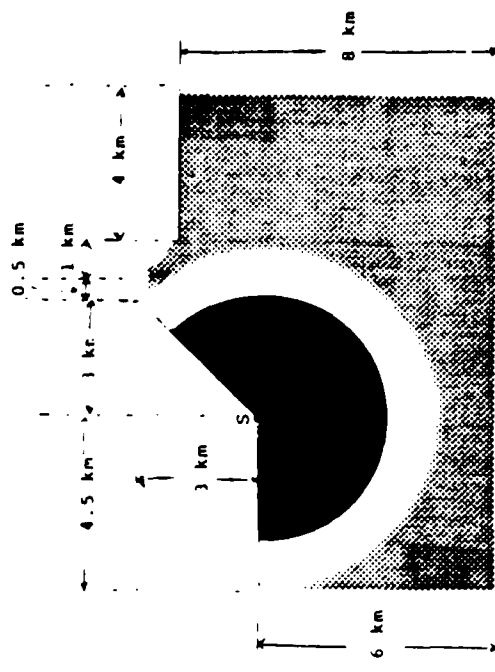


Figure 29-H. A Snapshot View of Wave Pattern at 1.6 sec after the Detonation of the Source.

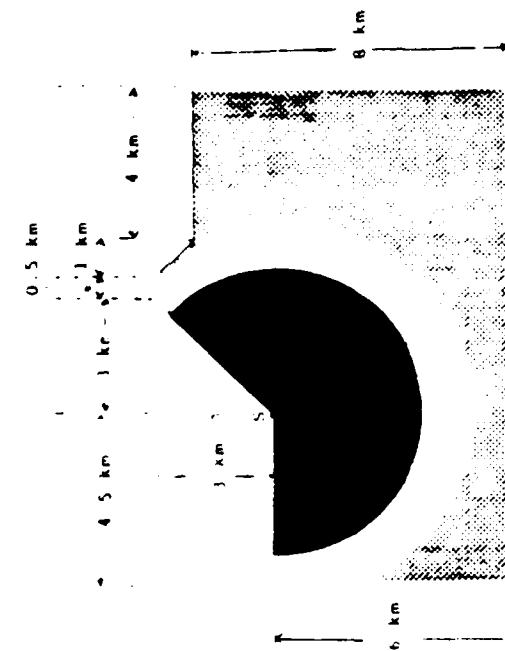


Figure 29-1. A Snapshot View of Wave Pattern at 1.8 sec after the Detonation of the Source.

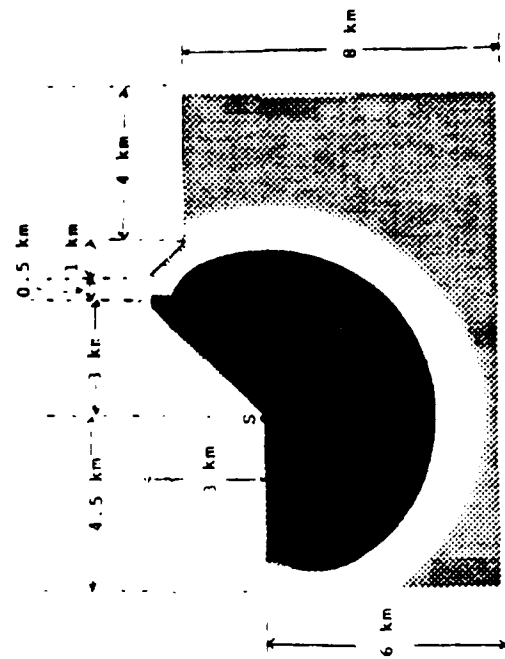


Figure 29-J. A Snapshot View of Wave Pattern at 2.0 sec after the Detonation of the Source.



Figure 29-K. A Snapshot View of Wave Pattern at 2.2 sec after the Detonation of the Source.

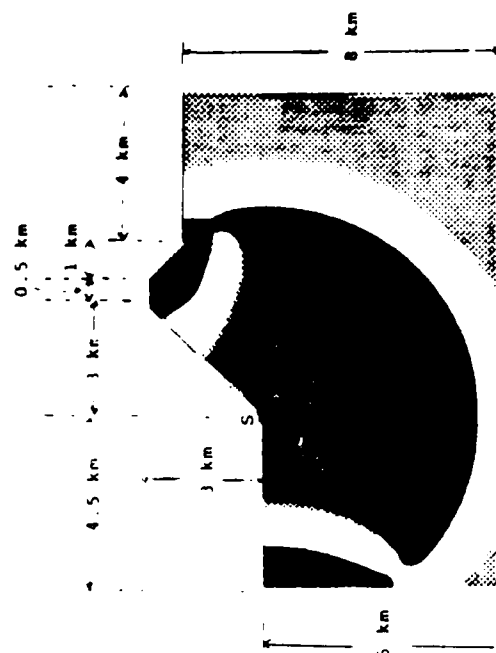


Figure 29-L. A Snapshot View of Wave Pattern at 2.4 sec after the Detonation of the Source.



Figure 29-M. A Snapshot View of Wave Pattern at 2.6 sec after the Detonation of the Source.

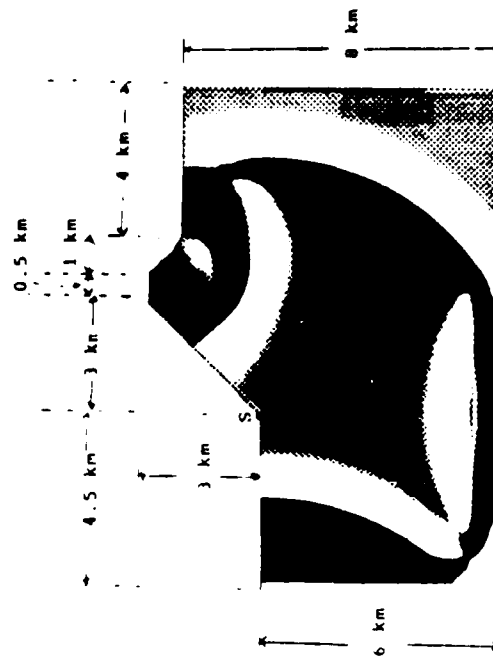


Figure 29-N. A Snapshot View of Wave Pattern at 2.8 sec after the Detonation of the Source.



Figure 29-0, A Snapshot View of Wave Pattern at 3.0 sec after the Detonation of the Source.

III. MODIFICATION AND IMPROVEMENT OF THE TWO DIMENSIONAL ELEMENT COMPUTER CODES

(1) NON-REFLECTING BOUNDARIES

Truncation of finite element models generates undesirable reflections from the truncated boundaries. Numerical analysis techniques that attempt to eliminate these undesirable reflections generally involve either viscous boundary or superposition boundaries to simulate the transparent boundaries. In frequency-domain finite element computer modeling, Lysmer and Kuhlemeyer (1969) and White et al. (1977) proposed viscous dashpots to damp out most of the reflections. However, within the framework of the time domain solutions, the viscous dashpot technique is good only for elastic body waves but not for surface waves. Also, the damping is frequency and incident angle dependent. Smith (1973) proposed a superposition method by adding two separate solutions, one with a Dirichlet and one with a Neumann boundary solution, to eliminate the artificial reflections. Although Smith's formulation is independent of both frequency and incidence angle, it requires 2^n complete dynamic solutions if there are n reflecting surfaces. This method also fails when a given wave is reflected at the same boundary more than once.

After considerable effort, we have succeeded in refining Smith's superposition method, which is referred to here as modified Smith superposition method for non-reflecting boundaries, and it summarized as follows:

(A) For one degree of freedom problems (acoustic or SH waves)

(a) Calculate the solution for Neumann's problem for each nodal point of the whole structure.

(b) Divide the solution obtained from Neumann's problem by 2 at the boundaries to obtain the expected solutions at the boundaries of each time step.

(c) Use these expected values at boundaries as feedback boundary conditions to calculate the expected responses of the interior nodal points for the same time step.

(B) For two degree of freedom problems (two-dimensional elastic waves)

(a) Calculate the solution for the mixed boundary conditions 1, i.e., normal displacement and tangential stress at the boundary are zero.

(b) Calculate the solution for the mixed boundary condition 2, i.e., tangential displacement and normal stress at the boundary are zero.

(c) Divide the tangential displacement at the boundary obtained from (i), and the normal displacement at the boundary obtained from (ii) by 2 to obtain the recovered displacement components at the boundaries at each time step.

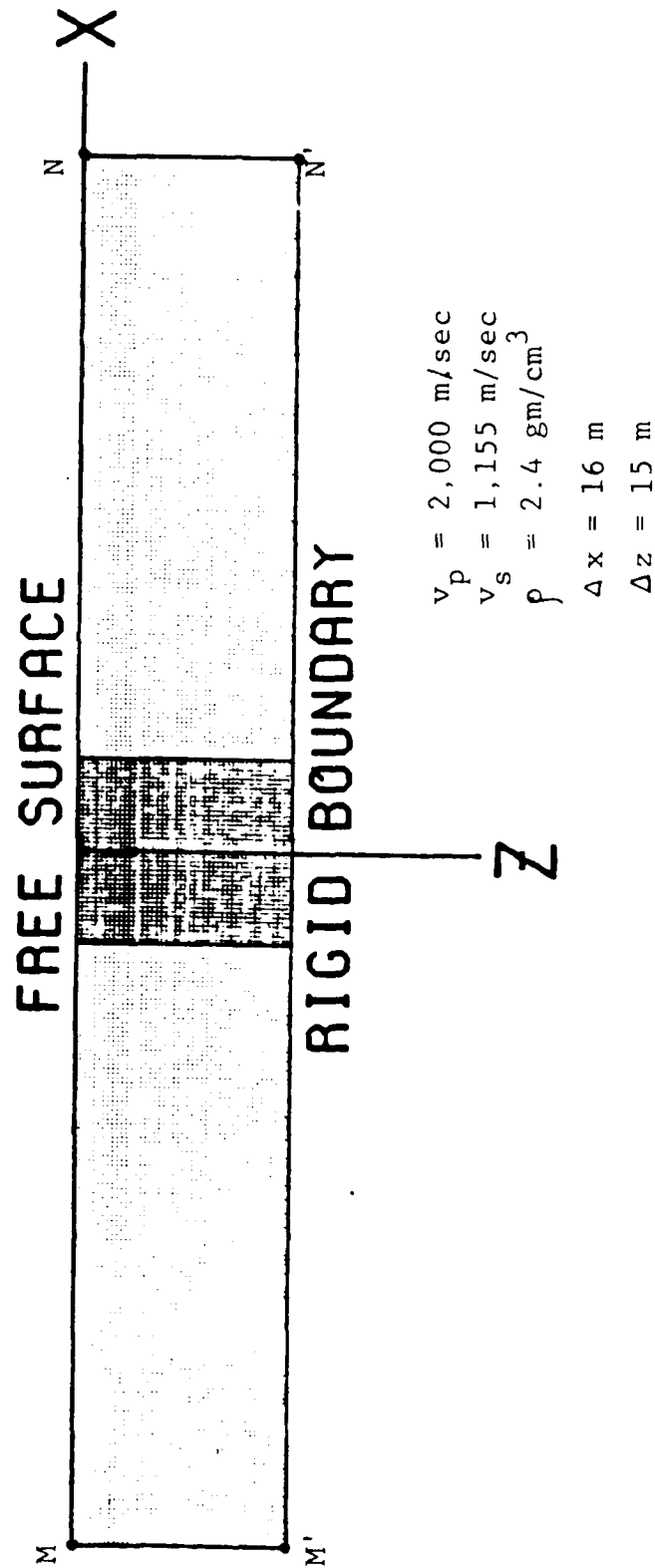
(d) Use these expected values of the displacements at the boundaries as the feedback boundary conditions to calculate the expected responses of the interior nodal points for the same time step.

The proposed approach avoids the need for 2^n complete solutions if there are n reflecting surfaces. However, this method still fails when a given wave is reflected at the same boundary more than once.

The following are two finite element modals to demonstrate the cancellation of reflections.

Example 1:

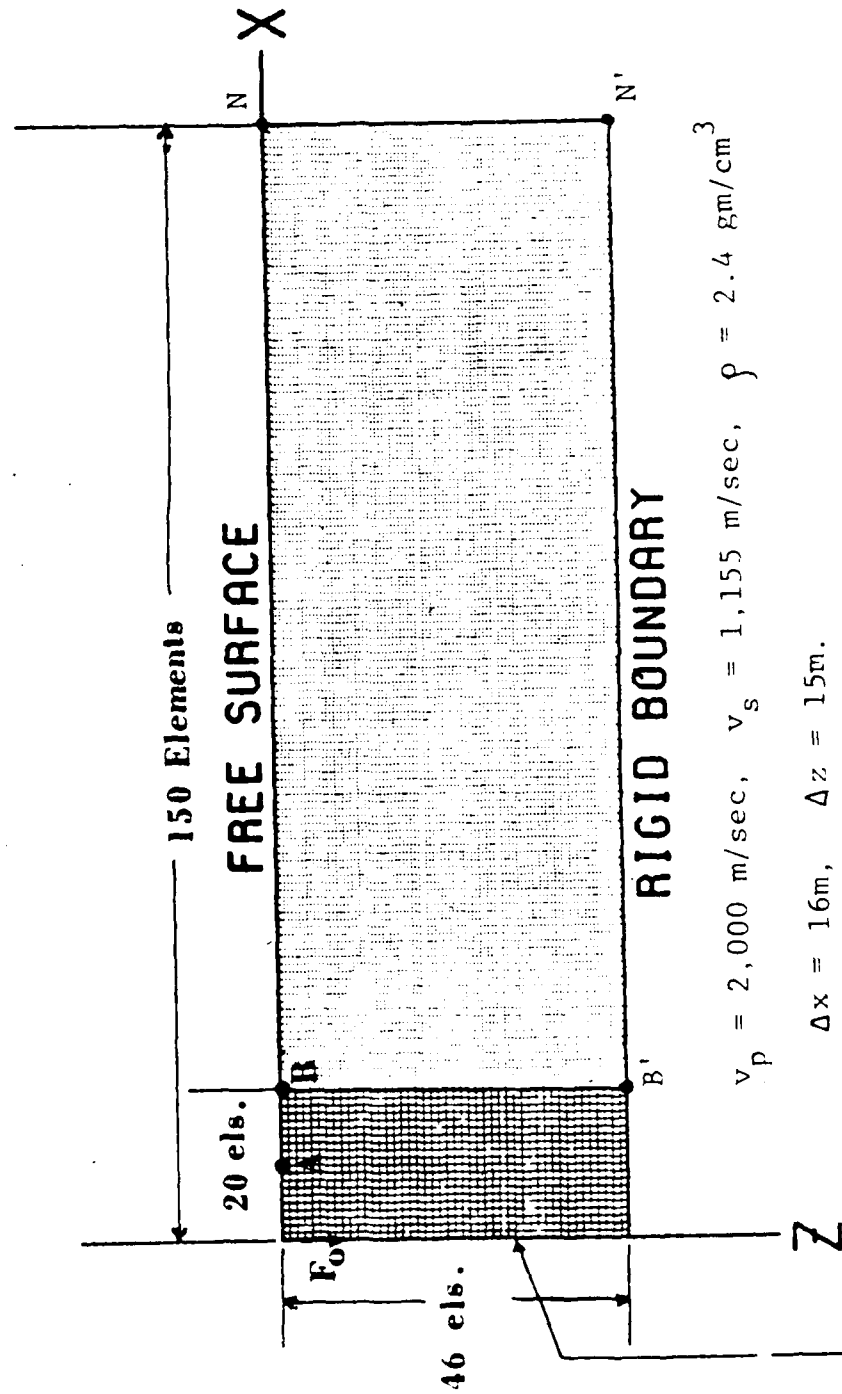
An infinite long elastic plate, bounded by an upper free surface and a lower rigid surface, with wave velocities $V_p = 2,000$ m/sec, $V_s = 1,155$ m/sec, density $\rho = 2.4$ gm/cm³ (Figure 30a). Symmetry is used by letting the horizontal displacement along z-axis be zero to reduce the size of the problem (Figure 30b). We use an internal forcing function, F_0 , with a time step $= 5.0 \times 10^{-3}$ sec. The observation points are located at A and B. The grid sizes are $\Delta x = 16$ m and $\Delta z = 15$ m. First, we construct a model of sufficiently large size (150 x 46 elements), to obtain the required solution before the arrivals of the reflection from the side boundaries (MM' and NN' in Figure 30a). Then we construct a model of smaller size (20 x 46 elements) with the application of above described non-reflecting boundary conditions along BB' to simulate an infinite medium in the x-direction. Figures 31-A and 31-B compare the displacement components observed at point B between the two different kinds of the solutions. The dotted curves are the expected results; the solid curves are the averaged values obtained with free and rigid boundary conditions on BB'. The deviation between the two different kinds of solution starts at the twenty-first time step numerically. Figures 32-A and 32-B show the comparison of the expected results and the non-reflecting boundary solutions based on the modified Smith superposition method observed as the same boundary point, B. Exact cancellation of the reflected waves at the boundary has been effectively achieved until the boundary BB' becomes the second-time reflecting boundary for a given ray. Figures 33-A and 33-B are the comparison of the two kinds of solutions observed at point A; the deviation would have started at the thirty-first time step without applying the non-reflecting boundary conditions.



FINITE ELEMENT MODEL I

Figure 30a. Finite Element Model for an Infinite Elastic Plate.

(Dark Region is the simulated infinite plate with the use of the non-reflecting boundaries.)



FINITE ELEMENT MODEL I

SYMMETRIC
BOUNDARY

Figure 30b. Finite Element Mesh for an Infinite Elastic Plate with the Use of the Symmetric Boundary Conditions.

OBSERVED AT POINT B (MODEL I)

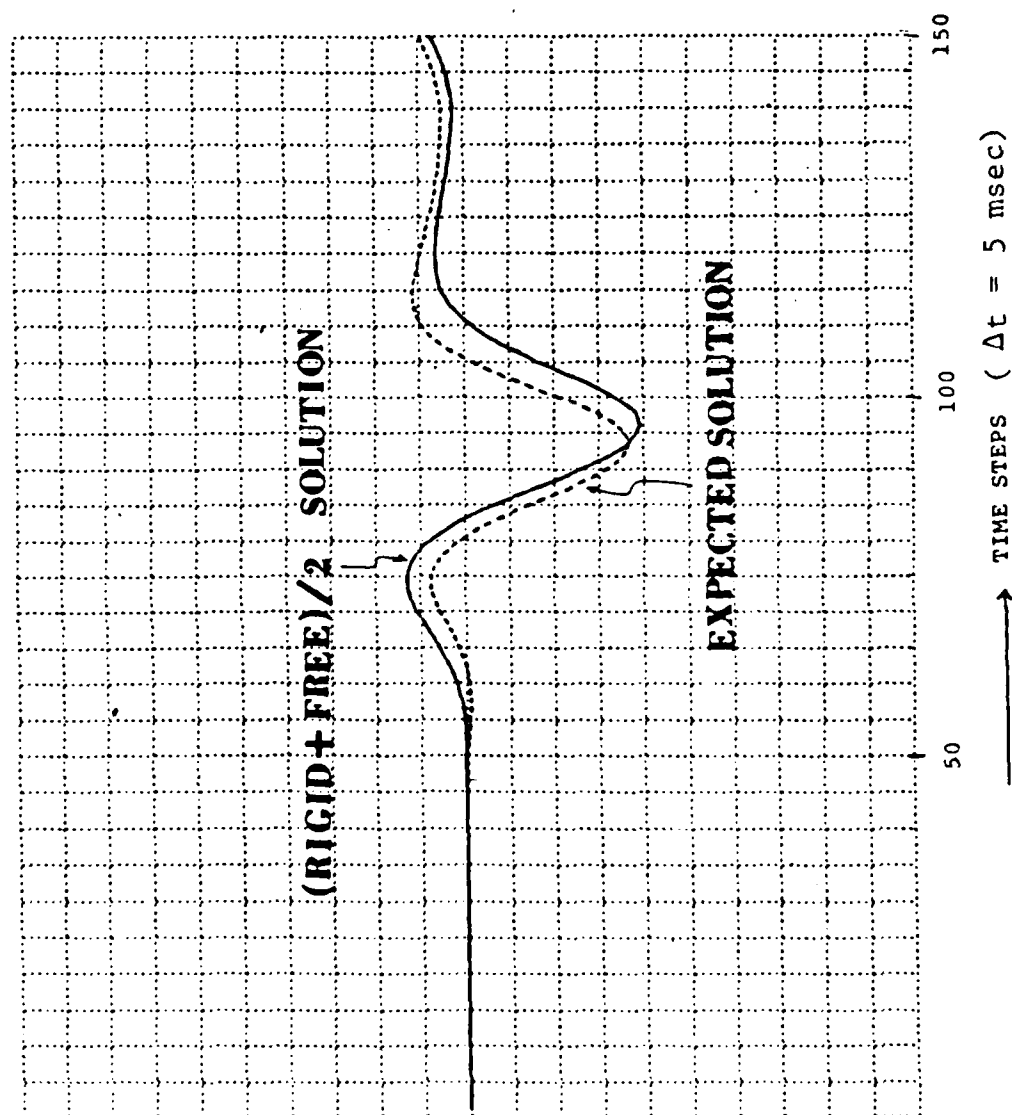


Figure 31a. Comparison of Vertical Displacements.

HORIZONTAL DISPLACEMENT

OBSERVED AT POINT B (MODEL I)

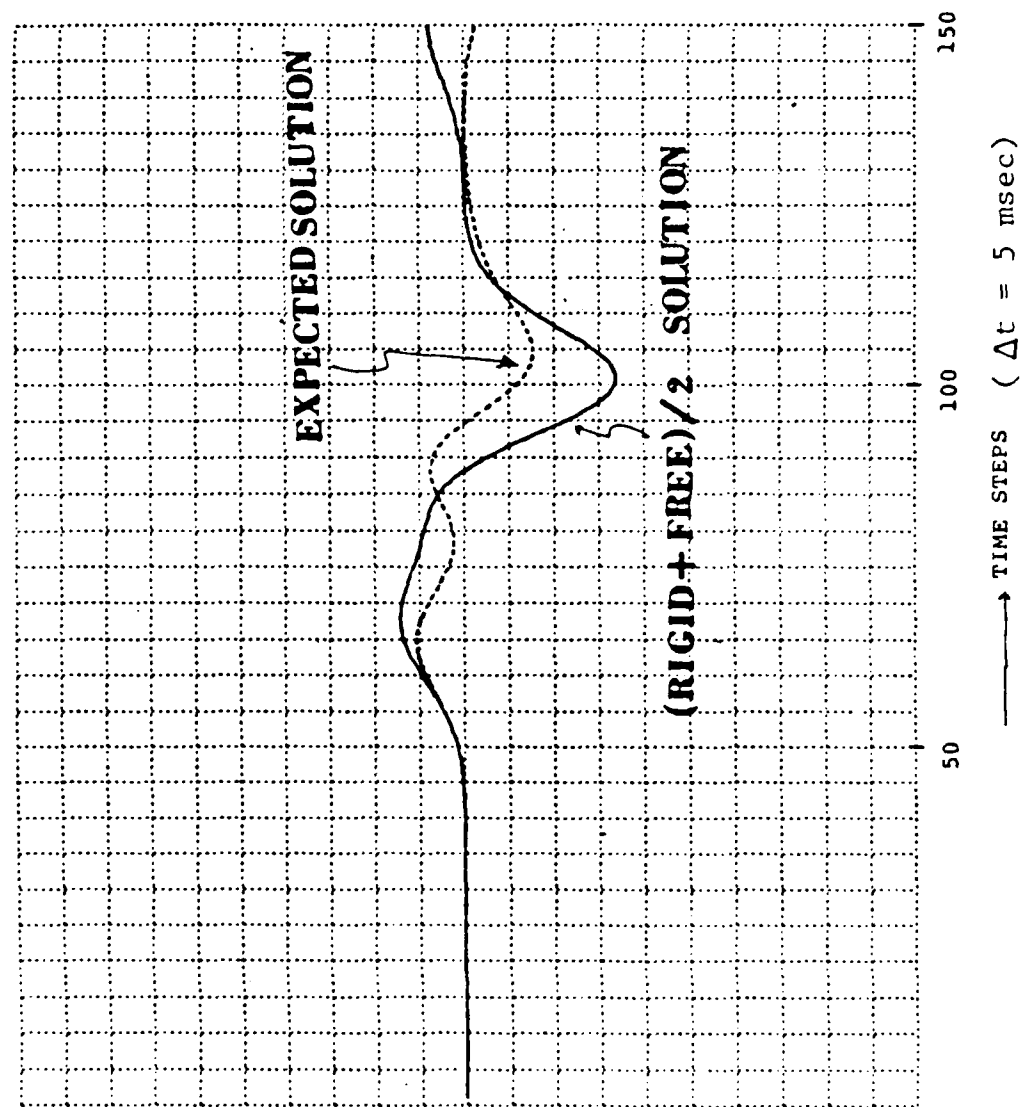


Figure 3lb. Comparison of Horizontal Displacements.

OBSERVED AT POINT B (MODEL 1)

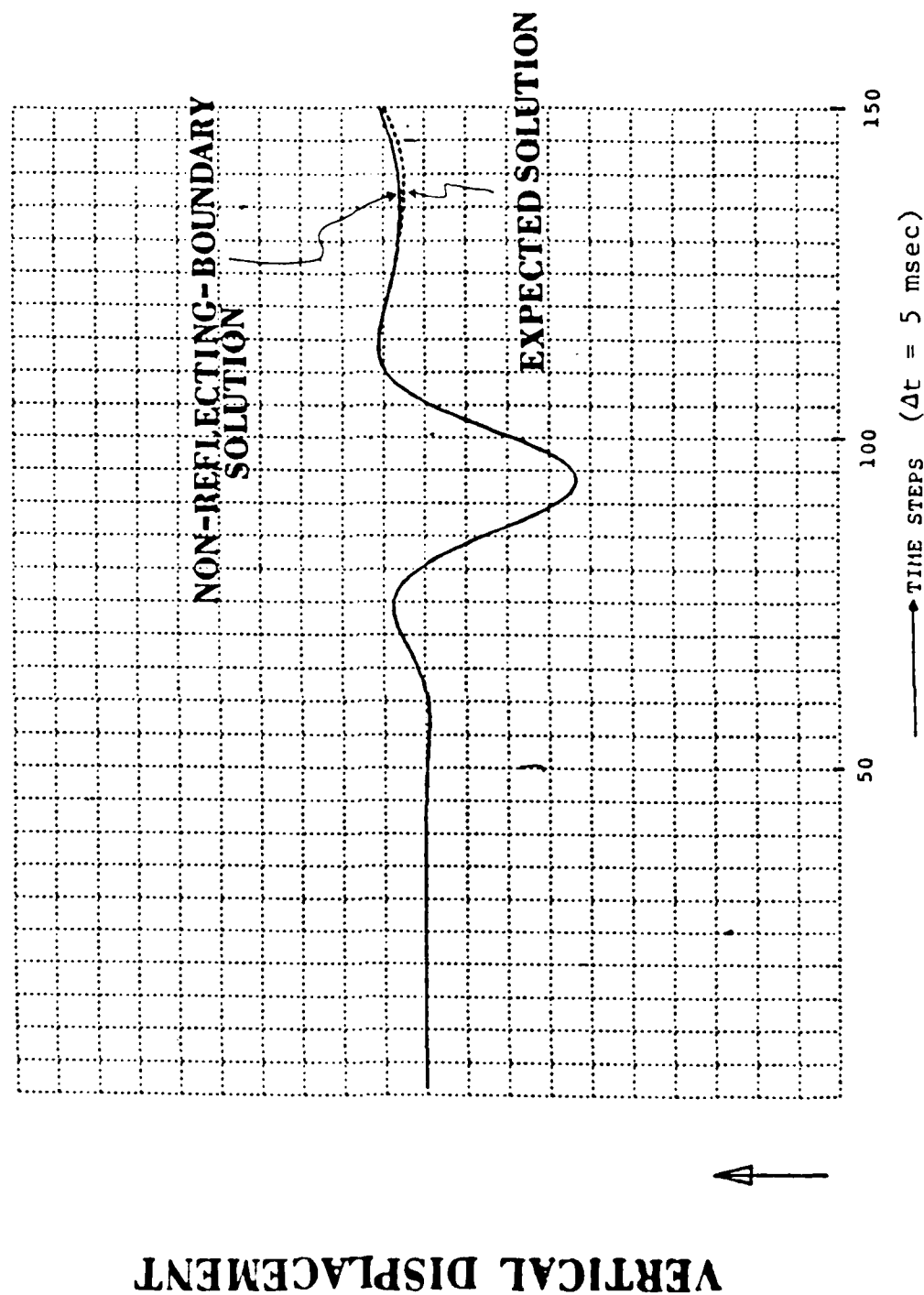


Figure 32a. Comparison of Vertical Displacements.

OBSERVED AT POINT B (MODEL 1)

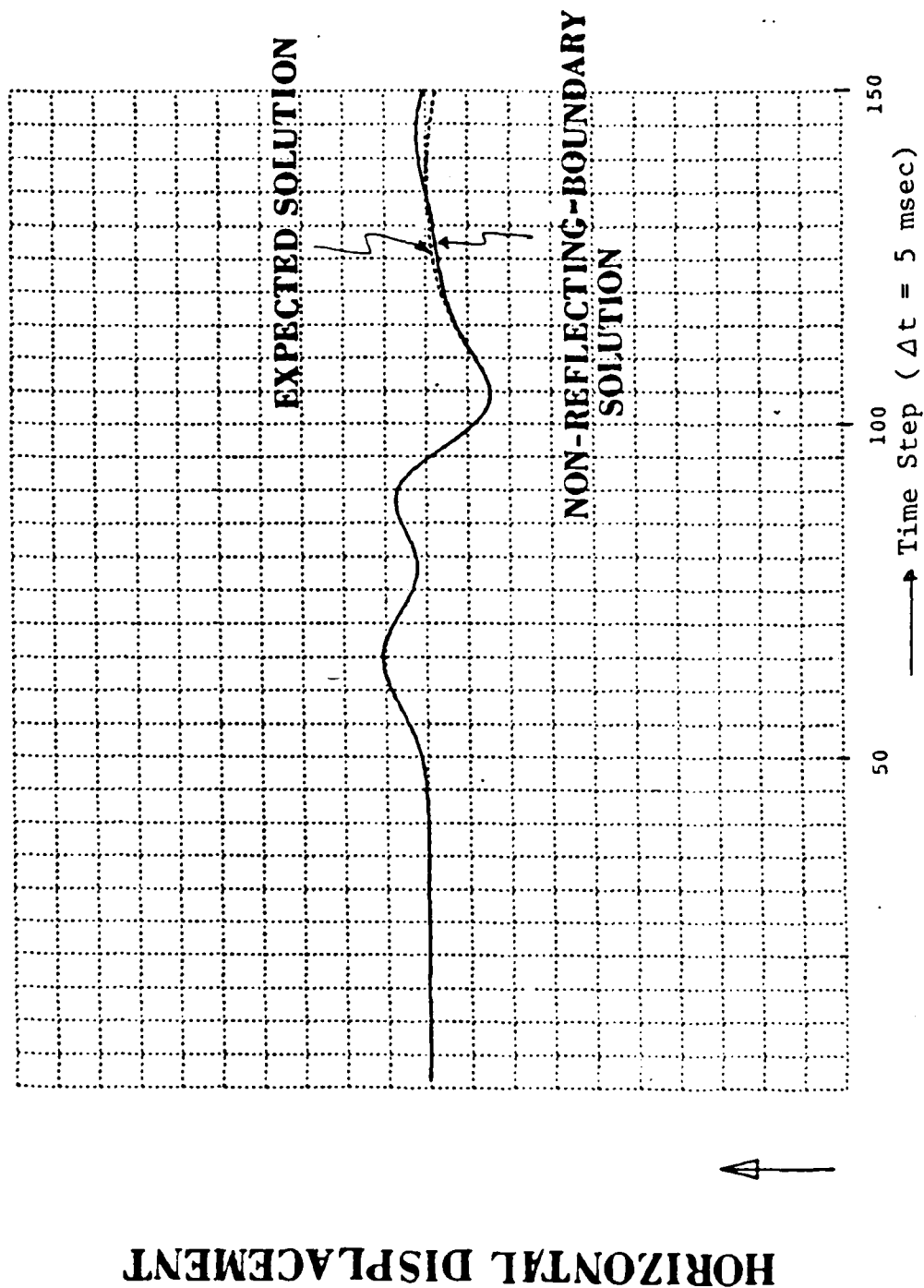


Figure 32b. Comparison of Horizontal Displacements.

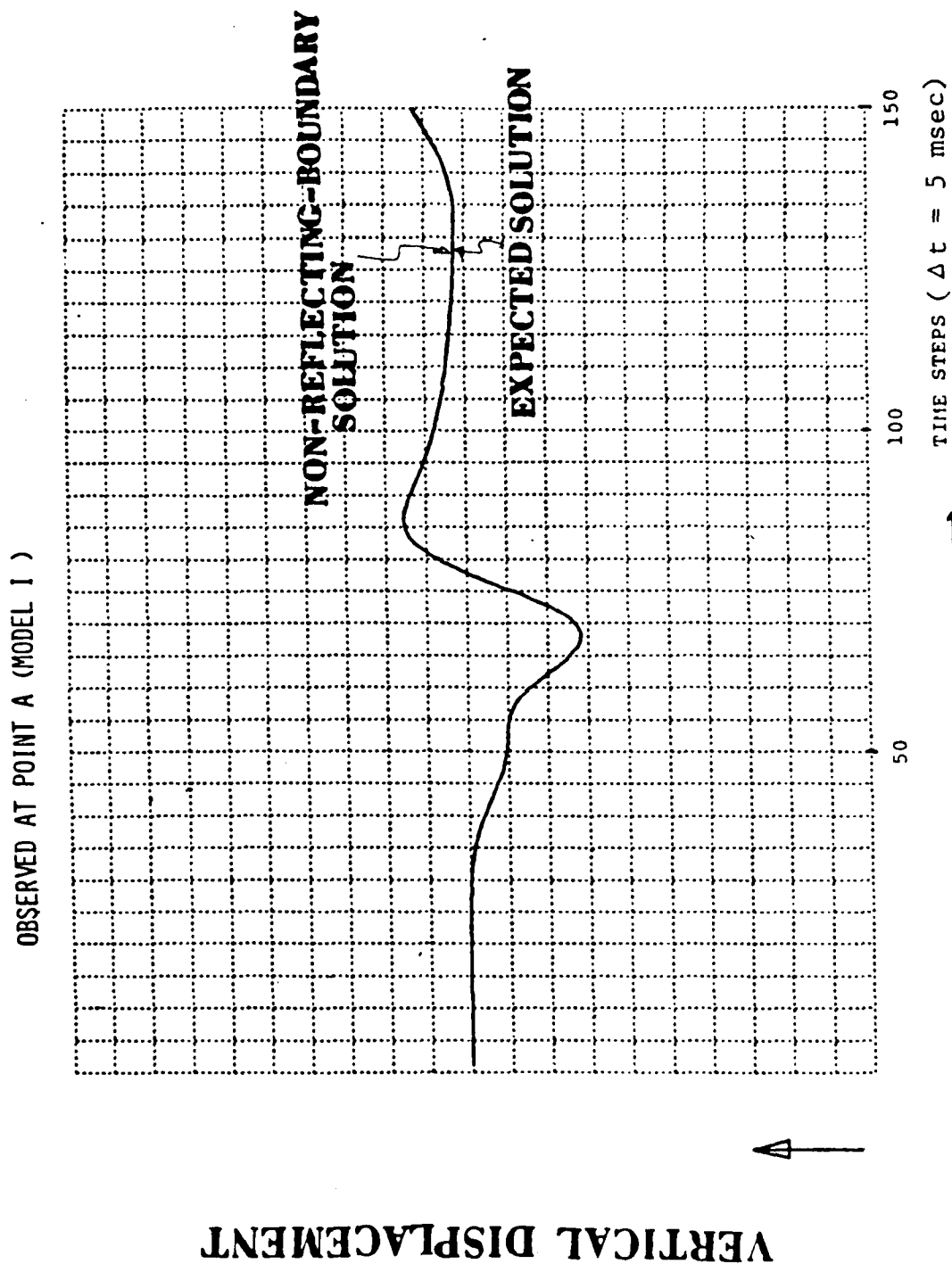


Figure 33a. Comparison of Vertical Displacements.

OBSERVED AT POINT A (MODEL I)

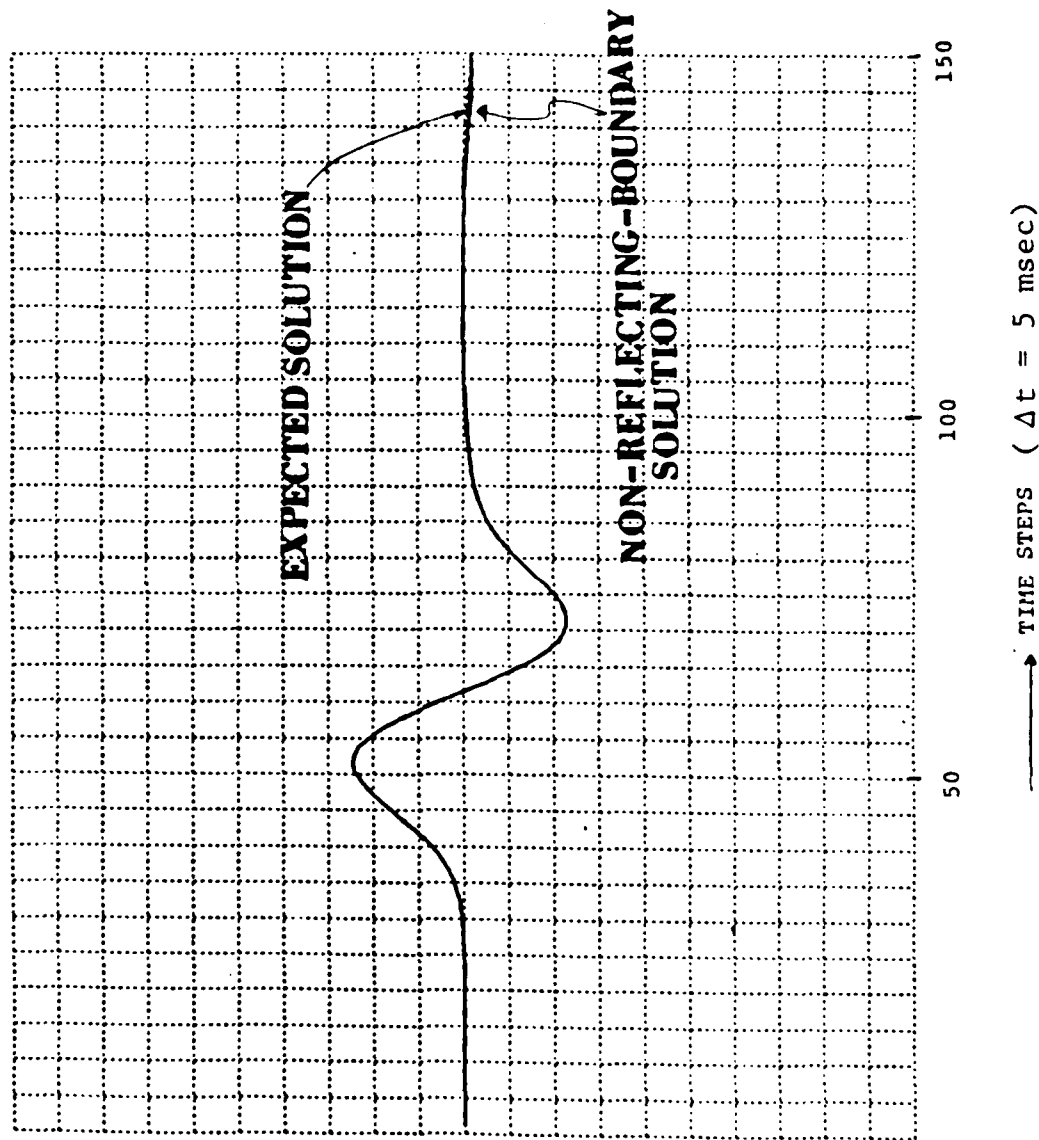
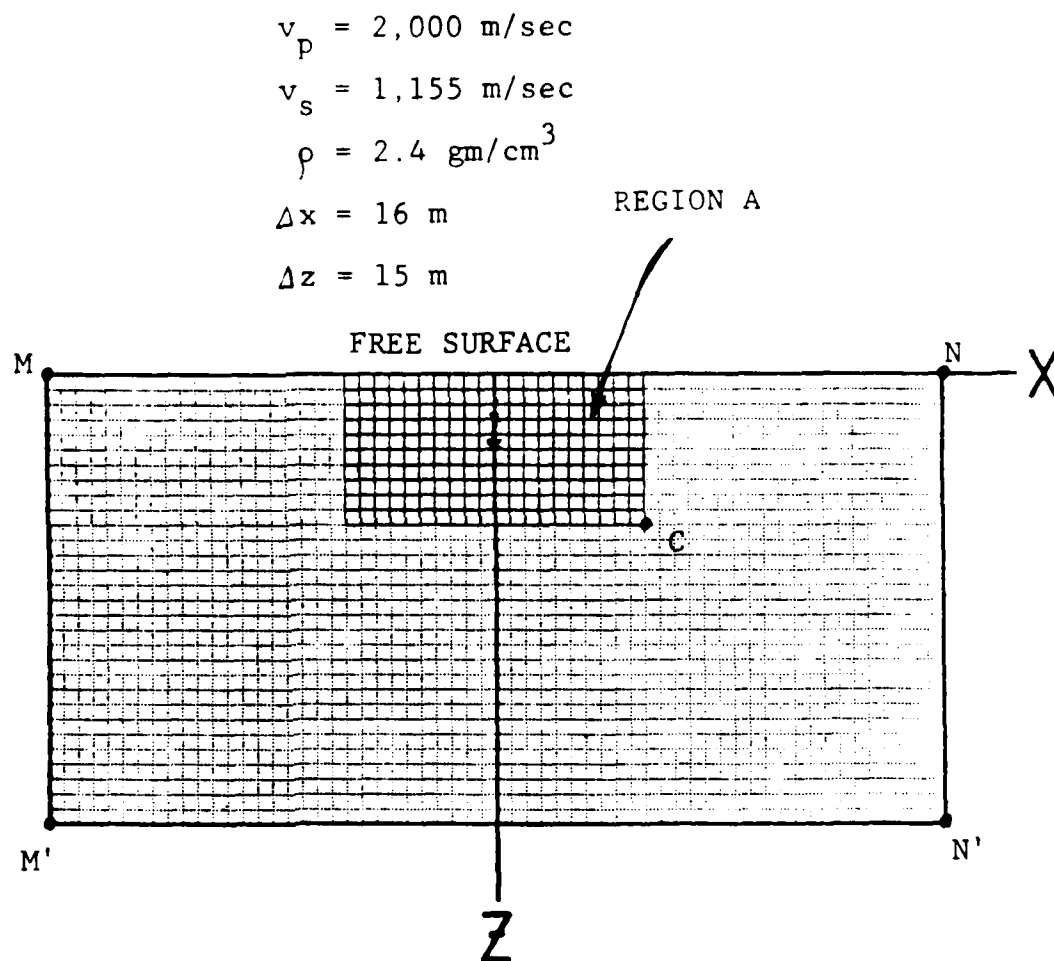


Figure 33b. Comparison of Horizontal Displacements.

Example 2:

In Example 1 we demonstrate the effect of using non-reflecting boundary conditions on a single boundary. In this second example, the non-reflecting boundary conditions are applied to two boundaries. The model is a half-space with the same elastic medium as Example 1 with an internal source (Figure 34a). Again only half of the problem is modeled due to symmetry (Figure 34b). Two models of different sizes are constructed: the large one (60x60 elements) generates the expected solutions; the small one (20x20 elements) is to test the non-reflecting effect. The small model contains only OABC. Figures 35a and 35b show the responses as observed at corner C (see Figure 34). The expected responses are obtained by using the large model containing OA'B'C', and the other solutions are obtained by using the small model in which both AC and BC are imposed with free boundary conditions. It is evident that the expected solutions for both the vertical and horizontal components do not agree with the traction-free boundary solutions. Analytically, corner C is singular. However, in the finite element algorithm, the non-reflecting boundary conditions based on the modified Smith superposition method can be successfully applied to point C. Figures 36a and 36b show the agreement between the above expected solutions and the non-reflecting boundary solutions. Again, this non-reflecting technique fails when a given wave is reflected at either boundary more than once.



FINITE ELEMENT MODEL II

Figure 34a. Finite Element Model for an Elastic Half-Space. (Region A is the simulated half-space with the use of non-reflecting boundaries.)

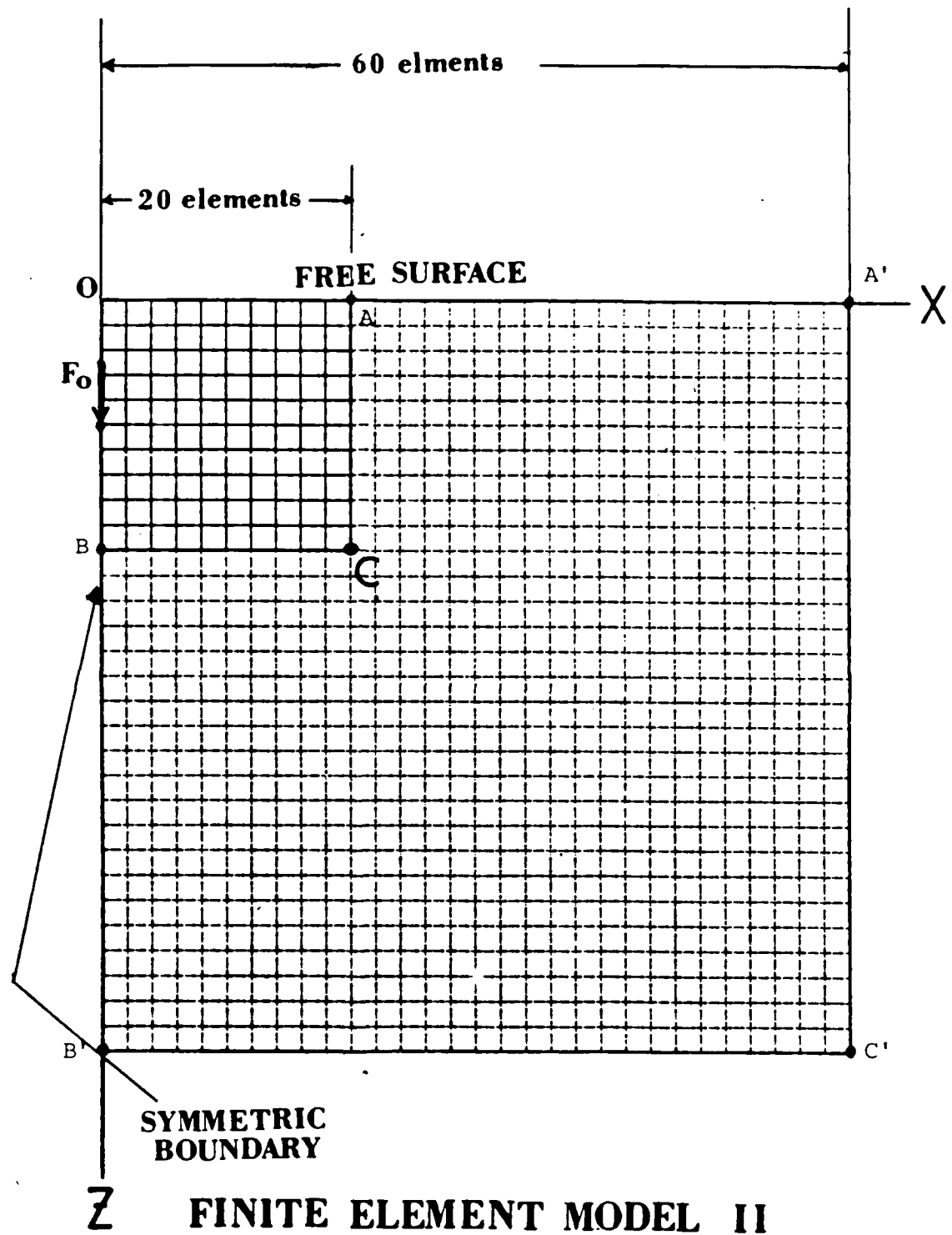


Figure 34b. Finite Element Mesh for an Elastic Half-Space with the Use of the Symmetric Boundary Conditions.

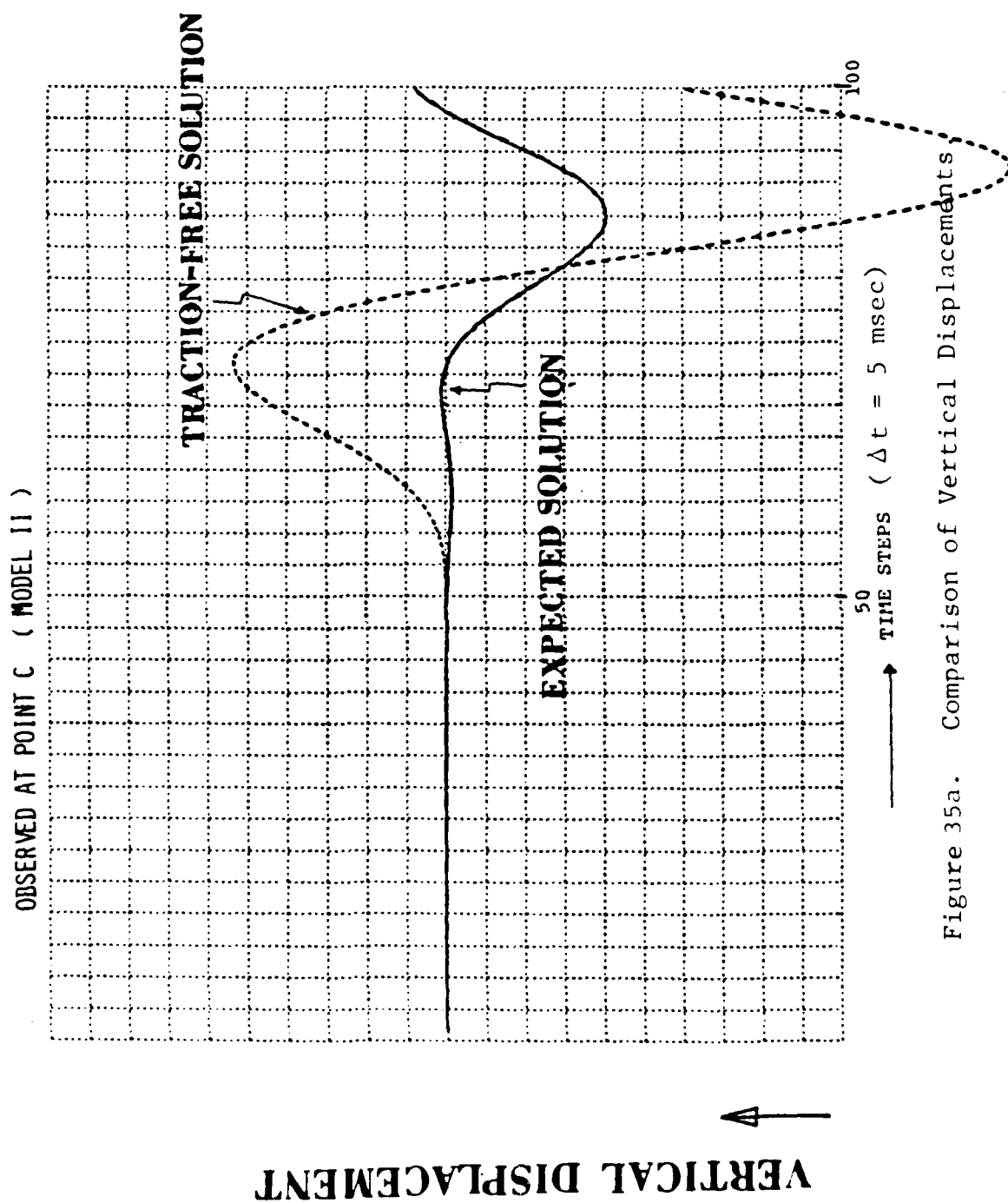


Figure 35a. Comparison of Vertical Displacements.

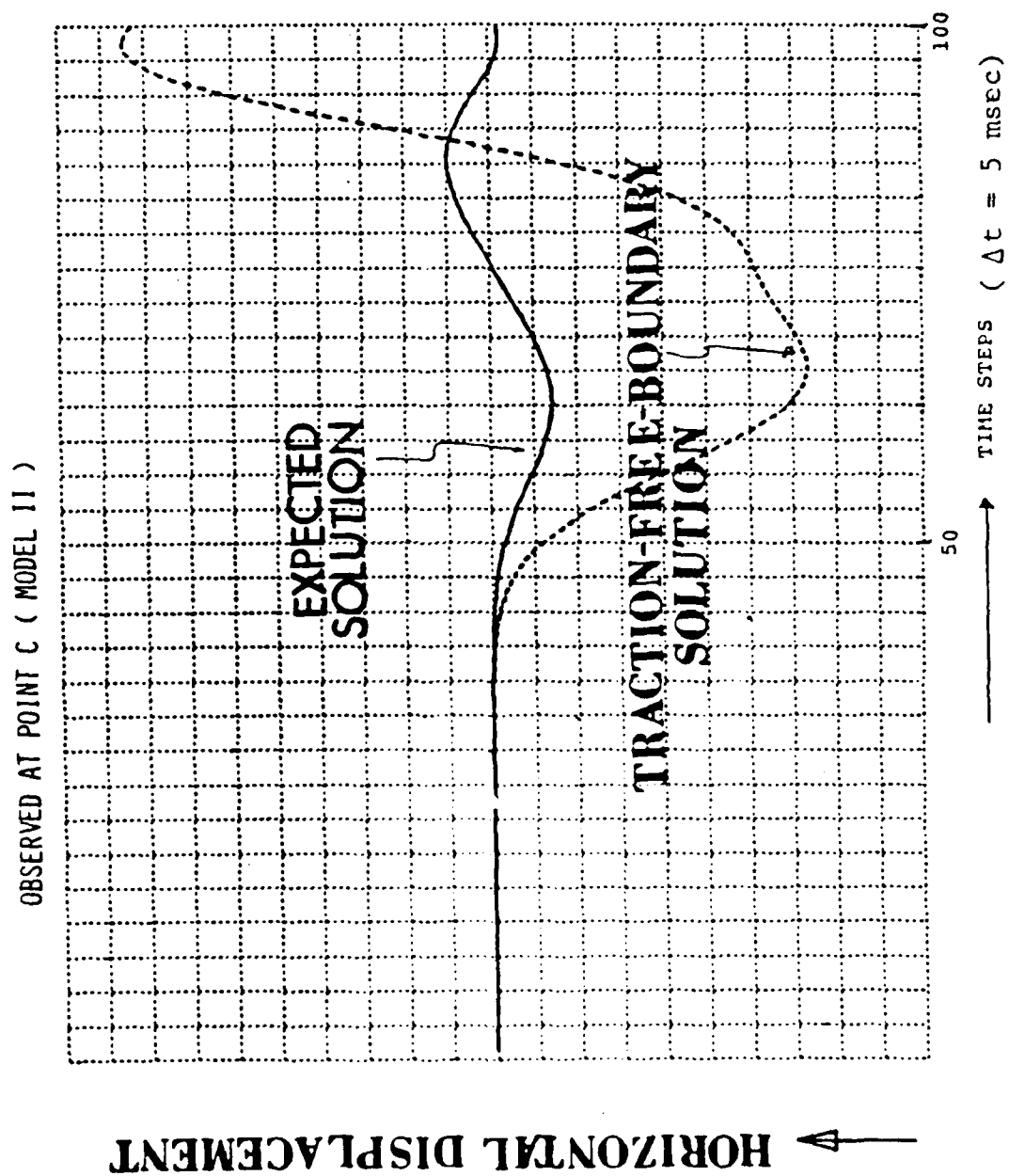


Figure 35b. Comparison of Horizontal Displacements.

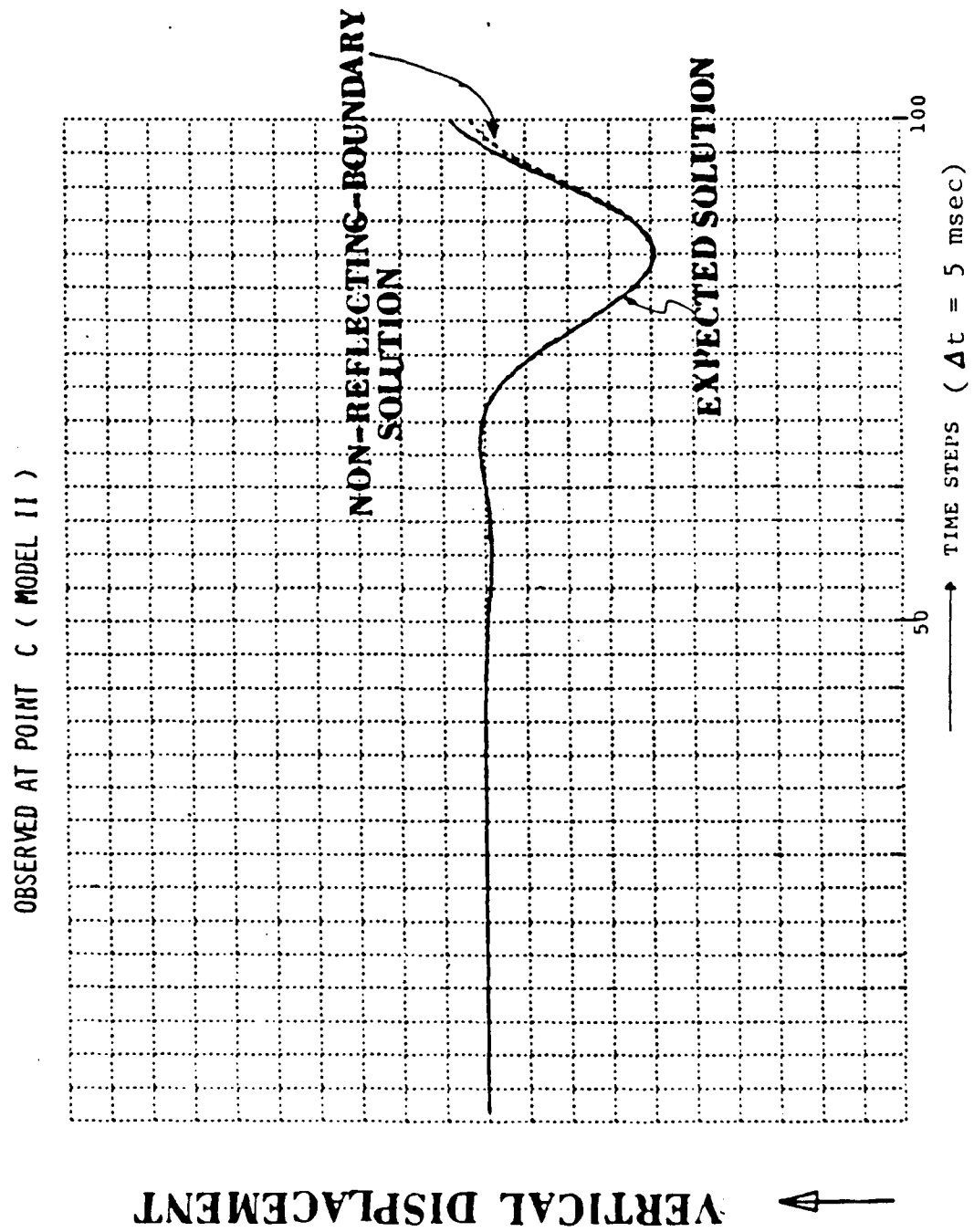


Figure 36a. Comparison of Vertical Displacements.

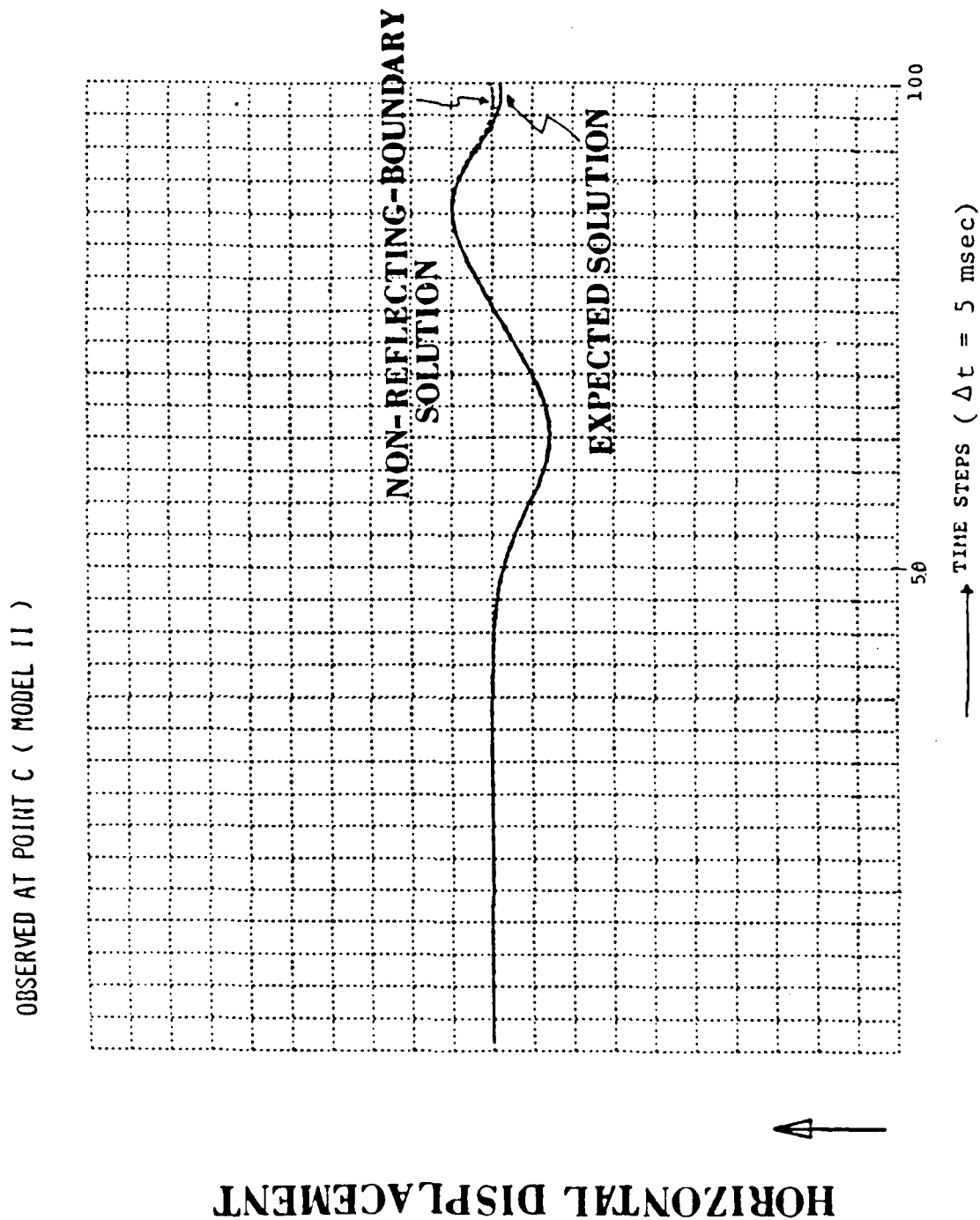


Figure 36b. Comparison of Horizontal Displacements.

(2) EFFECTIVE EXCITATION (EE) METHOD

As mentioned in the Final Report of Contract F49620-77-C-0130, "Elastic and Visco-elastic Wave Scattering and Diffraction" (1977-1980), we used the direct step-by-step explicit central-difference time integration scheme in AFEA3. Consequently, when the structure is subjected to an external disturbance, only the neighboring nodal points of the source are primarily excited while all other nodal points remain virtually undisturbed. The region of excitation motion expands with increasing time steps. For instance, we first consider a two-dimensional finite element mesh as shown in Figure 37. If the source is located at point S, for the first time step we need only (i) to calculate the displacements, velocities, accelerations of those nodal points within the area $A_1B_1C_1D_1$, including the nodal points, and only (ii) to assemble the stiffness and mass matrices for those elements within the area $A_2B_2C_2D_2$. For the second time step, only those nodal points within the areas $A_1B_1C_1D_1$ and $A_2B_2C_2D_2$ and the elements within the area $A_3B_3C_3D_3$ are effectively excited, and so on. The same concept can be generalized to the three-dimensional case. In the Aldridge preliminary two-dimensional finite element code AFEA, the displacements, velocities, accelerations for every nodal point must be calculated for every time step. Consequently, the EE-method saves a large amount of computing time in the early stage of computation particularly for large finite element models.

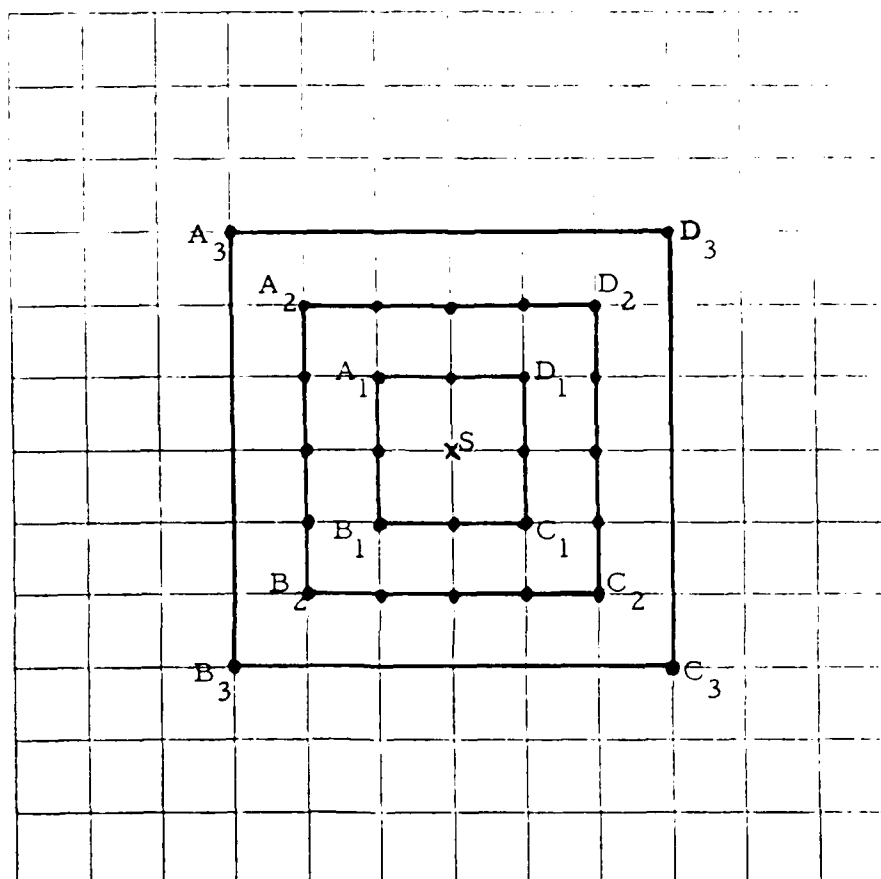


Figure 37. Two Dimensional Effective Excitation Finite Element Mesh.

(3) INTRODUCING RELATIVE COORDINATES OF THE NODAL POINTS

In the old version of the AFEA, the mesh generator generates the value of the coordinates of the four nodal points of each quadrilateral, either a 4-CST (Constant Strain Triangles) or an averaged 2-CST quadrilateral element, with respect to the global system (Figure 38)

$$AX(n), BX(n), CX(n), DX(n)$$
$$AY(n), BY(n), CY(n), DY(n)$$

where $n = 1, 2, 3, \dots, N$, and N is the number of the total elements. Thus, we require incore storage with $8 \times N$ words for the eight variables. Actually, we need only assign the relative coordinates of one element since we are temporarily dealing with regular sized elements. The introduction of the relative coordinates is based on the fact that both the shape function $[N]$ and the strain-displacement matrix $[B]$ of the triangular elements depend only on the relative coordinates of the element. Thus, in the new version of AFEA, we need only eight incore words for these eight variables.

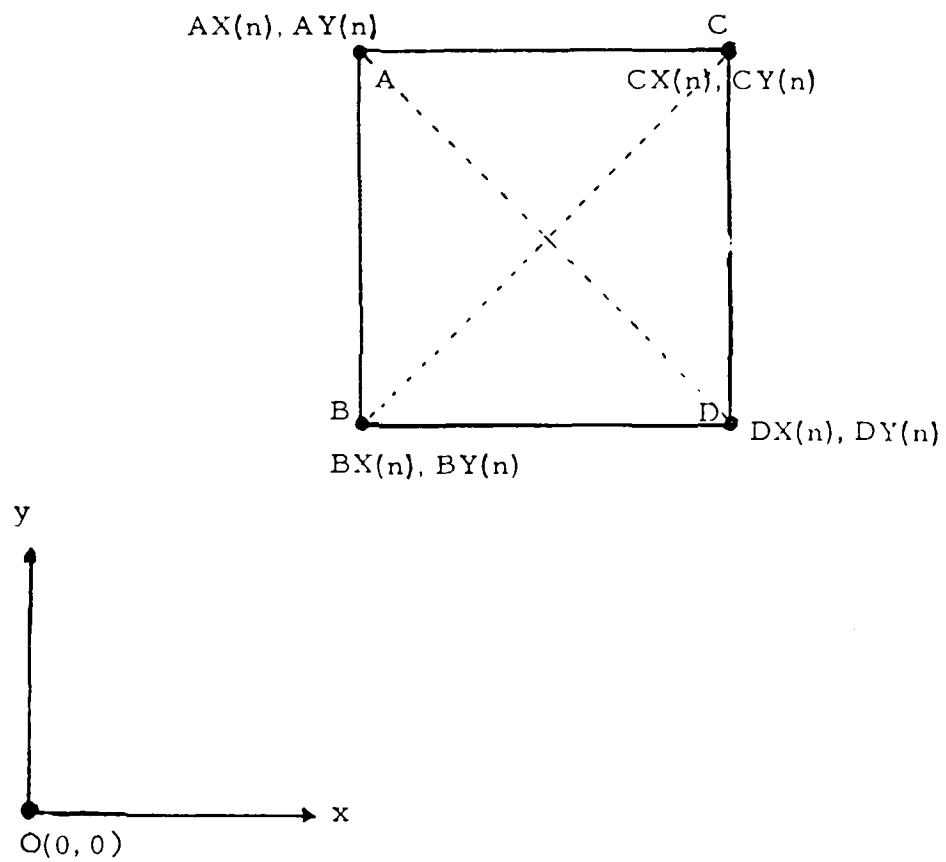


Figure 38. The Coordinates of the n^{th} Element.

(4) RESTART/BACK-UP OPTION

In the new version of the two-dimensional computer code, we have included a restart/back-up option. That is, we save the displacements and velocities of every nodal point after a certain number of time steps. The new back-up results will overwrite on the same tape to replace the old back-up results. If the integer IFLAG has the value zero, the option will start from the beginning; any other values of IFLAG will cause the option to restart from its last executed time step. This feature greatly facilitates efficiency of computation in case of a computer failure.

(5) AVERAGING 2CST FORMULATION

In the old version of our two-dimensional finite element codes, (SH-wave and Elastic Wave Cases), we used 4-CST (Constant Strain Triangles) quadrilateral elements in order to avoid the space-grid skewness. The degrees of freedom of the internal node, such as node 5 in Figure 39-A, are statically condensed. The degrees of freedom of such nodes do not appear in the global assemblage equations so that the storage during the computation is reduced considerably. The 4-CST formulation has been a very good approach to obtain solutions for static cases. However, in the 4-CST algorithm for the dynamic case, it was assumed that the internal condensed nodal points for each quadrilateral element were subjected to no inertial forces. In the present modified version of these codes, an averaged 2-CST algorithm is adopted. In Figure 39-B, a quadrilateral is composed of two triangles. Two distinct ways of subdividing the quadrilateral are given. Therefore, the assembled quadrilateral stiffness matrix can be obtained by a linear interpolation without any internal condensation. Based on the averaged 2-CST formulation, a better approximation of the solution can be obtained.

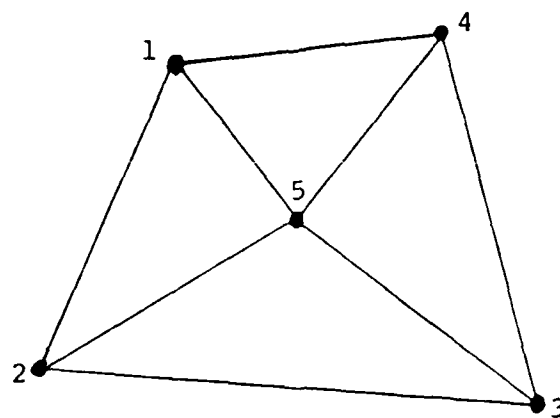


Figure 39-A. A 4-CST Quadralateral Element.

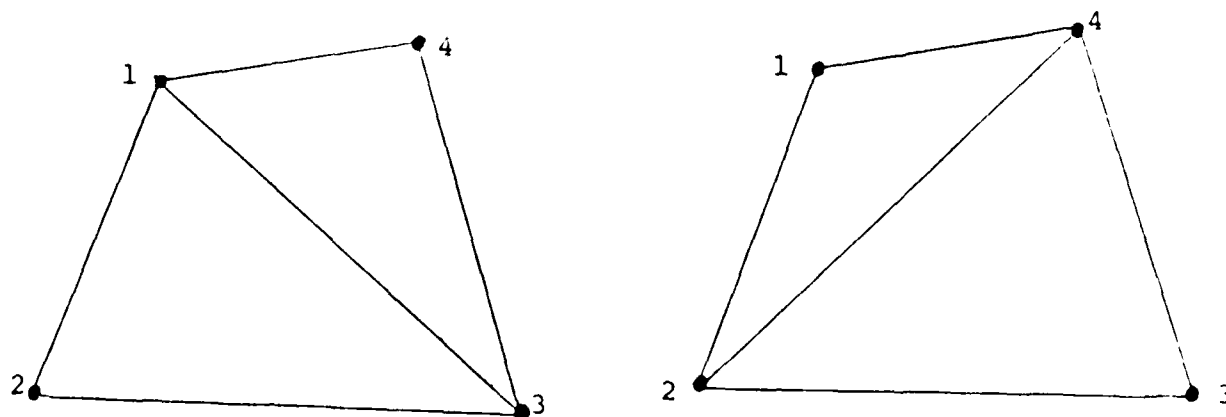


Figure 39-B. Two 2-CST Quadralateral Elements.

(6) Nodal-Point-Oriented Approach

In the old version of our two-dimensional finite element codes, the global stiffness matrix is obtained by the assemblage of the stiffness matrix of each individual quadrilateral element for each time step in the time integration.

In the present modified version of the codes, the global matrix involves only the non-zero stiffness matrix members for each nodal point before time integration.

The advantages of the old codes are:

- (i) The incore storage required is very little. Only the products of the global stiffness matrix and displacements are stored.
- (ii) There will be less chance of making mistakes, particularly for source mechanism problems.

The advantages of the new codes are:

- (i) The computing time is drastically reduced since local assemblages for each time step are avoided. The amount of the reduced time depends upon the size, and the property of each individual problem. For a model of 40×40 elements, the computing time using the new version program is only $1/5$ of that using the old version.
- (ii) The disk storage for the problem with irregular element meshes is the same as that of the problem with a regular size element mesh.

In both the versions, the 2-CST formulation and effective excitation method are used. The restart/back-up option is also introduced into the new version codes.

IV. FINITE ELEMENT SOURCE MECHANISM

The finite element simulation of a non-directional line or a point source, (cylindrical source for two-dimensional problems, or a spherical source for three-dimensional problems), for the two- or three-degree-of-freedom elastic wave case has been a very challenging subject. The simplest or the most natural way to excite the elastic medium is to apply a directional forcing function to the structure. Likewise, for the one-degree-of-freedom problem, special effort is needed to simulate a coupled source. By using an energy-sharing-nodal-points technique, we have successfully simulated different types of sources. We have studied the two-dimensional source mechanism problems for the cases of SH-waves and elastic waves (both P and S), respectively. For the SH-wave case, two type of sources are considered: (a) a concentrated line source, and (b) a concentrated coupled line source. For the elastic wave case, three types of source are considered, viz., (a) a directional-force line source, (b) an omni-directional line source, (c) a single-couple-without-moment line source, (d) a single-couple-with-moment line source, and (e) a double-couple line source.

Consider a two-dimensional whole space elastic medium, with $v_p = 5,000$ m/sec, $v_s = 2,900$ m/sec, $\rho = 2.67$ gm/cm³. Figure 40 shows the 30×30 finite element mesh. Point $S(0,0)$ is the location of the applied source. Using this model, we have studied the following cases:

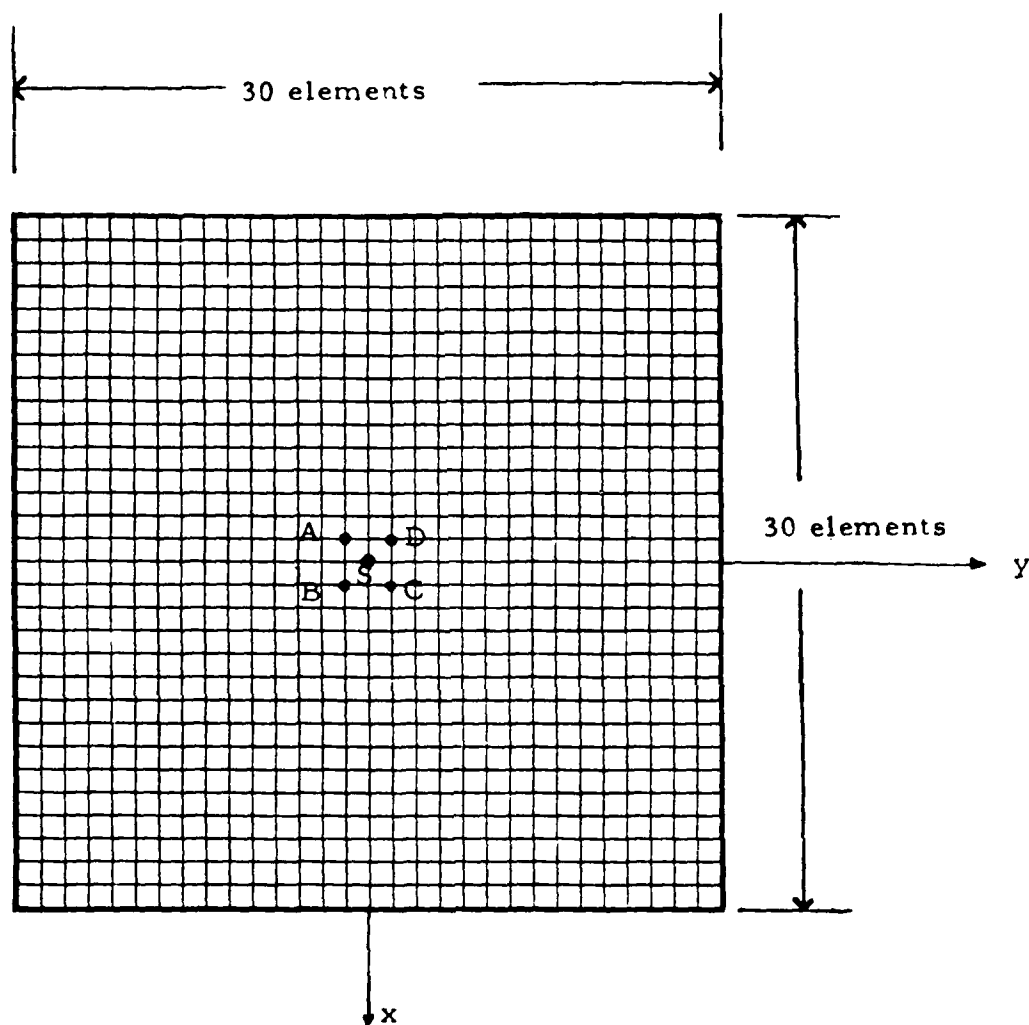


Figure 40. A 30x30 Finite Element Mesh of a Homogeneous Elastic Medium with $V_p = 5,000$ m/sec, $V_s = 2,900$ m/sec and $\rho = 2.67$ gm/cm³. ($\Delta x = \Delta y = 100$ m)

(1) ONE DEGREE OF FREEDOM SH-WAVE PROBLEM

(a) Concentrated Line Source

As we mentioned previously, this is the most natural way to apply an external source. At Point $S(0,0)$ in Figure 40, a forcing function, $F_1(t)$ as given in Figure 2, is applied. Figures 41-A to 41-H are the displacement fields at 0.1 sec intervals. The cylindrically spreading wave can be observed.

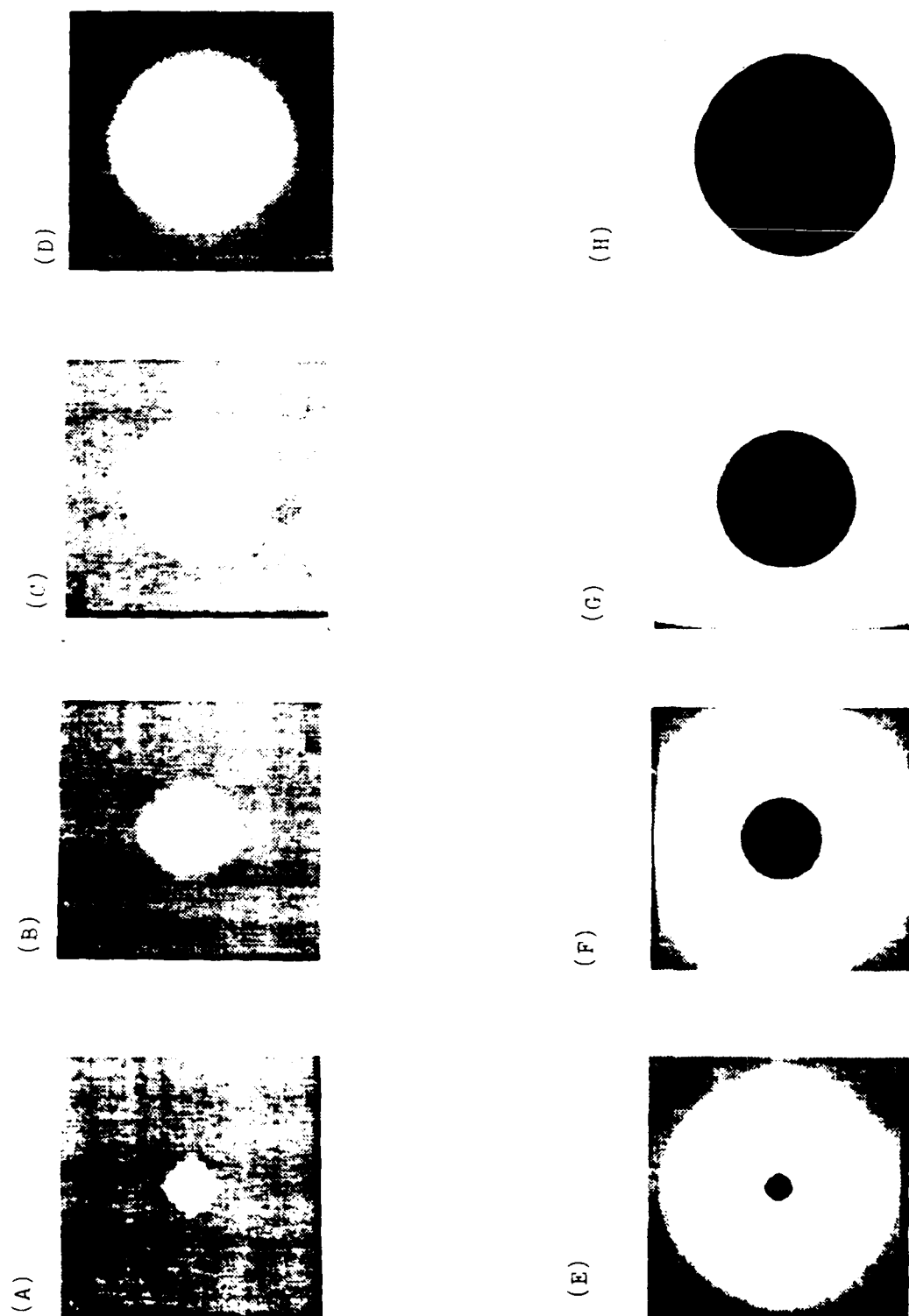


Figure 41. Snapshot View of Wave Pattern at 0.1 sec Interval After the Detonation of the Concentrated Line Source.

(ii) Concentrated Coupled Line Source

In order to simulate a coupled line source at point $S(0,0)$ of Figure 40, we let the points $S_1(0,+0)$, and $S_2(0,-0)$ occupy the same location as point S and apply the forcing function $F_1(t)$ to each individual nodal point but in the opposite directions as shown in Figure 42. In other words, the displacement fields are $w_1(0,+0,t)$ and $w_2(0,-0,t)$ at S_1 and S_2 , respectively. At the source points in Figure 42, dot means outward from the plane of the paper, cross means inward into the plane of the paper. Points A, B, C, and D are the nodal points surrounding point S (Figure 40). Figure 43-A to 43-H are the snapshots of the synthetic displacement field $w(x,y,t)$ at 0.1 sec intervals, showing the radiation pattern of a coupled source.

- Outward from the plane of the paper
- × Inward towards the plane of the paper

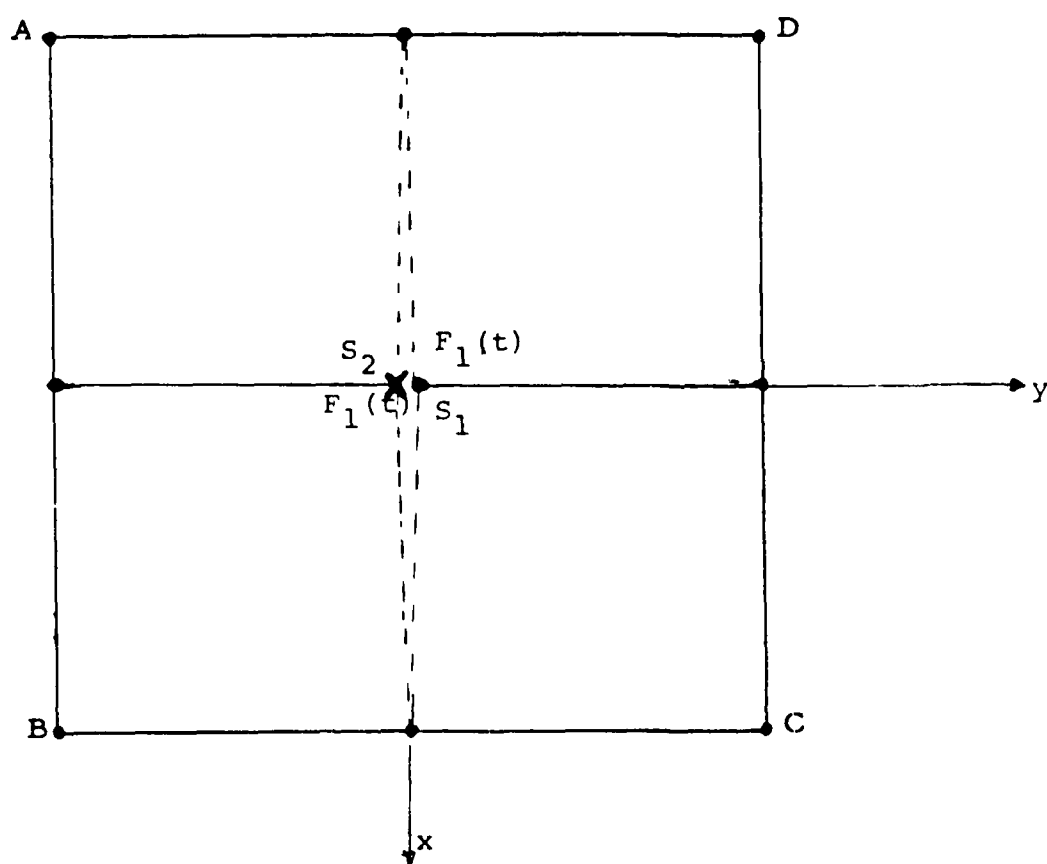


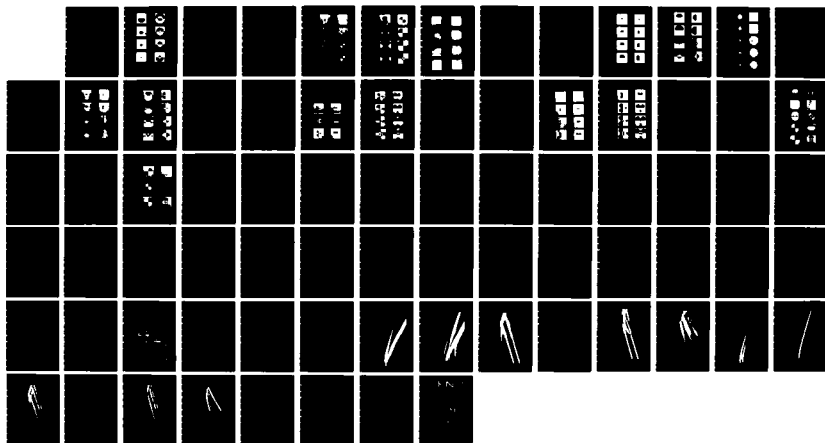
Figure 42. Concentrated Couple Source Mechanism
for SH-Wave Case.

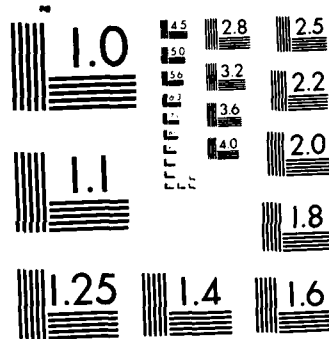
GROUND RESPONSE IN ALLUVIAL BASINS DUE TO SEISMIC
DISTURBANCES(U) COLUMBIA UNIV NEW YORK J T KUO ET AL
MAR 85 AFGL-TR-85-0062 F19628-81-K-0012

DISTURBANCES(U) COLUMBIA UNIV NEW YORK J T KUO ET AL
MAR 85 AFGL-TR-85-0062 F19628-81-K-0012

F/G 8/11

NL





MICROCOPY RESOLUTION TEST CHART
NATIONAL BUREAU OF STANDARDS 1963-A

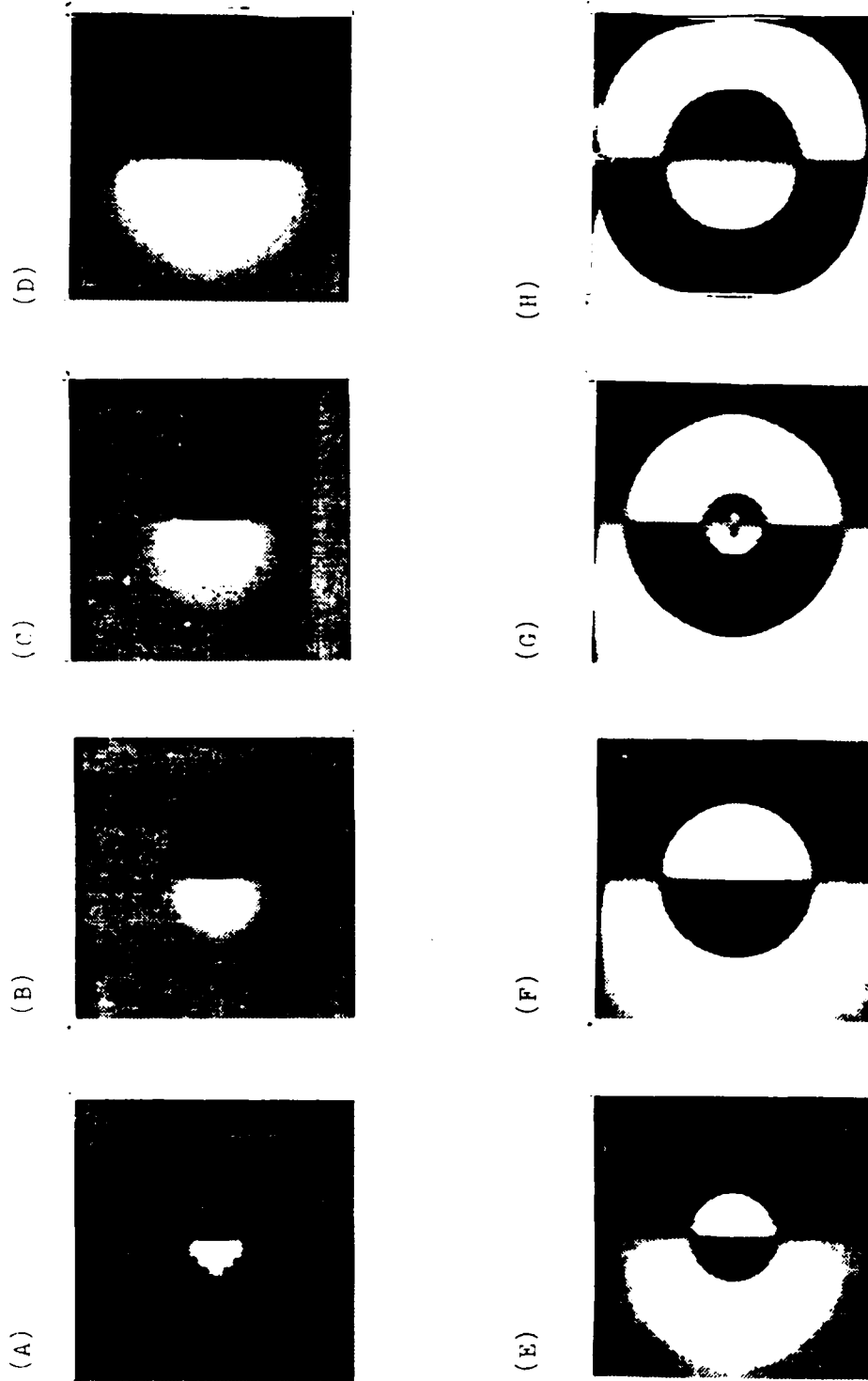


Figure 43. Snapshot View of Wave Pattern at 0.1 sec Interval After
The Detonation of the Concentrated Couple Source.

(2) TWO DEGREE OF FREEDOM ELASTIC WAVE PROBLEM

(a) Single-Directional Force Line Source

For the elastic wave case, one of the most common sources is the directional line source. In Figure 44, a vertical line source, $F_0(t)$ as given in Figure 18, is located at point S. Figures 45-A to 45-H are the snapshots of the displacement components u_x and u_y . Figures 46-A to 46-I are the snapshots of the absolute values of the displacement resultants. The time interval between snapshots is 0.0575 sec.

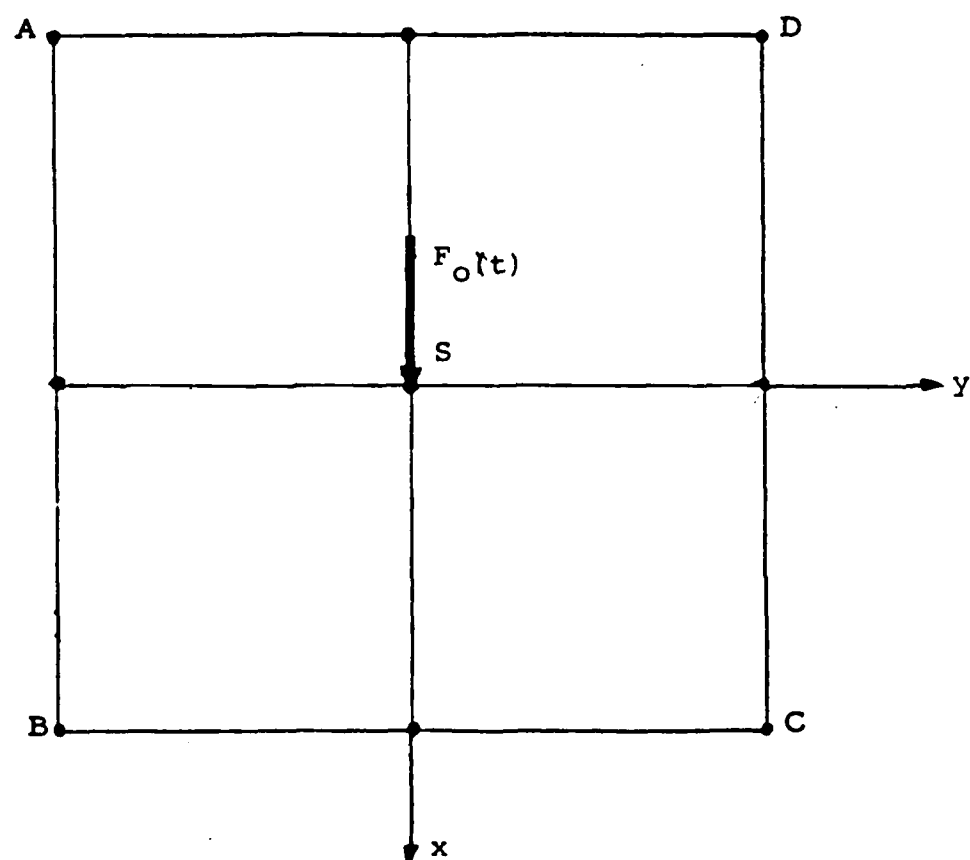


Figure 44. Directional Source for the Elastic Case.

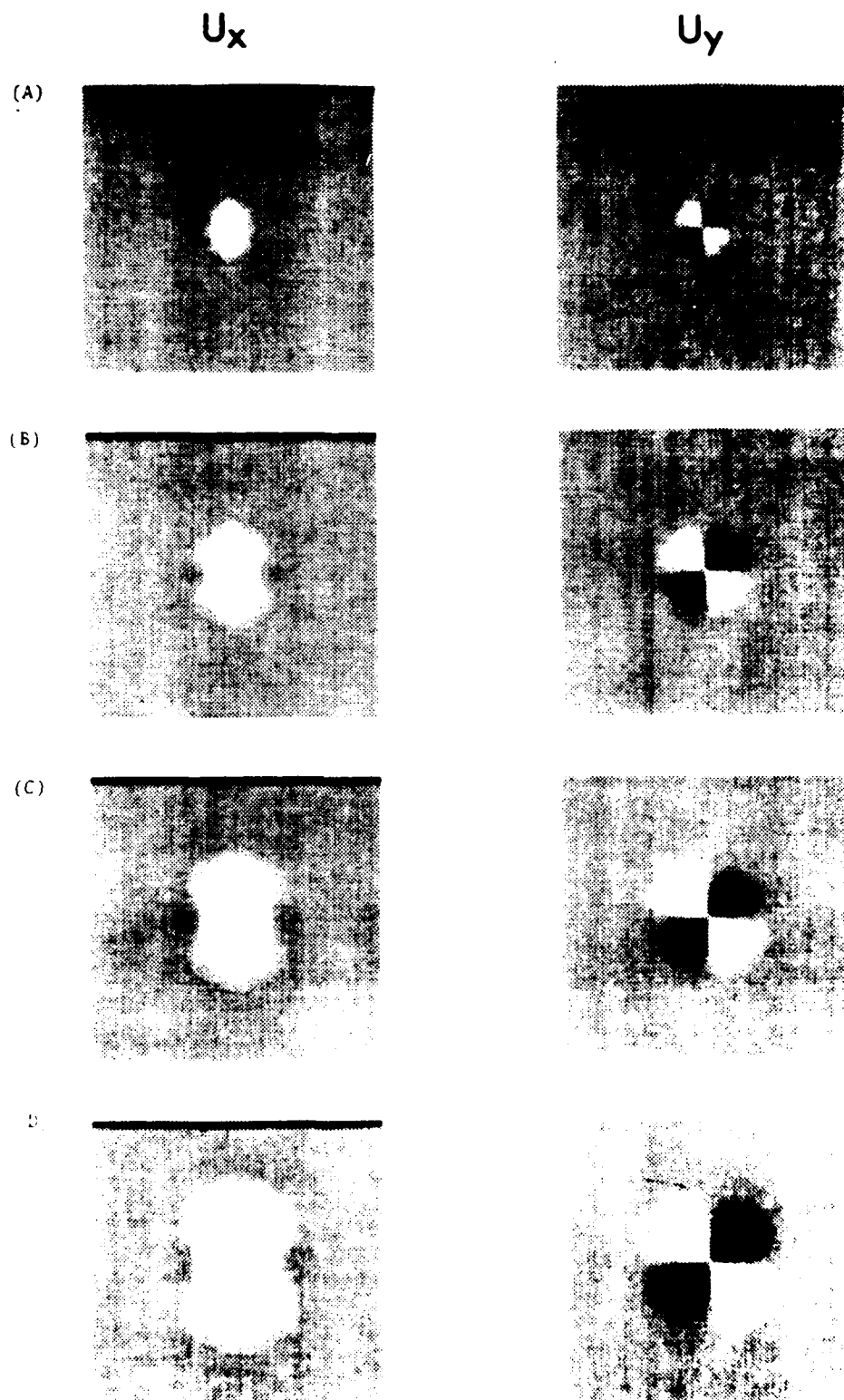


Figure 45. Snapshot View of Wave Pattern at 0.05T Interval After the Detonation of the Directional Line Source.

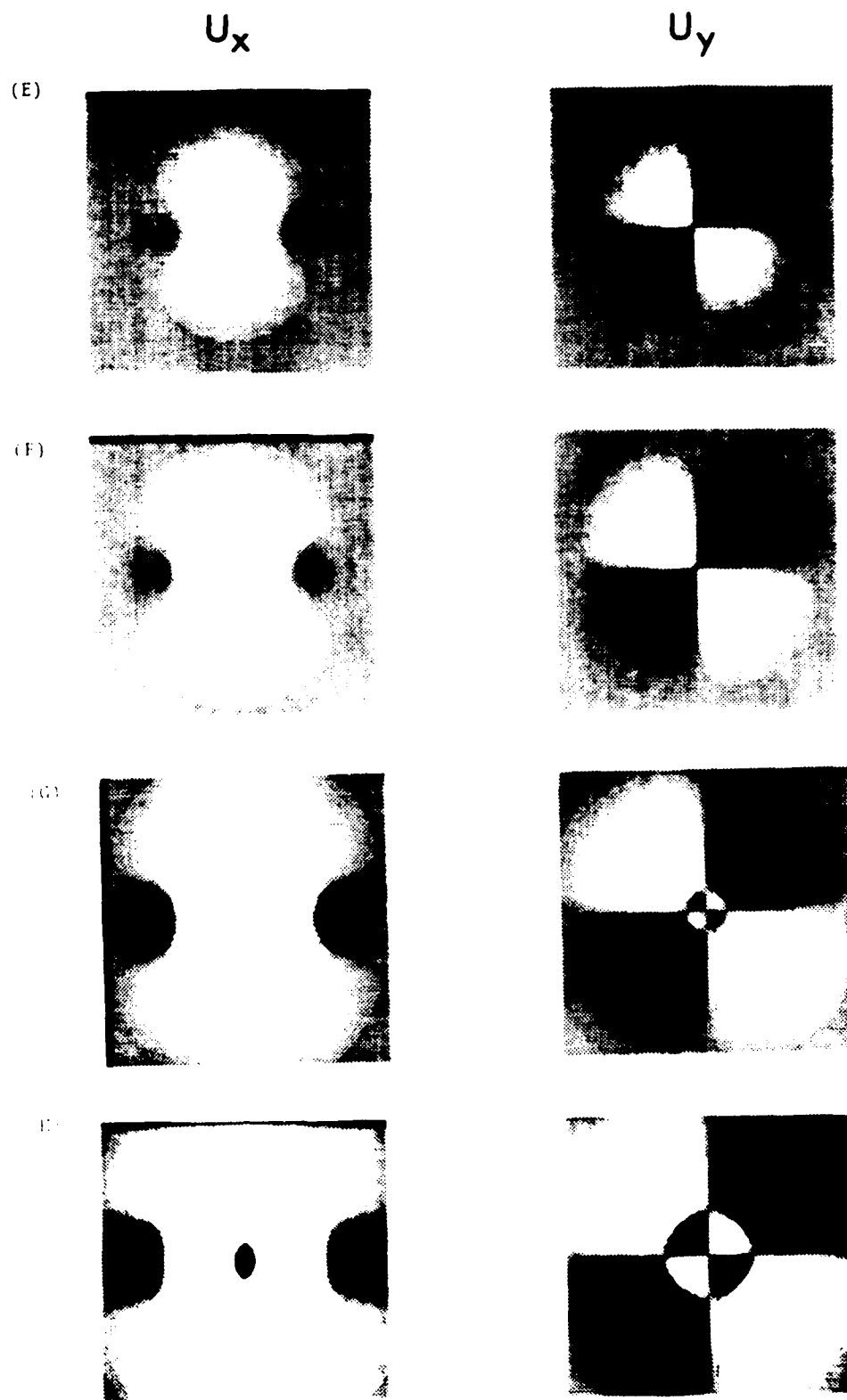


Figure 45. Snapshot View of the Wave pattern at 0.0375 sec Interval.
After the Detonation of the Directional Line Charge.

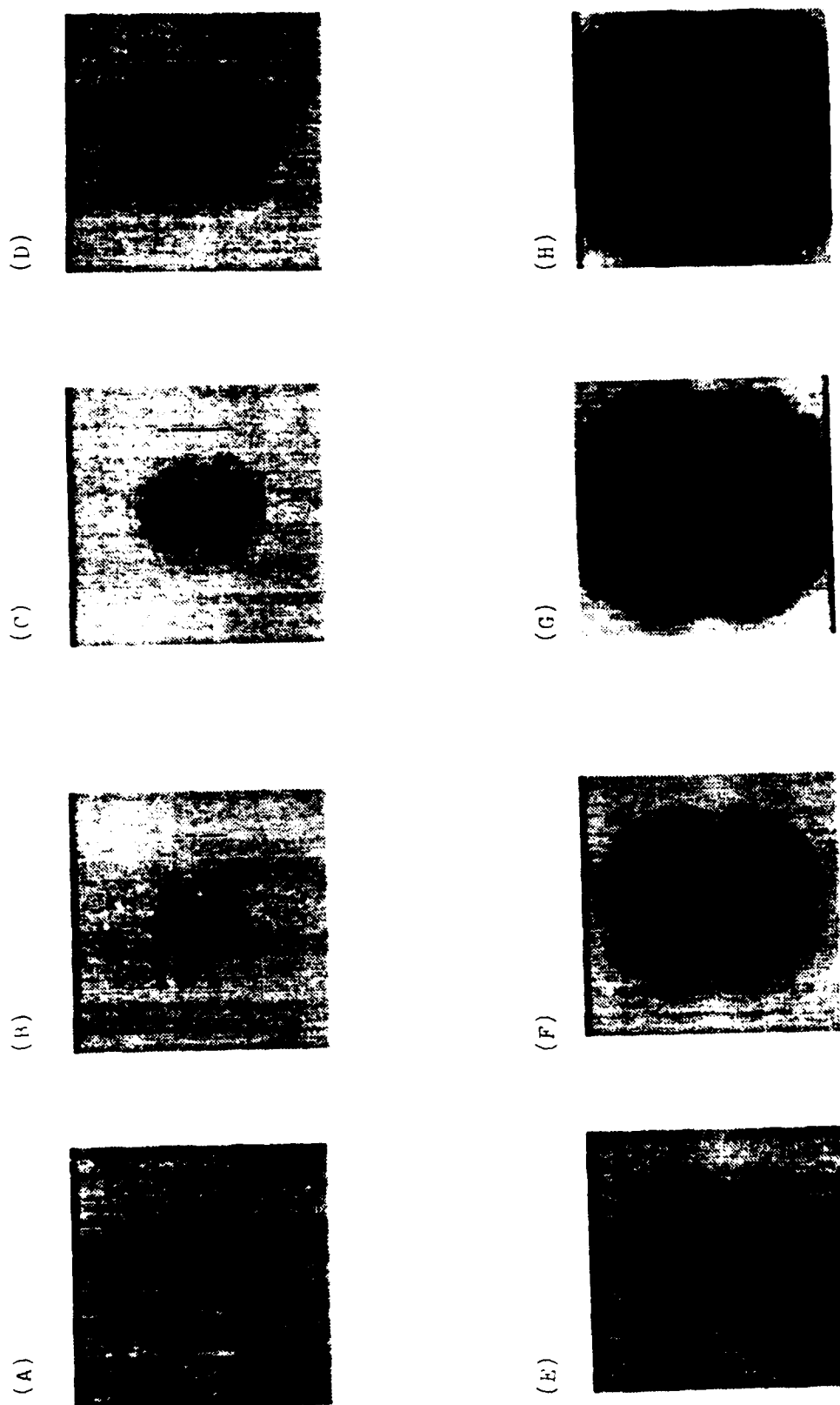


Figure 46. Snapshot View of Wave Pattern at 0.0574 sec Interval After the Initiation of the Pipisternal Line Source.

(b) Omni-Directional Force Line Source

In order to simulate an omni-directional line source at point $S(0,0)$ in Figure 40, we let the points $S_1(-0,+0)$, $S_2(+0,+0)$, $S_3(+0,-0)$, and $S_4(-0,-0)$ reside at the same location as point S and apply a forcing function, $F_0(t)$, to each individual point in the manner shown in Figure 47. Figures 48-A to 48-H are the snapshots of the displacement components u_x and u_y . The time interval between snapshots is also 0.0575 sec. The cylindrically spreading radiation patterns of the displacement magnitude can be observed in Figure 49-A to 49-J.

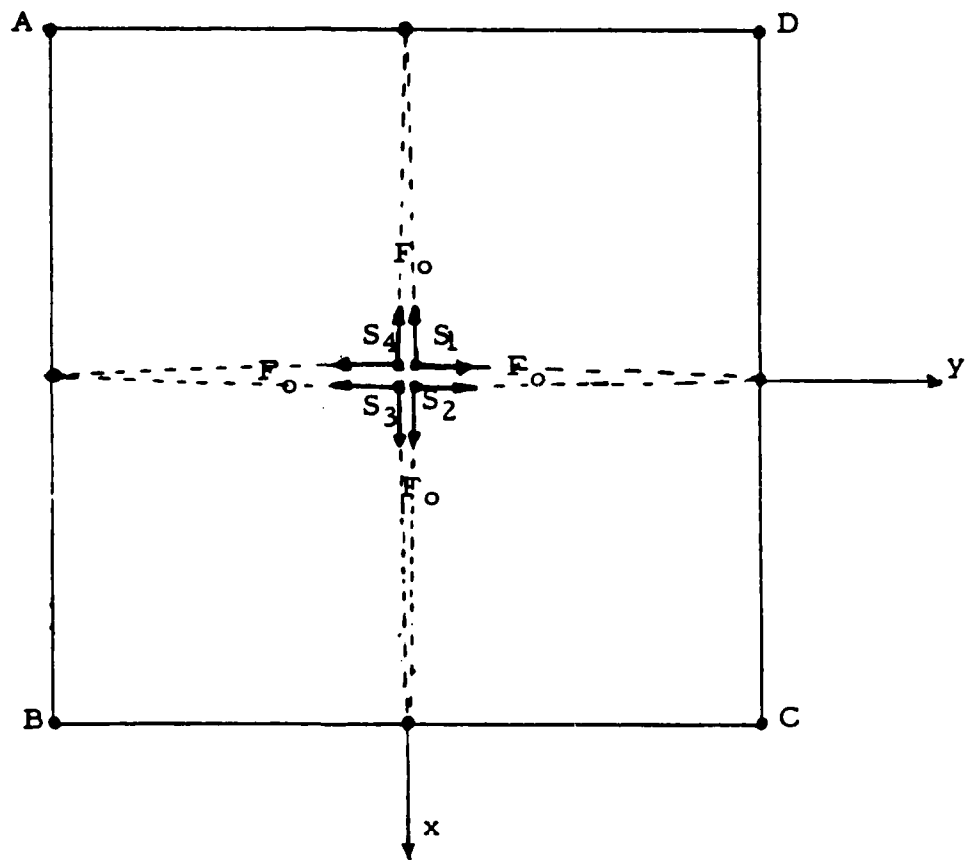


Figure 47. Omni-directional Line Source Mechanism
for Elastic Case.

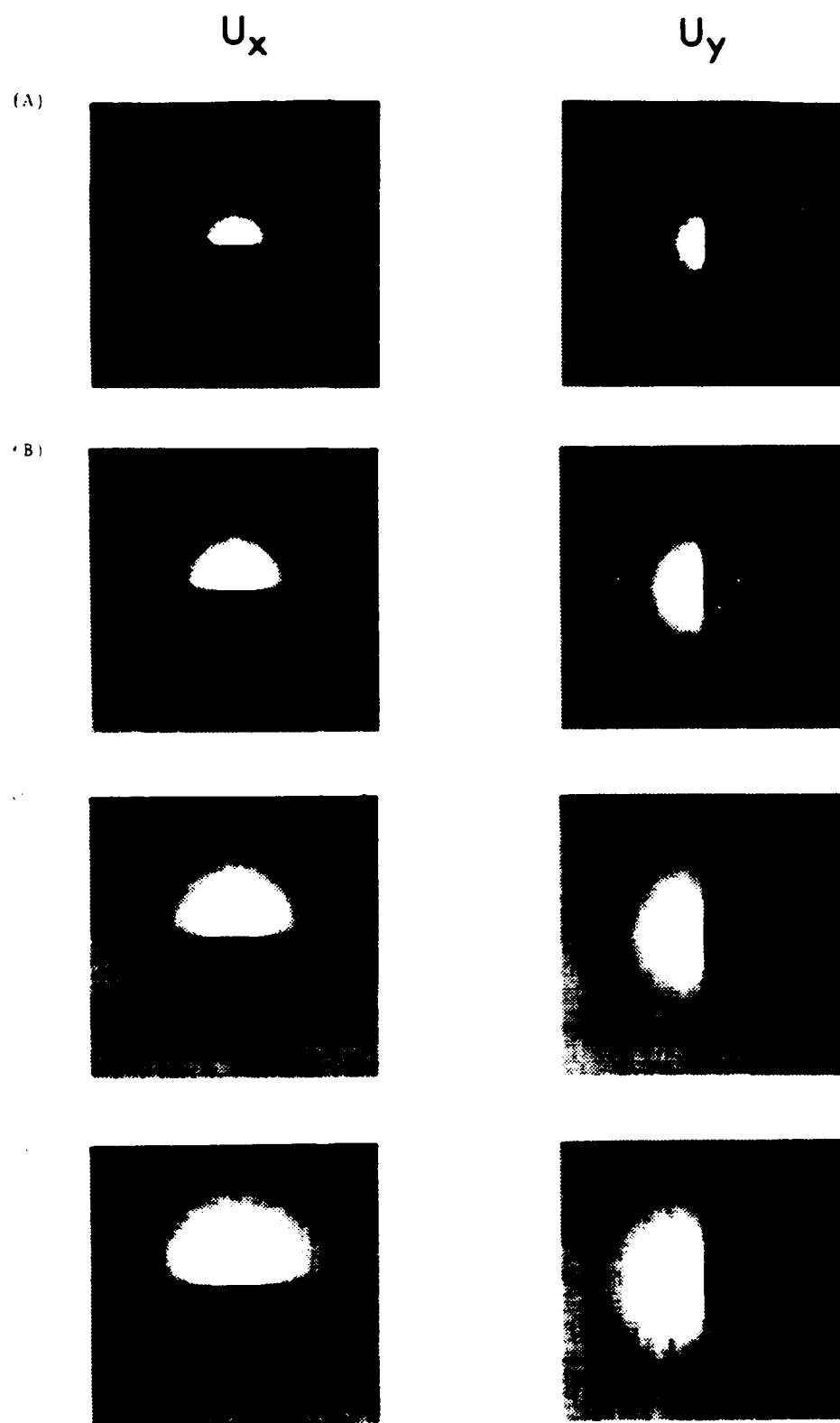


Figure 48. Laser Pattern at 100% Intensity
 (A) Direct, (B) Indirect, (C) Direct, (D) Indirect

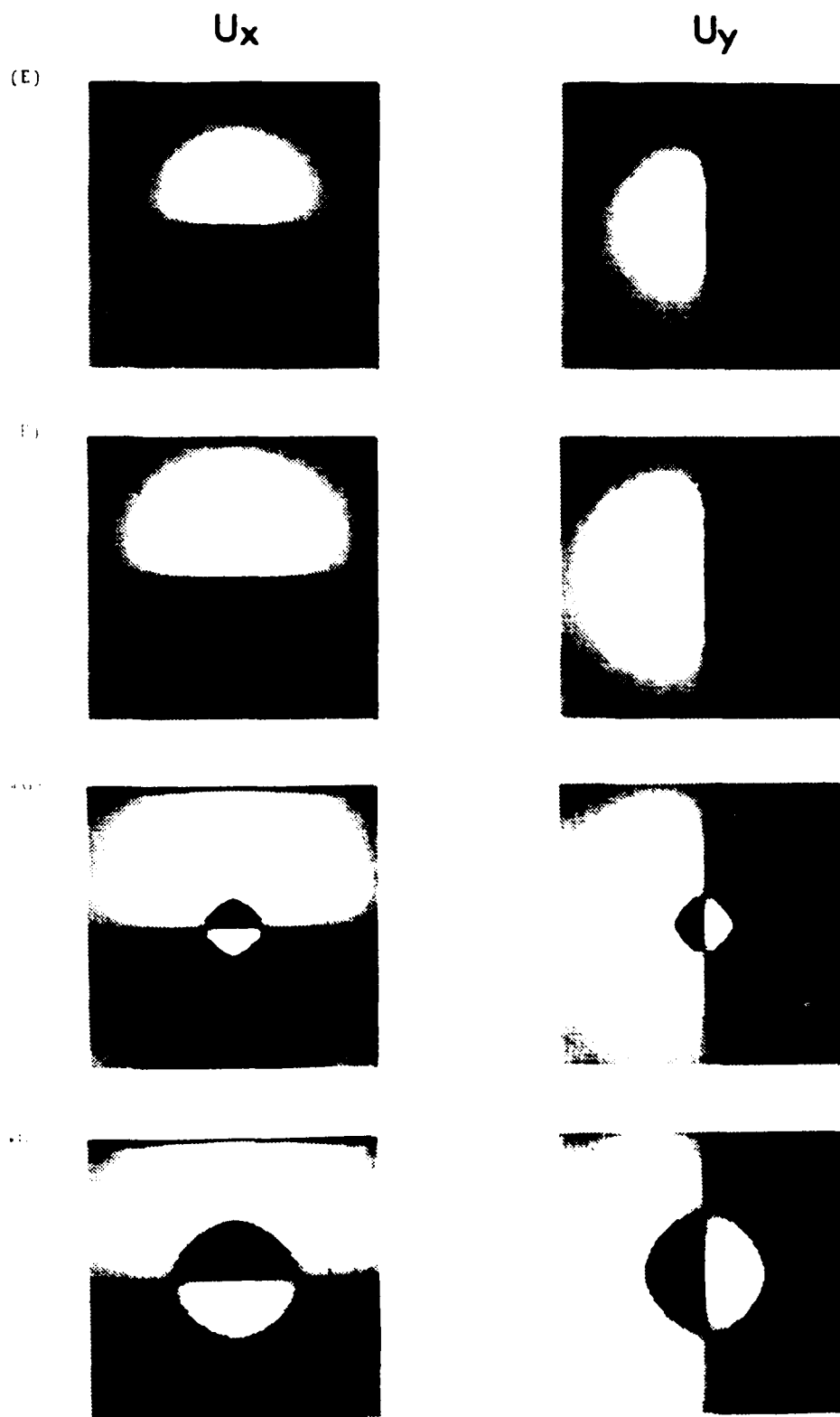


Figure 48. Comparison of the image pattern at 0.575 sec. Interval after the initiation of the two-dimensional flow.

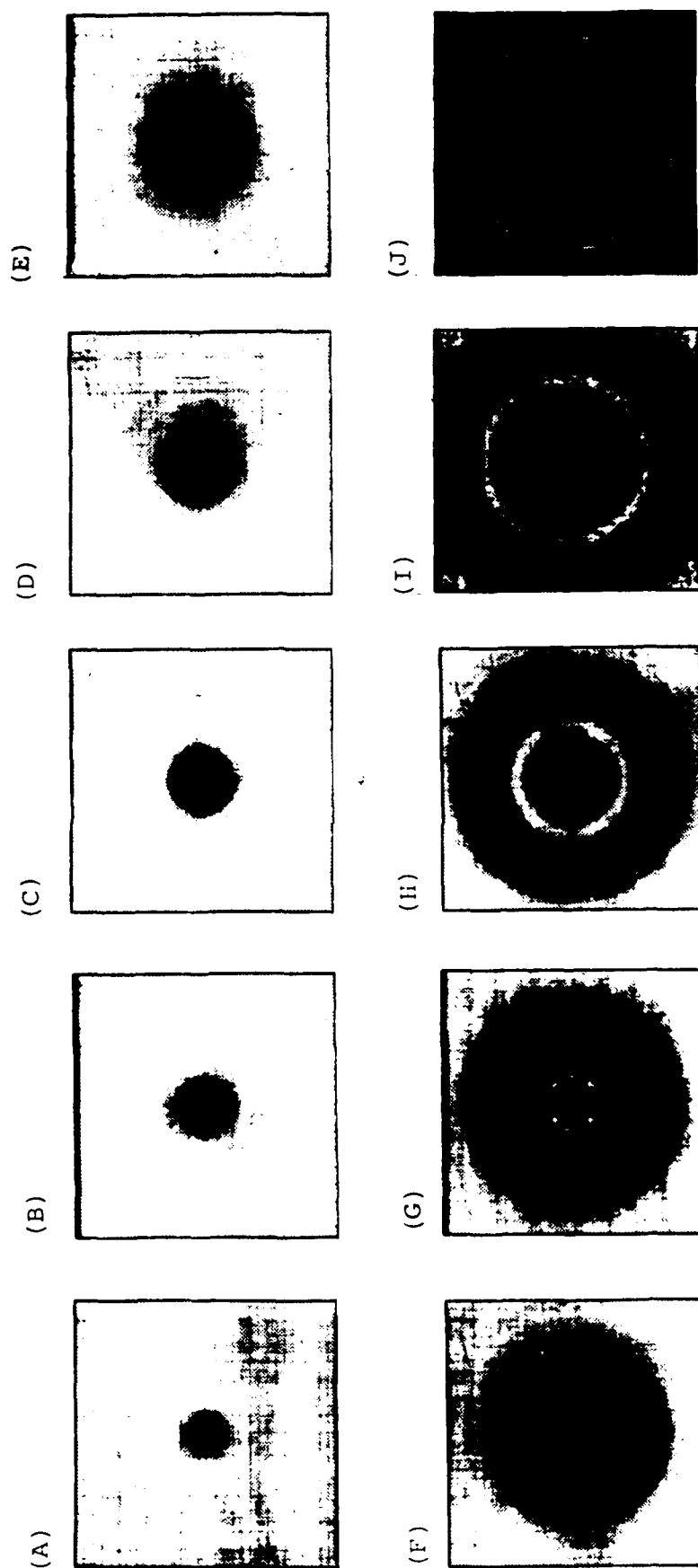


Figure 49. Snapshot View of Wave Pattern at 0.0575 sec Interval After the Detonation of the Concentrated Omni-directional Source.

(c) Couple-Without-Moment Line Source

Figure 50 shows the mechanism of a couple-without-moment line source for the elastic wave case. Points $S_1(+0,0)$ and $S_2(-0,0)$ occupy the same location and are subjected to two forcing functions, $F_0(t)$, having the same magnitude but in the opposite directions, creating a couple without moment. The radiation patterns of the displacement components u_x and u_y are given in Figures 51-A to 51-B.

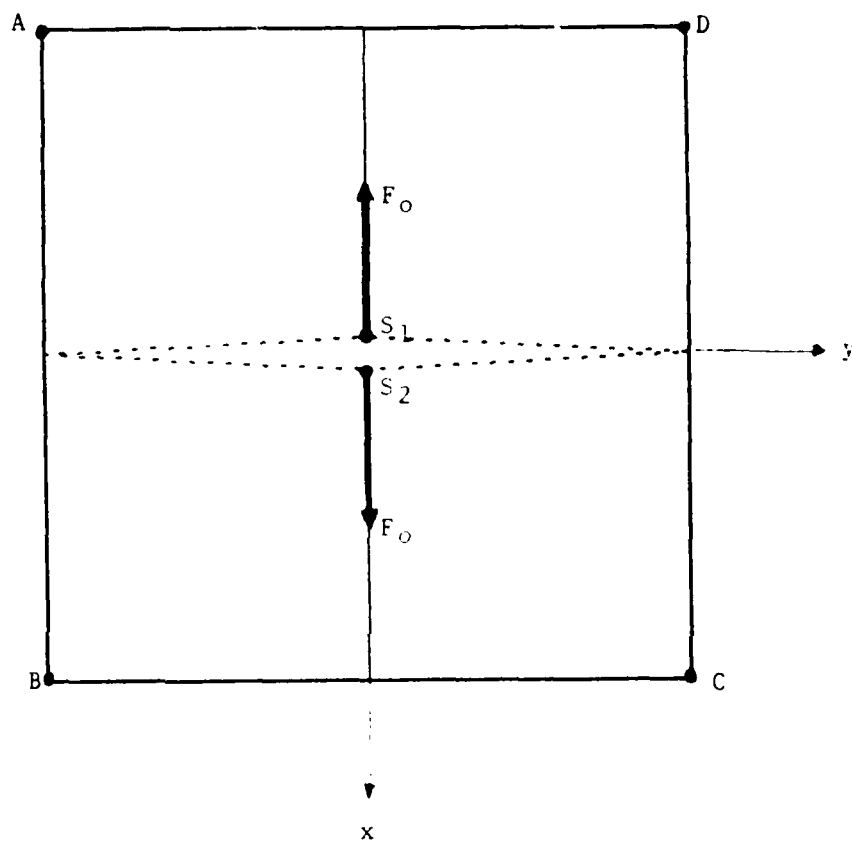


Figure 50. Single Couple-Without-Moment Source Mechanism.

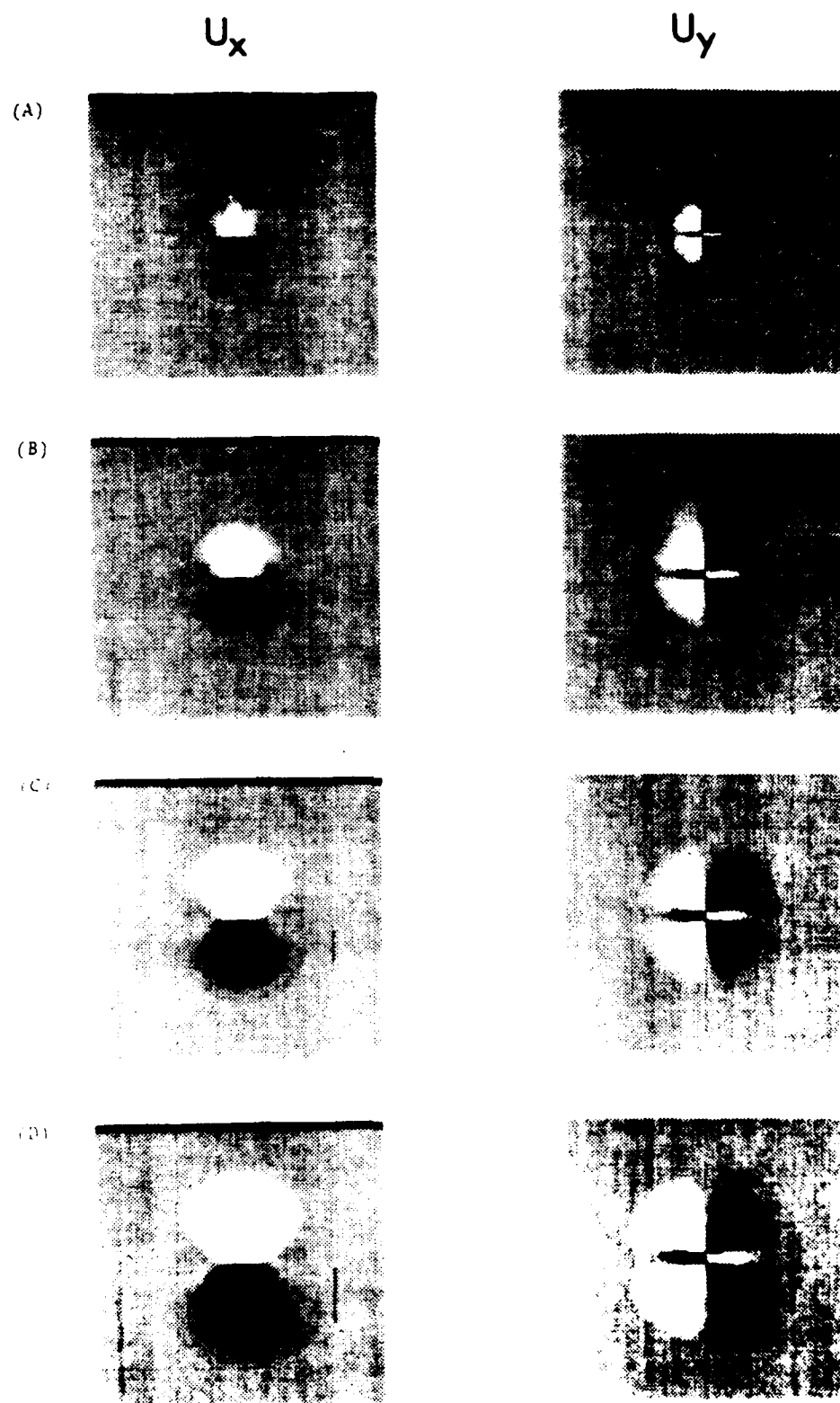


Figure 51. Snapshot View of Wave Pattern at 0.575 sec Interval After the Detonation of the Couple-without Moment Source.

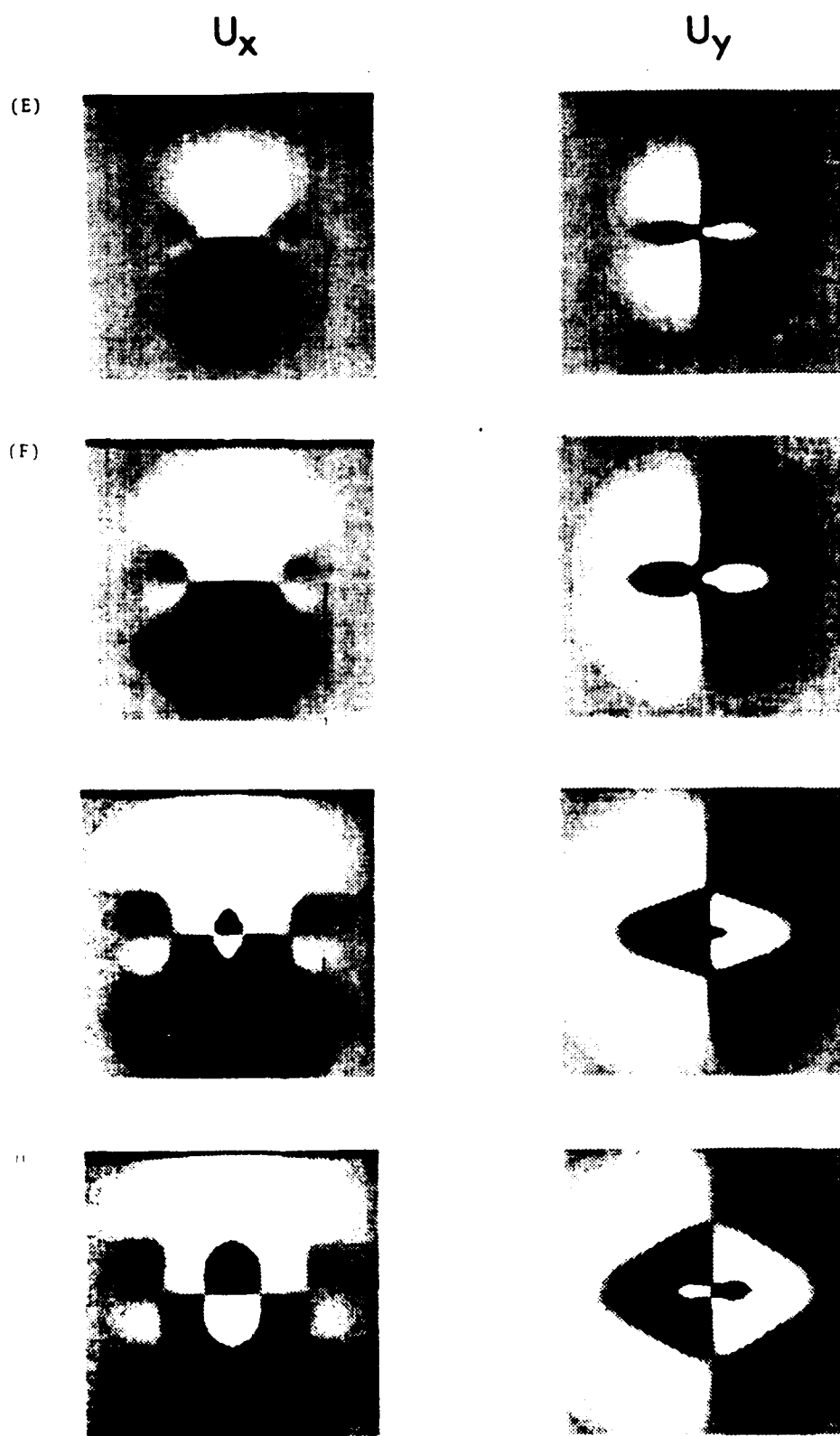


Figure 51. Snapshot View of Wave Pattern at 0.0375 sec Interval after the Detonation of the Couple-without-Moment Source.

(d) Couple-With-Moment Line Source

Figure 52 shows the mechanism of a couple-with-moment line source for the elastic wave case. Points $S_1(+0,0)$ and $S_2(-0,0)$ occupy the same location and are subjected to a moment forcing function $F_0(t)$, with the same magnitude but in the opposite directions. The radiation patterns of the displacement components u_x and u_y are given in Figures 53-A to 53-B.

•

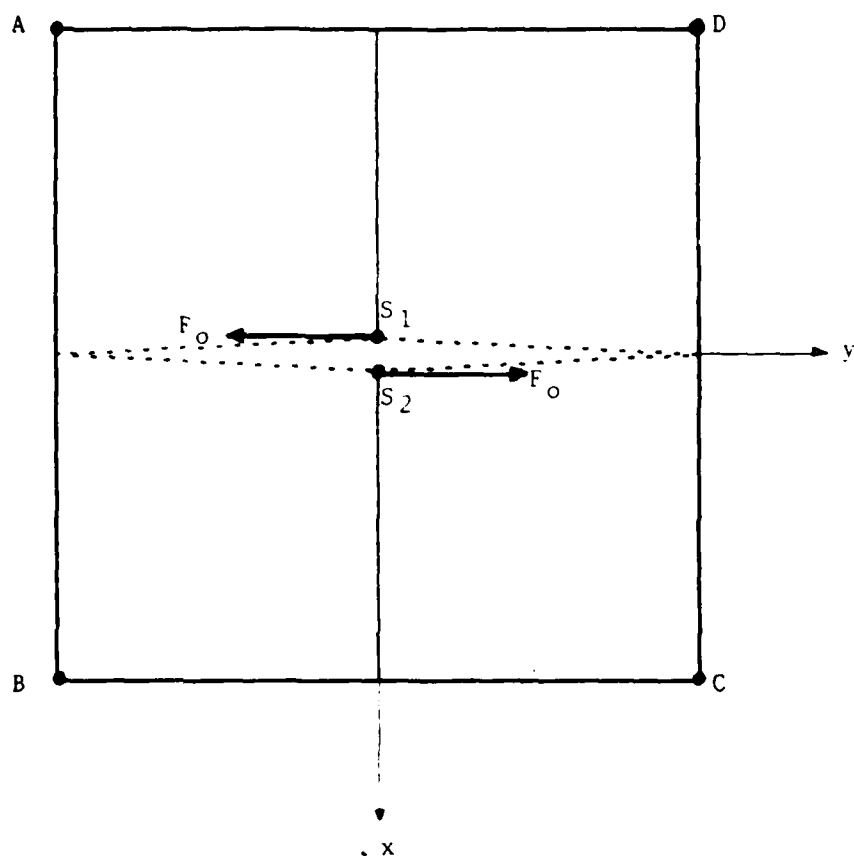


Figure 52. Single-Couple-With-Moment Source Mechanism.

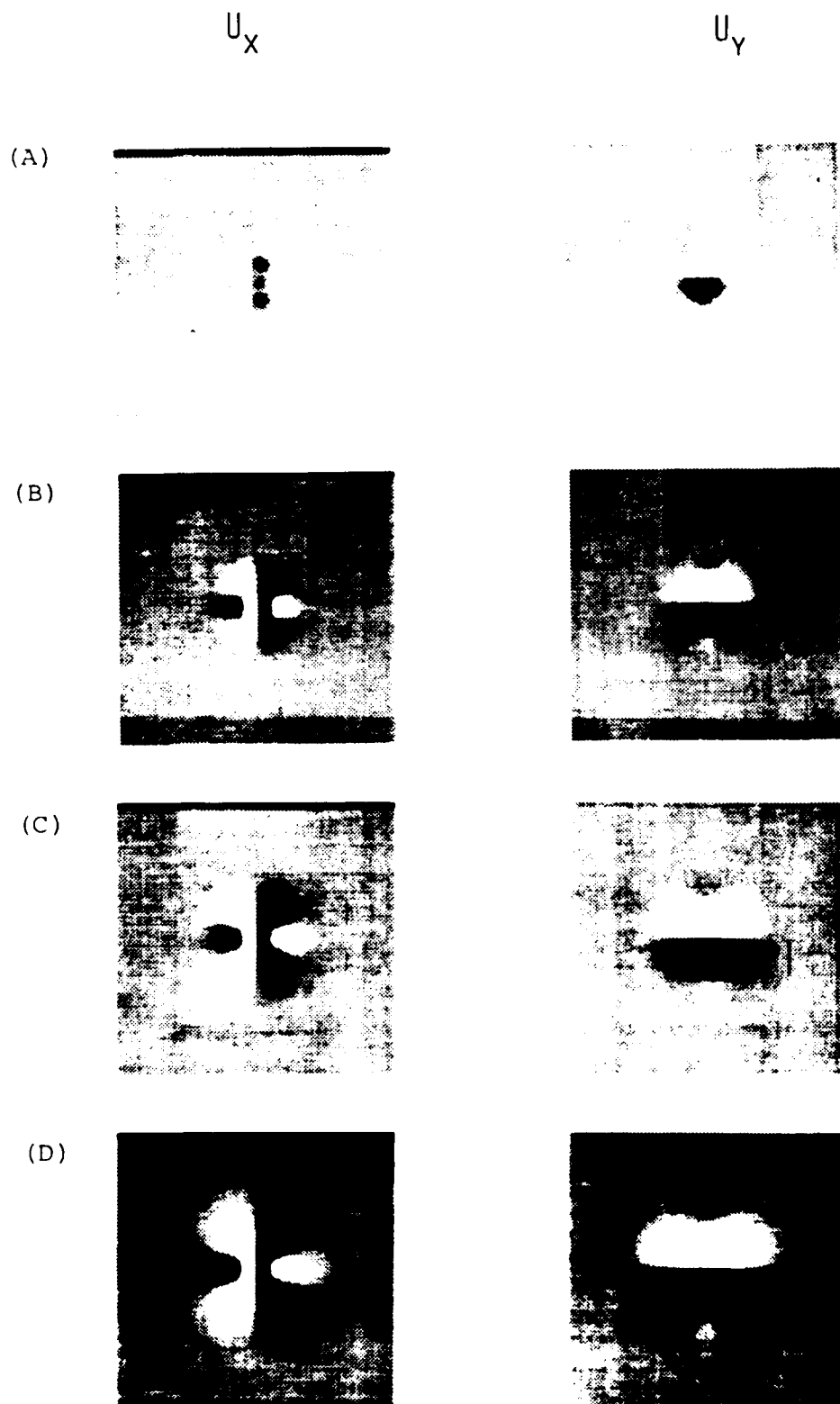
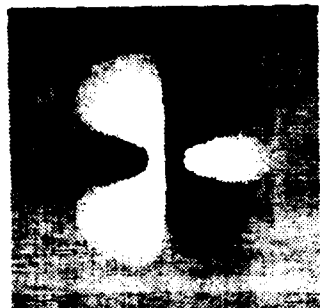


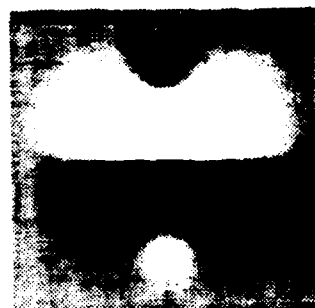
Figure 53. Snapshot View of Wave Pattern at 0.0575 sec. Interval,
after the Detonation of the Couple-with-Moment Source.

U_x U_y

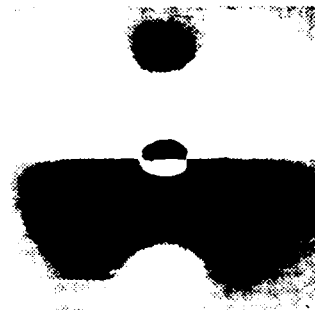
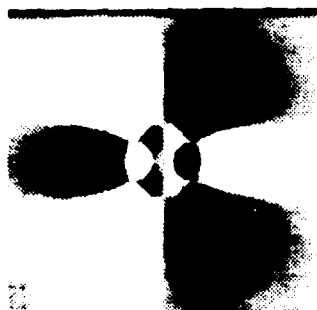
(E)



(F)



(G)



(H)

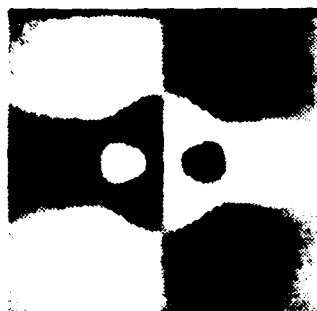


Figure 53. Snapshot View of Wave Pattern at 0.0575 sec Interval
after the Detonation of the Couple-with-Moment Source.

(d) Double-Couple Force Line Source

In order to simulate a double-couple force line source at point $S(0,0)$ in Figure 40, we let the points $S_1(-0,+0)$, $S_2(+0,+0)$, $S_3(+0,-0)$, and $S_4(-0,-0)$ at the same location as point S and apply a forcing function $F_0(t)$ to each individual point in a manner shown in Figure 54. Figures 55-A to 55-H are the snapshots of the displacement components u_x and u_y . The time interval between snapshots is also 0.0575 sec.

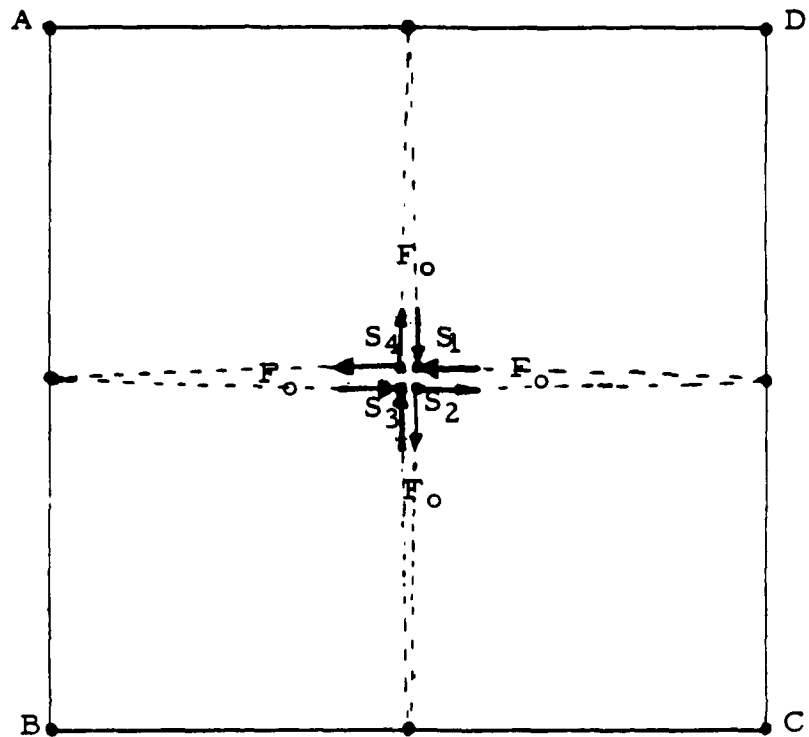


Figure 54. Double-Couple Force Source Mechanism.

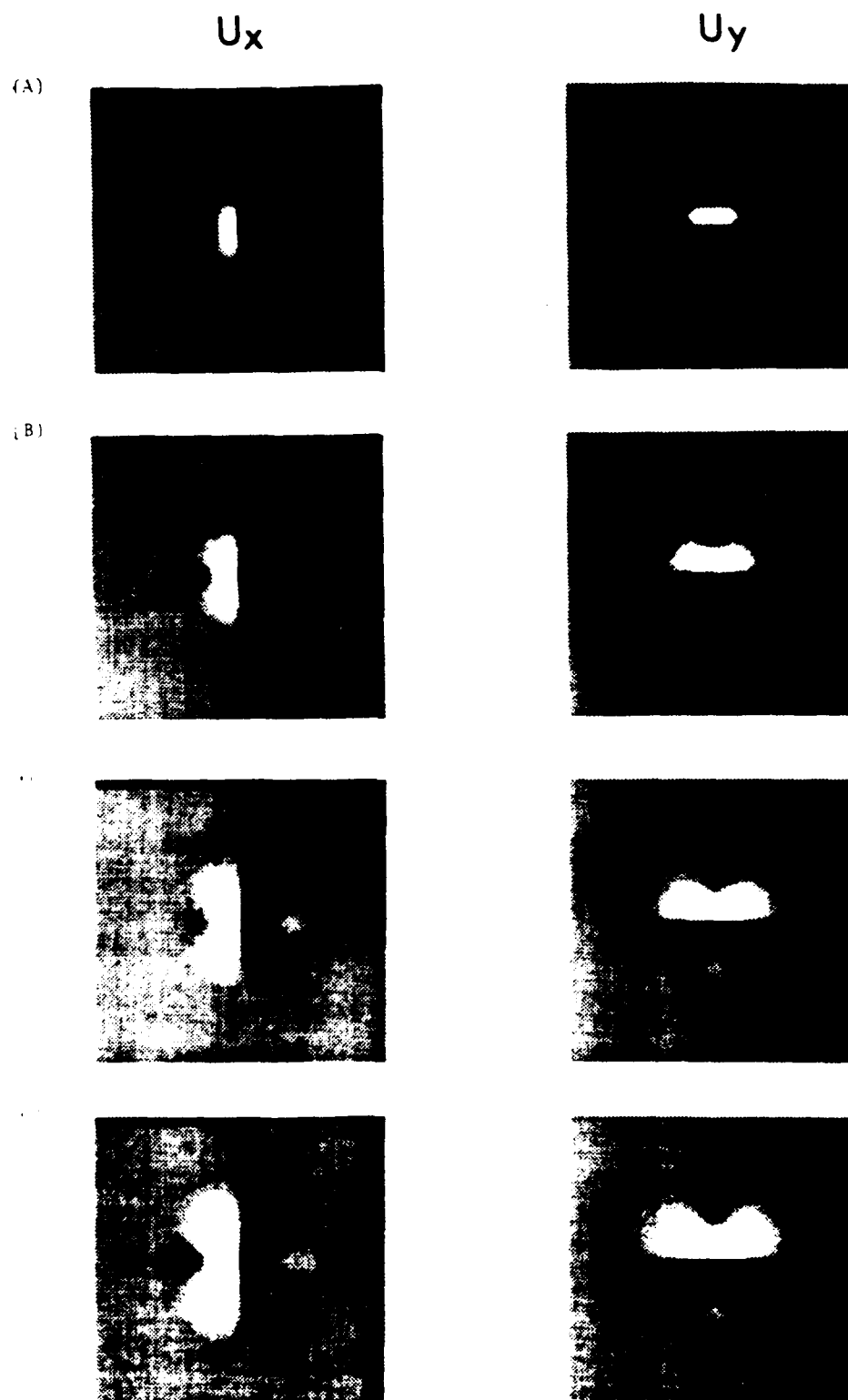


Figure 55. Snapshots of Wave Pattern at $t = 0.75$ and 1.0 and
After the determination of the Double-Couple M_{DC} (in μ).

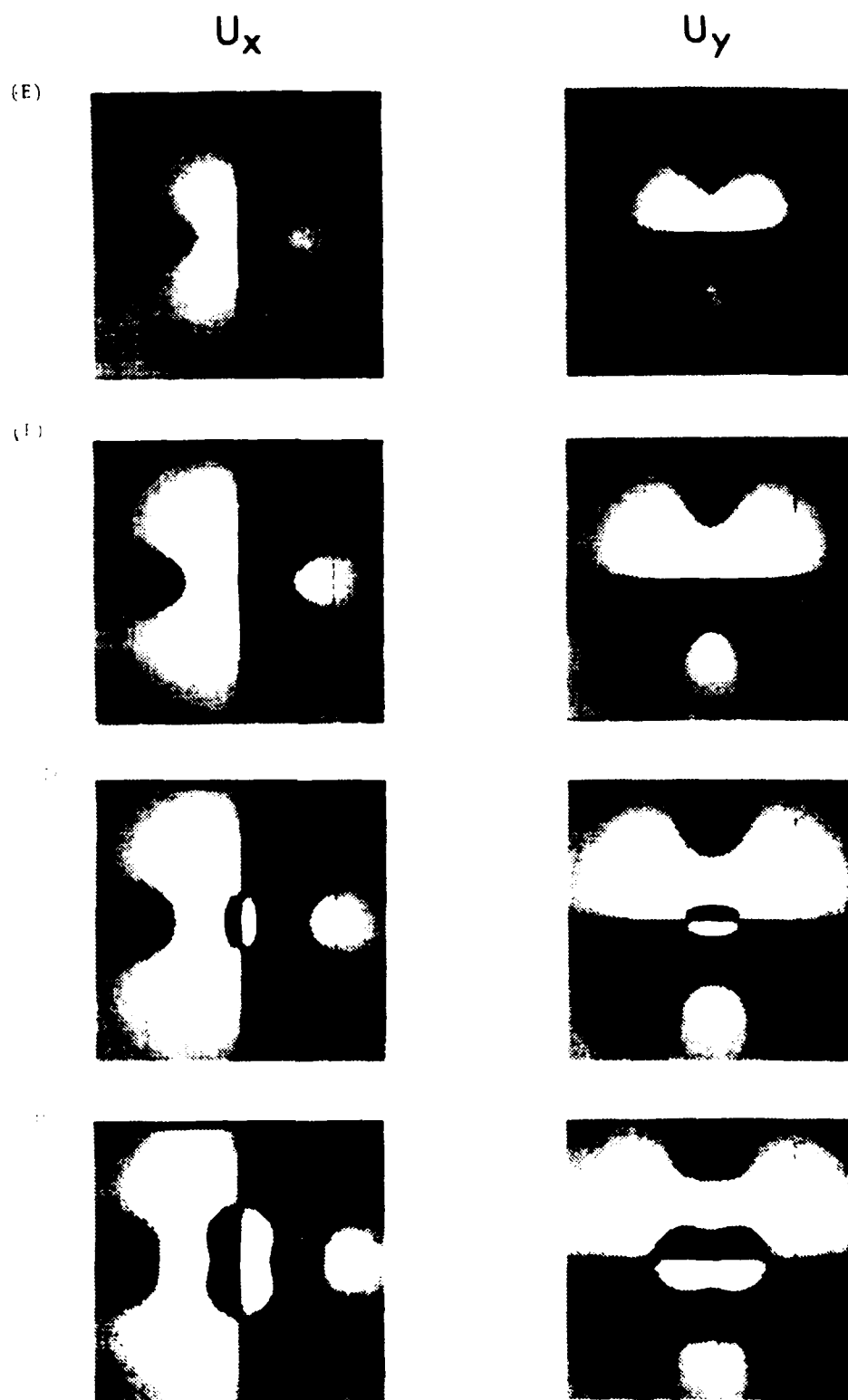
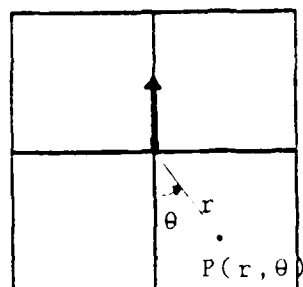


Figure 55. Snapshot View of Wave Pattern at 0.073 sec. Interval After the Activation of the Double-Couple Source.

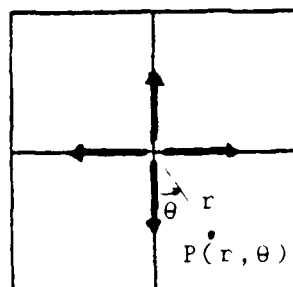
(3) REMARKS ON THE FINITE ELEMENT SOLUTIONS

(a) In the preceding seven cases, the non-reflecting boundaries techniques are used on all the four boundaries. Without using the non-reflecting boundaries, undesired reflections would appear at the 15th time step after the detonation of the source, or 0.3 seconds for the SH-wave cases and 0.1725 seconds for the models of the elastic wave cases.

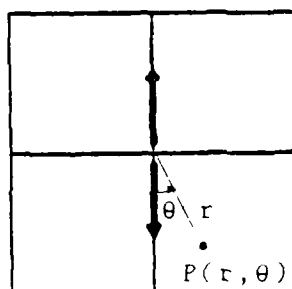
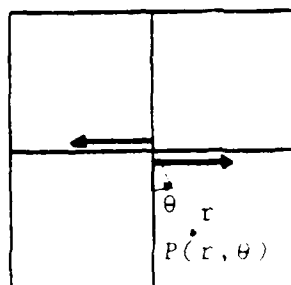
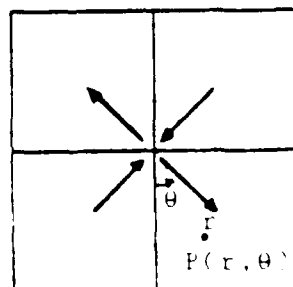
(b) All the snapshots of the displacement field for the preceding five elastic solid cases are presented in a rectangular coordinate system. It may provide better physical understanding if we transform the results into the polar system (r, θ) . Figures 56 show the radiation patterns for the radial displacement u_r and the transverse displacement u_t due to the five different types of source (Figure 56-A). The snapshots shown in Figure 56-B are the displacement fields at the 30th time step, 0.345 seconds after the detonation of the source. These results qualitatively agree with the classic analytical solutions of the three-dimensional source mechanism given by Honda (1952).



(A) SINGLE DIRECTIONAL FORCE.



(B) OMNI-DIRECTIONAL FORCE.

(C) SINGLE-COUPLE FORCE
WITHOUT MOMENT.(D) SINGLE-COUPLE FORCE
WITH MOMENT.

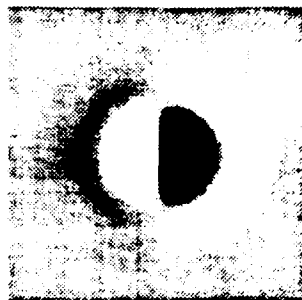
(E) DOUBLE-COUPLE FORCE.

FIGURE 56-A. FIVE DIFFERENT TYPES OF SOURCE.

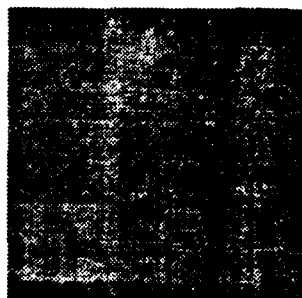
U_R U_T

117

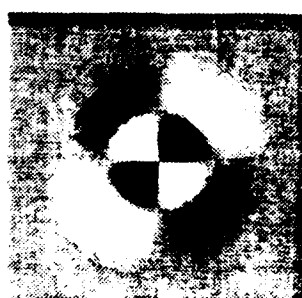
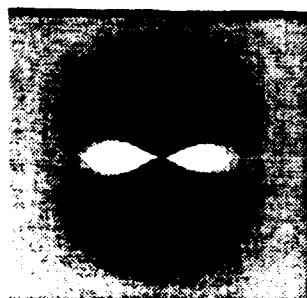
(A)



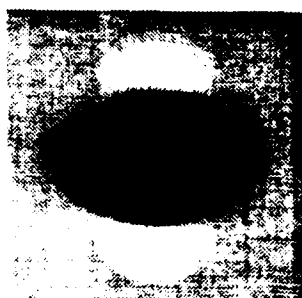
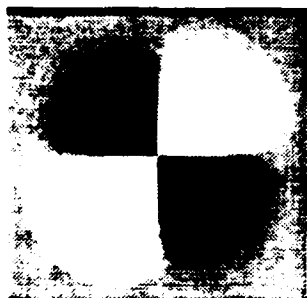
(B)



(C)



(D)



(E)

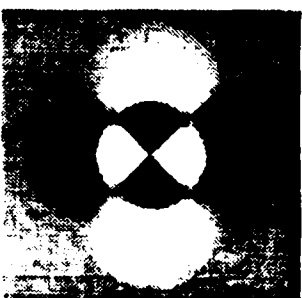
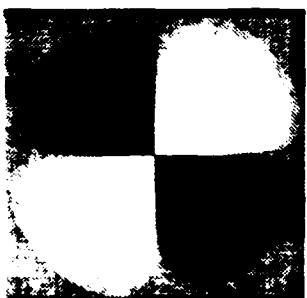
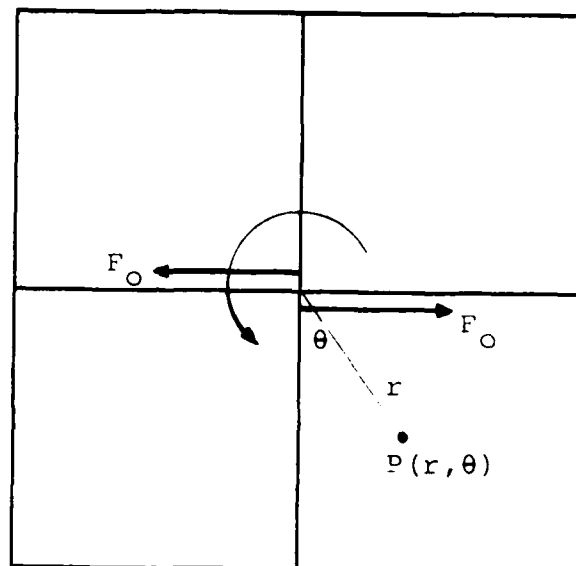


Figure 56-1. Calibration Patterns of the Uses in Figure 56-A.

(c) Honda (1952) showed that the combination of two coplanar-couple forces with moment in the opposite rotational direction (Figures 57-A and 57-B) is equivalent to that of two coplanar-couple forces without moment. (or a combination of compression and tension, which are 90 degrees out of phase (Figure 55-C). In the finite element results, Figures 58-A and 58-B are the snapshots of the radial and transverse components of the displacement field, u_r and u_t , associated with the cases of Figure 57-A and 57-B. Figure 58-C is the combined results of 58-A and 58-B. These combined results are exactly the same as the displacement field due to the case of Figure 55-C. The snapshots are taken at the 25th time step, 0.2875 seconds.

(A)



(B)

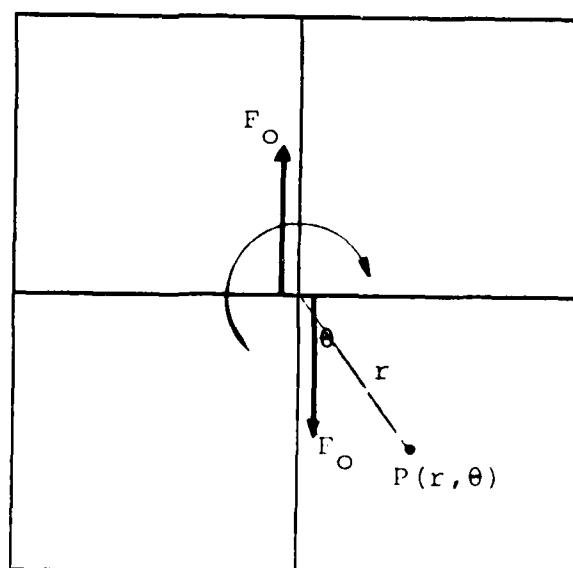


Figure 57. Two Types of Single-Couple-Forces With Moment.

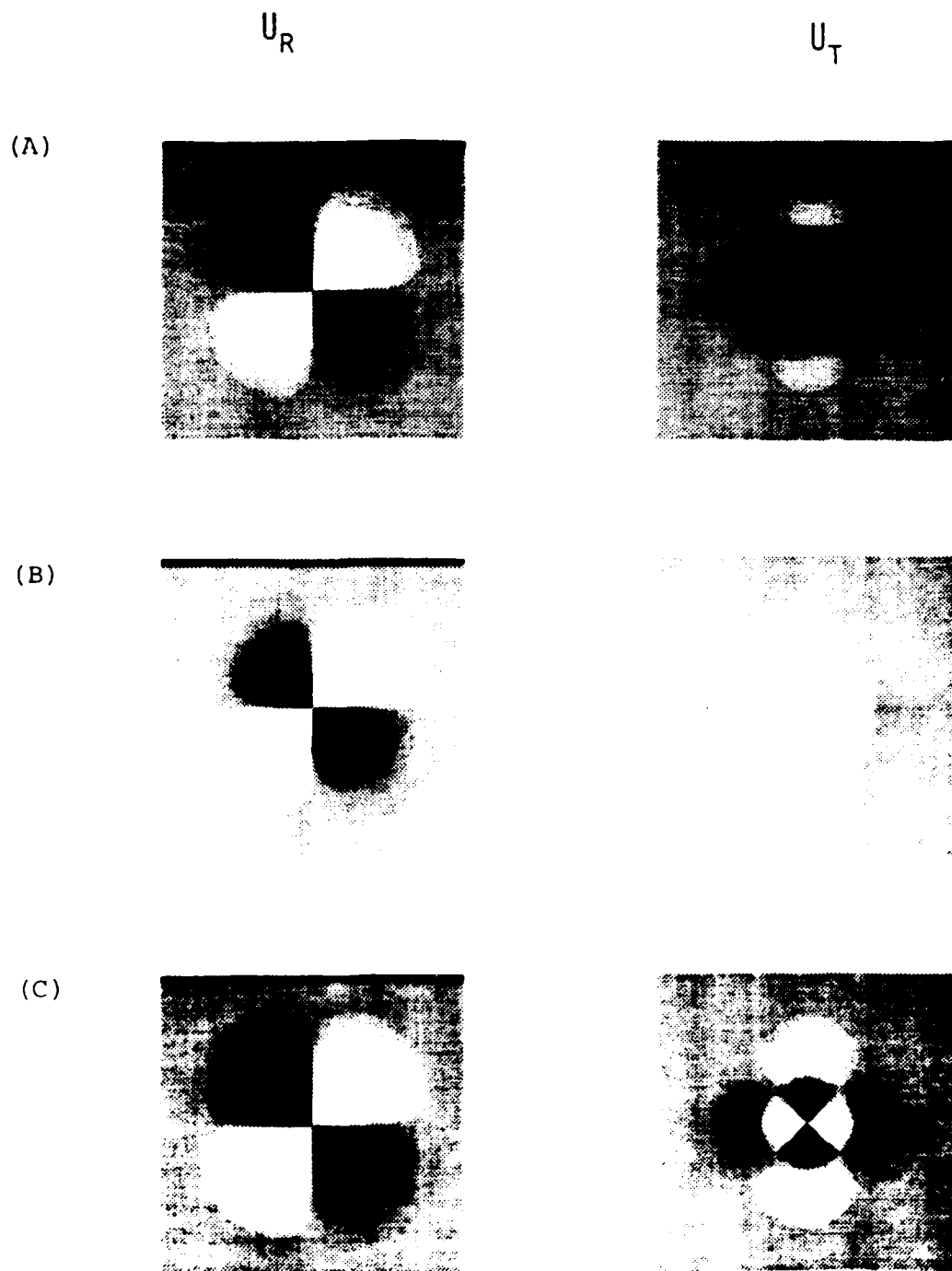


Figure 58. Radiation Patterns of the Cases in Figure 57.

(4) DEMONSTRATION OF THE WAVEFORMS STRONGLY DEPENDS ON THE NATURE OF SOURCE

It is well known that the elastic response due to a spherical pressure pulse is dominated by P waves, while the elastic response due to a directional point force is rich in shear and Rayleigh waves in the near field. In order to demonstrate this difference in waveforms due to two different types of source, an example of an anticlinal model is given in Appendix A (A part of the work in Appendix A is supported by PROJECT MIDAS).

V. THE TWO-DIMENSIONAL FINITE ELEMENT COMPUTER PROGRAM FOR ELASTODYNAMIC PROBLEMS (THE USER'S GUIDE)

The program described here is specifically coded for solving a class of elastodynamic transient problems in elastic wave scattering and diffraction for the two-dimensional case. This element-oriented finite element code, designated as ALFE2.A, has been adapted to the VAX 11/780 computer at AFGL last October (1984).

In the computer code ALFE2.A, we have addressed our particular attention toward the areas of: (a) practical difficulties of using enormously large in-core storage without increasing I/O time, and (b) solving sparse matrix without calculating zero-matrix elements to save computing time. We succeeded in overcoming these serious difficulties to a certain degree.

The present computer code ALFE2.A is written in standard FORTRAN IV language and has been executed successfully on the PRIME 750 computer.

(1) FORMULATION

The general procedure for using the finite element method in solving elastodynamic problems in continuum mechanics includes idealization of the problem, finite element space discretization, formulation of the set of simultaneous equations to be solved, and time integration. We summarize the ALFE2.A code as follows:

(a) Basic Formulation

Based on the principle of virtual work, the equations of motion for elastodynamics are:

$$[M] \{\ddot{u}\} + [K] \{u\} = \{f(t)\}$$

where $\{u\}$, $\{\ddot{u}\}$ are the displacement and acceleration vectors of the finite element assemblage, and $[M]$ is the assembled mass matrix, $[K]$ is the assembled stiffness matrix, and $\{f(t)\}$ is the applied time-dependent load vector.

(b) Spatial Elements

For the present version of Program ALFE2.A, the two-dimensional solid unit element in the nodal numbering system is that of an four-node solid quadrilateral element. Each quadrilateral element is comprised of two constant strain triangles (2CST). Two distinct ways of subdivision are used in a manner as shown in Figure 59. A standard right-handed Cartesian coordinate system is used for the global coordinates.

(c) Interpolation Functions for a Triangle

The functions of the displacement field $\{\tilde{u}\} = \{u_x, u_y\}$ is approximated by two linear polynomials

$$u_x = \alpha_1 + \alpha_2 x + \alpha_3 y$$

$$u_y = \beta_1 + \beta_2 x + \beta_3 y$$

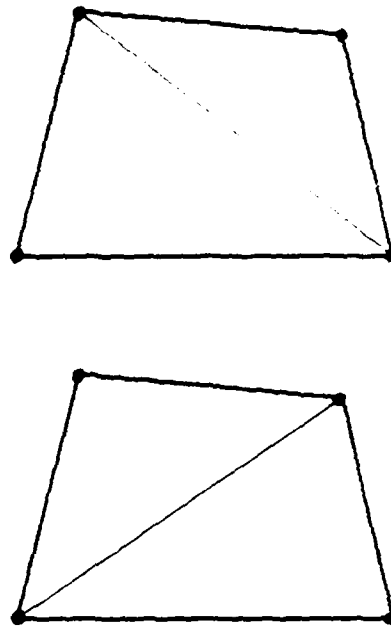


Figure 59. A Quadrangle Comprised by Two Triangles.

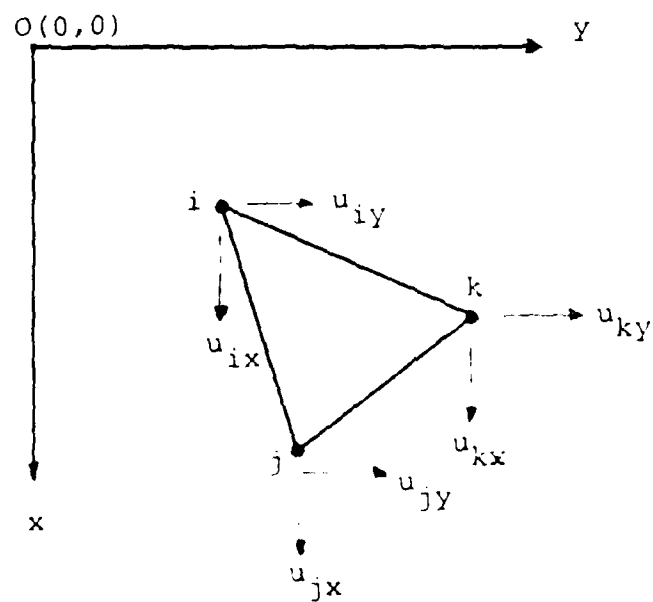


Figure 60. An Element of Triangle

The six constants α_i , β_i ($i = 1, 2, 3$) can be evaluated by solving two sets of three simultaneous linear equations. These simultaneous equations can be obtained by equating the values of the displacements at the triangle nodes, i , j , and k (Figure 6B). The coefficients α_i , and β_i can be solved in terms of the nodal displacements and nodal coordinates. Once these coefficients are determined, we can write the displacement of an arbitrary point within the triangle element as

$$\{u\} = [IN_i, IN_j, IN_k] \{\bar{u}\}$$

where I is a 2×2 unit matrix, N_i , N_j , N_k , or $[N]$ are the shape functions, which are expressed in terms of the nodal coordinates, $\{\bar{u}\}$ is a column vector with six nodal displacement components of the triangle element. The strain-displacement matrix $[B]$ can be defined explicitly in terms of $[N]$.

(d) Triangle Stiffness Matrix

Construct the elastic matrix $[D]$ and carry out the matrix multiplications $[B]^T[D][B]$. After integration of $[B]^T[D][B]$ over the area, the triangle area, in this linear case, a 6×6 triangle stiffness matrix is obtained.

The Young's Modulus and Poisson's ratio (or the Lamé's constants) of the material are required to define the stiffness

matrix of the solid element.

(e) Quadrangle Stiffness Matrix (Averaged 2CST)

The final 8x8 element stiffness matrix is obtained by assembling two 6x6 stiffness matrices. No condensations of internal degrees of freedom are required, since there are no internal nodes in this assemblage.

(f) Mass Matrix

By assuming that all the mass attributed to a node is concentrated at that node, the mass of the quadrilateral element is lumped weightedly to the four nodal points. The mass density of the material is required to define the mass matrix of the element.

(g) Global Stiffness and Mass Matrices Generation

Assemble the stiffness and mass matrices of the individual quadrilateral elements with a common nodal point to obtain the equations of motion at the nodal point. A final banded characteristic global stiffness matrix of order $I \times I$ is obtained, where $I = N \times NF$, N is the number of total nodal points, and NF is the degrees of freedom of each nodal point. The banded global stiffness matrix is highly sparse. The mass matrix is diagonal.

(h) External Load Vector and Prescribed Boundary Conditions

The external forcing function $F(t)$ may be read in as a single vector. Traction boundary conditions are incorporated into the external load vector automatically, i.e. for a free boundary, the load terms associated with the nodes on the boundary are zero. For specified displacements, the stiffness matrix has to be modified.

Any nodal point may be chosen to be one of the four types of boundary conditions, depending on the code number of each nodal point.

$NZRPT(2*N-1)=1$ -- the nodal point is free to traction in the x-direction

$NZRPT(2*N) = 1$ -- the nodal point is free to traction in the y-direction

$NZRPT(2*N-1)=0$ -- the nodal point is fixed in the x-direction

$NZRPT(2*N) = 0$ -- the nodal point is fixed in the y-direction

The character N is the array number of the nodal point.

(i) Time Integration Scheme

The following time integration scheme

$$\begin{aligned}\{u(t+\Delta t)\} &= \{u(t)\} + \{\dot{u}(t)\}\Delta t \\ \{\dot{u}(t+\Delta t)\} &= \{\dot{u}(t)\} + [M]^{-1}[K]\{u(t+\Delta t)\}\Delta t + [M]^{-1}\{F(t)\}\Delta t\end{aligned}$$

is carried out step by step to determine the displacements and velocities in the x, and y directions. The quantity Δt is the time step increment.

(2) PROGRAM DISCRIPTION

The ALFE2.A code consists of Main Program and seven subroutines. These subroutines carry out most of computational steps for spatial stiffness and mass matrix assemblage, and are controlled by Main Program. Following are descriptions of the functions of Main Program and subroutines.

MAIN PROGRAM: Solves overall time-history response of the entire finite element model, and prints the displacements, velocities and accelerations.

SUBROUTINES:

DATAIN - reads in the input data. An automatic finite element mesh generator is introduced.

TRIANG - formulates the stiffness matrix of a single triangle element.

QUAD - formulates the constitutive relations.

STIFT - formulates the stiffness and mass matrices of a single quadrilateral element assembled by two triangular elements.

FRMSTF - formulates the global stiffness and mass matrices, finds the products of the global stiffness matrix and displacements.

FORCE - Introduces the forcing function.

NEW - formulates the quadrilateral stiffness matrix by an alternative approach.

The flow charts of Main Program ALFE2.A and all the subroutines are appended at the end of this section.

Main Program first calls subroutine DATAIN to read and echo print the input master control data, and material properties for each element.

The coordinates for each nodal point and the numbering of a system of nodal points interconnection are generated automatically. As the elemental data are identified, subroutines FRMSTF, STIFT, QUAD, TRIANG are then called to form the global stiffness matrix and global mass vector matrix based on the quadrilateral stiffness and mass matrices. The products of the global stiffness matrix and displacement are computed at the same time as the global stiffness matrix is assembled.

Subroutine FORCE is called to formulate the applied load vector matrix. Time integration is then carried out to determine the nodal displacement and velocity components in each time step increment.

(3) MULTILAYERED MESH GENERATION

The computer Code ALFE2.A itself is applicable to any two-dimensional geological and stratigraphic structures. In this preliminary version ALFE2.A, the regular-size finite element meshes are generated by an automatic mesh generator. The basic element or zone of the generalized grid is a rectangle. Figure 61 shows a 12x12 diagram.

Figure 62 shows the grid-point numbering convention for a 3x3 mesh, i.e. $NROW = (MCOL-1) = 3$, where

$(MCOL-1)$ = number of elements in the x-direction,

$NROW$ = number of elements in the y-direction.

The grid points are numbered in the order: Top to Bottom, Right to Left.

Figure 63 provides an example showing the convention for numbering the elements for 3x3 mesh. The elements are numbered in the order Top to Bottom, and Right to Left. In this mesh generator, $(MCOL-1)$, and $NROW$ are not necessarily to be the same.

In this version of ALFE2.A, the automatic finite element mesh generation subroutine is limited to nine horizontal layers. That is, the finite element mesh can model various different combinations corresponding to one to nine different materials. For example, in lines 3-11 of the data input, if we assign the same elastic parameter constants for each layer, the mesh will simulate a homogeneous medium, if we assign different elastic parameter constants to the first layer from those of the other eight layers, then we obtain a one-layered medium, and so forth.

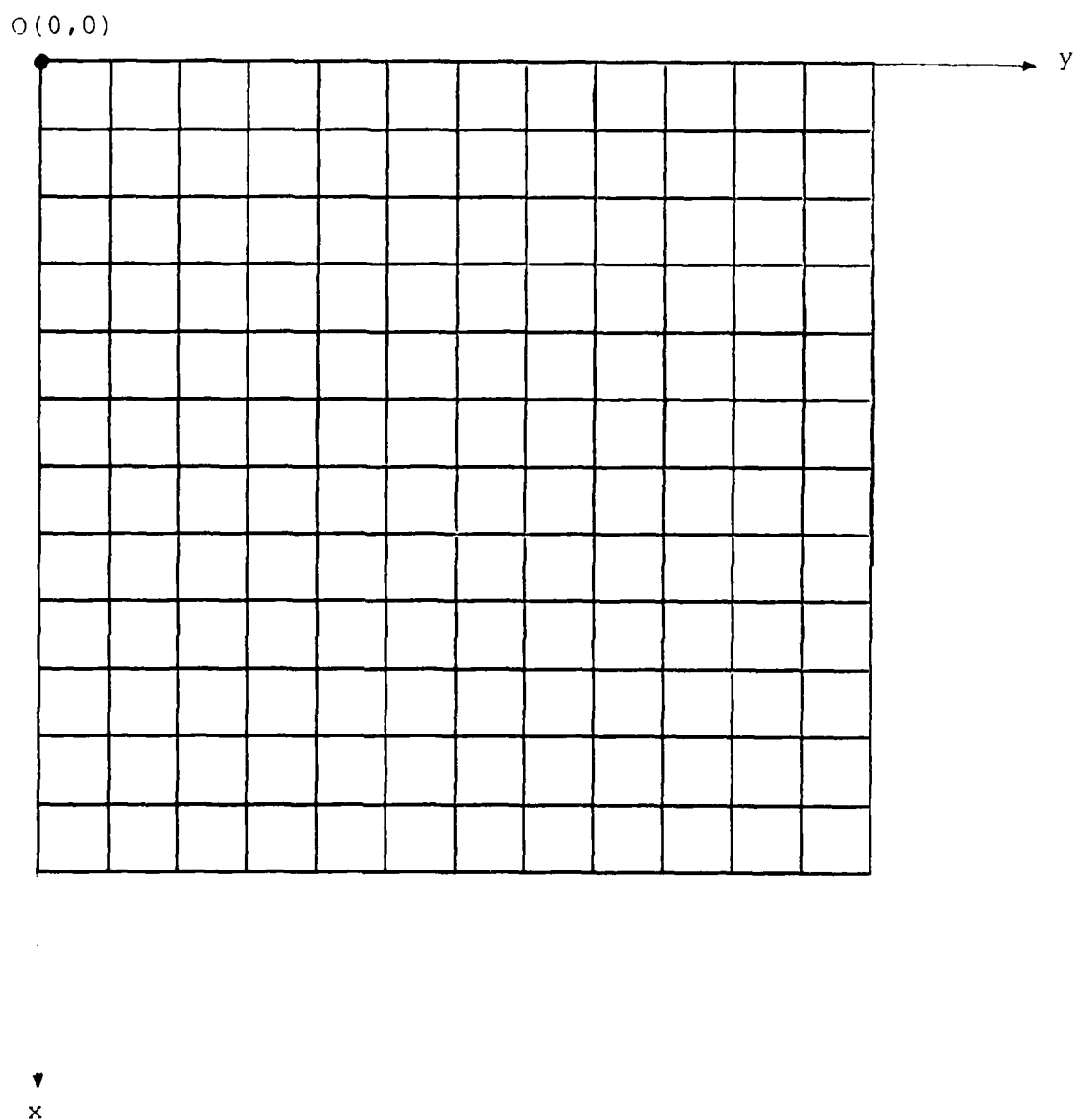


Figure 61. A 12x12 Finite Element Mesh.

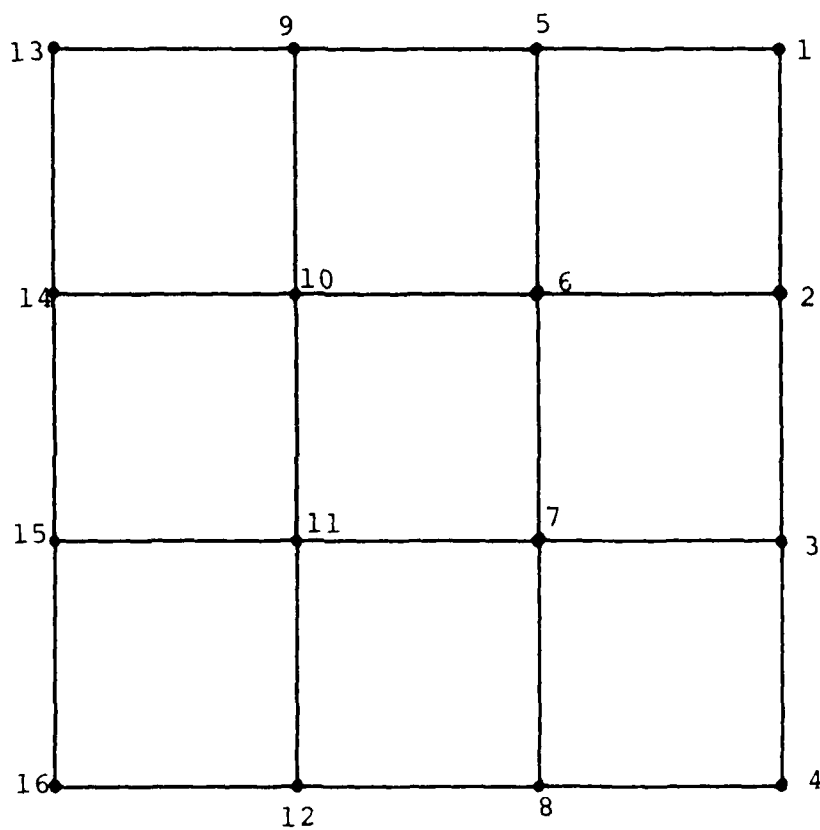


Figure 62. An Example Showing the Convention for Numbering the Nodal Points in PROGRAM ALFE2.A.

7	4	1
8	5	2
9	6	3

Figure 63. An Example Showing the Convention for
Numbering of Elements in PROGRAM ALFE2.A.

(4) GUIDE FOR DATA INPUT

BASIC PARAMETERS (FORMAT 3I5)

<u>COLUMN</u>	<u>VARIABLE</u>	<u>DEFINITION</u>
1-5	IFLAG	Back-up Option IFLAG=0 : Start from beginning IFLAG≠0 : Restart from its last executed time step
6-10	NBSTEP	Back-up by NBSTEP time steps
11-15	ISRC	Code for source type, (temporarily set to "1", means directional force source)

BASIC PARAMETERS (FORMAT 2I5, F15.8)

<u>COLUMN</u>	<u>VARIABLE</u>	<u>DEFINITION</u>
1-5	NMATRL	Number of materials
6-10	NSTEP	Total number of time steps to be calculated
11-25	DELTAT	Time-step increment

MATERIAL PROPERTIES (FORMAT 3F15.4)

<u>COLUMN</u>	<u>VARIABLE</u>	<u>DEFINITION</u>
1-15	VP	Compressional wave velocity of the material
16-30	VS	Shear wave velocity of the material
31-45	RHO	Mass density of the material

LOADING POINT AND MATERIAL-ELEMENT CONNECTION (FORMAT 1115)

<u>COLUMN</u>	<u>VARIABLE</u>	<u>DEFINITION</u>
1-5	NS	Force applied on NS-th vertical nodal point
6-10	NROWSO	Force applied on NRORSO-th horizontal nodal point
11-15	MH1	Vertical number of elements for the first layer
16-20	MH2	Vertical number of elements for the first two layers
21-25	MH3	Vertical number of elements for the first three layers
26-30	MH4	Vertical number of elements for the first four layers
31-35	MH5	Vertical number of elements for the first five layers
36-40	MH6	Vertical number of elements for the first six layers
41-45	MH7	Vertical number of elements for the first seven layers
46-50	MH8	Vertical number of elements for the first eight layers
51-55	MH9	Vertical number of elements for the first nine layers

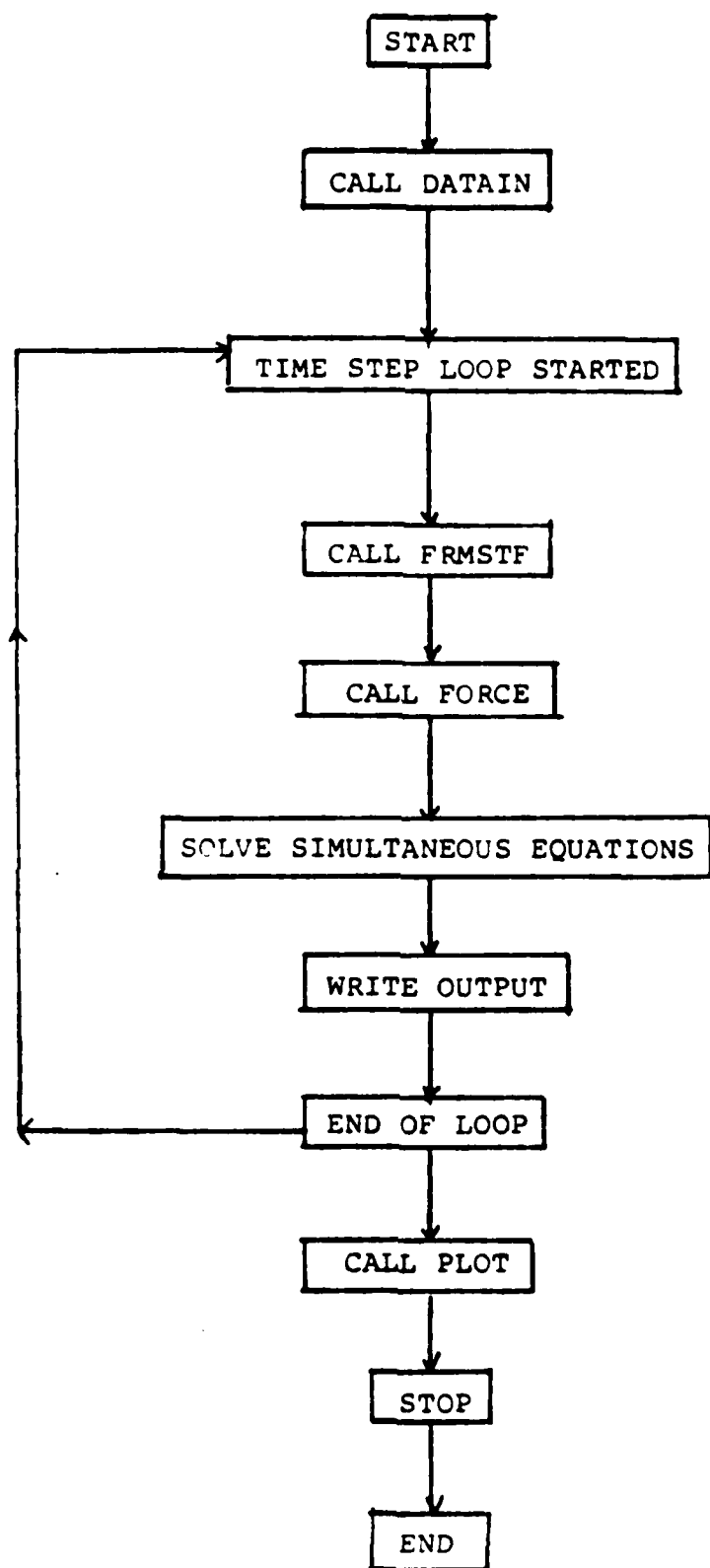
COORDINATE AND NODAL POINT CONTROL (FORMAT 215,2E16.4)

<u>COLUMN</u>	<u>VARIABLE</u>	<u>DEFINITION</u>
1-5	NROW	Number of element in the y-direction
6-10	MCOL	Number of nodal points in the x-direction
11-15	XX	Size of quadrilateral element in the x-direction
16-20	YY	Size of quadrilateral element in the y-direction

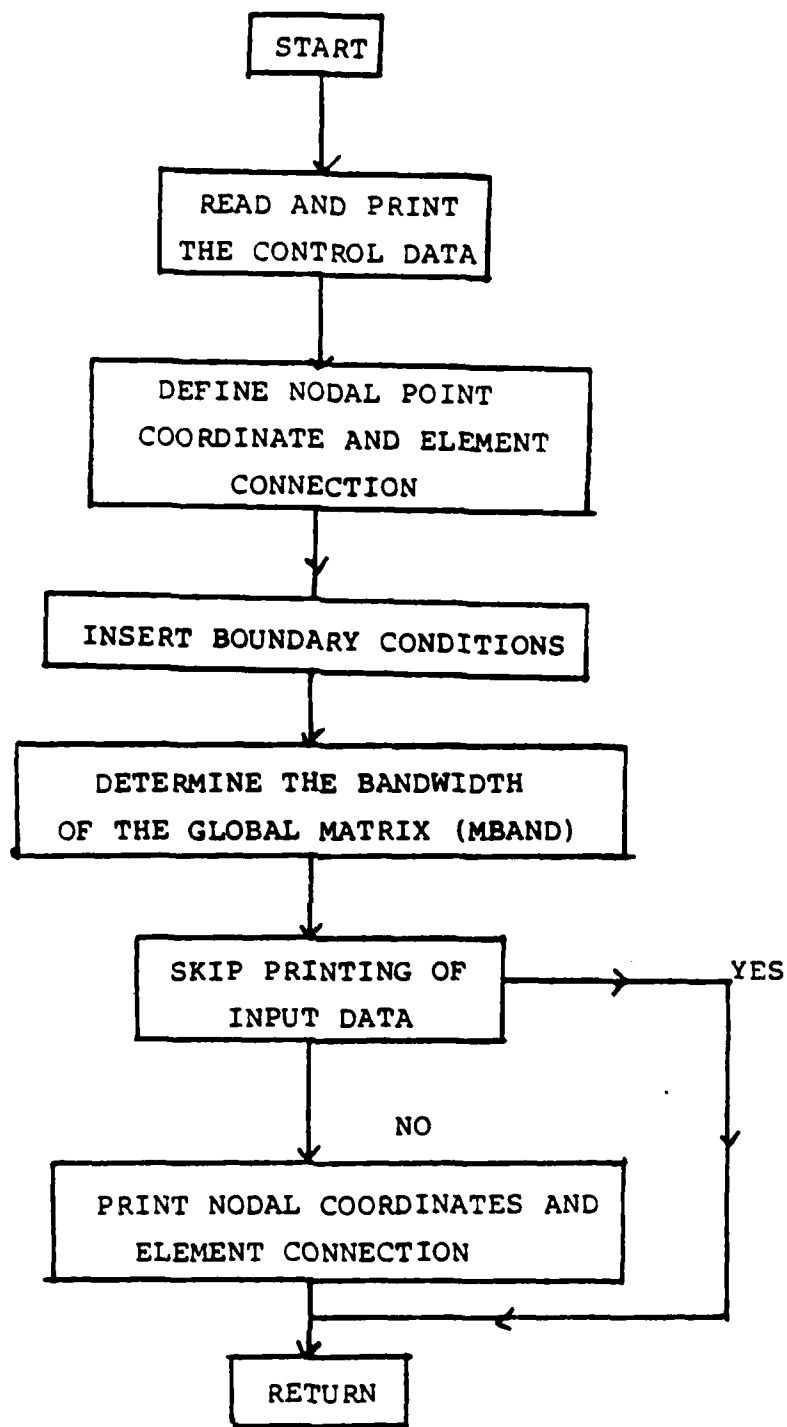
(5) DEFINITION OF OTHER MAJOR VARIABLES

<u>VARIABLE</u>	<u>DEFINITION</u>
NODEPT	Number of the total nodal points
NELMNT	Number of the total elements
NF	Degrees of freedom of each nodal point
MAXNOD	Maximum number of nodal points for each element (Quadrangle)
NEQTN	Total number of equations
NELMAR	Element connecting array
AX,BX,CX,DX, AY,BY,CY,DY	Coordinates of the four nodal points of quadrilateral element with respect to the global system
S(6,6)	Stiffness matrix of triangular element
AREA	Area of triangular element
STIFMX(8,8)	Stiffness matrix of quadrilateral element
SMX(8,8)	Mass matrix of quadrilateral element
E(N)	Young's Modulus of the N-th material
PNU(N)	Poisson's ratio of the N-th material
PLUMP(N)	Lame's constant λ of the N-th material
PMU(N)	Lame's constant μ of the N-th material
D(3,3)	Constitutive matrix [D]
B(3,6)	Strain-displacement matrix [B]
NZRPT	Boundary condition code
UUU	Displacement component of each nodal point
VVV	Velocity component of each nodal point
UUI	Displacement component of each nodal point for different type of non-reflecting boundaries
VVI	Velocity component of each nodal point for different type of non-reflecting boundaries
XXX	Matrix product of $[K] \{u\}$
MBAND	Half-band width of assemblage equations (irrelevant to the present code ALFE2.A)

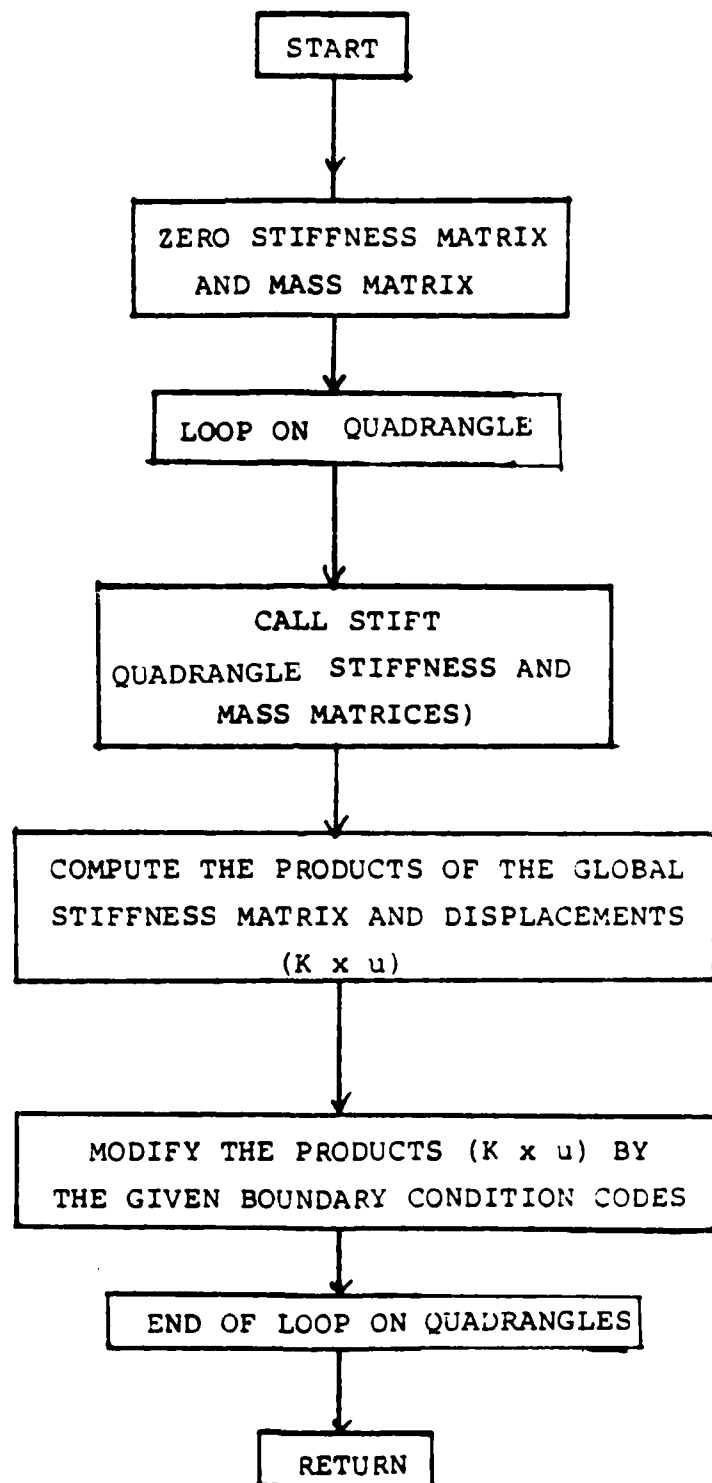
(5) FLOW CHARTS OF MAIN PROGRAM ALFE2.A AND SUBROUTINES



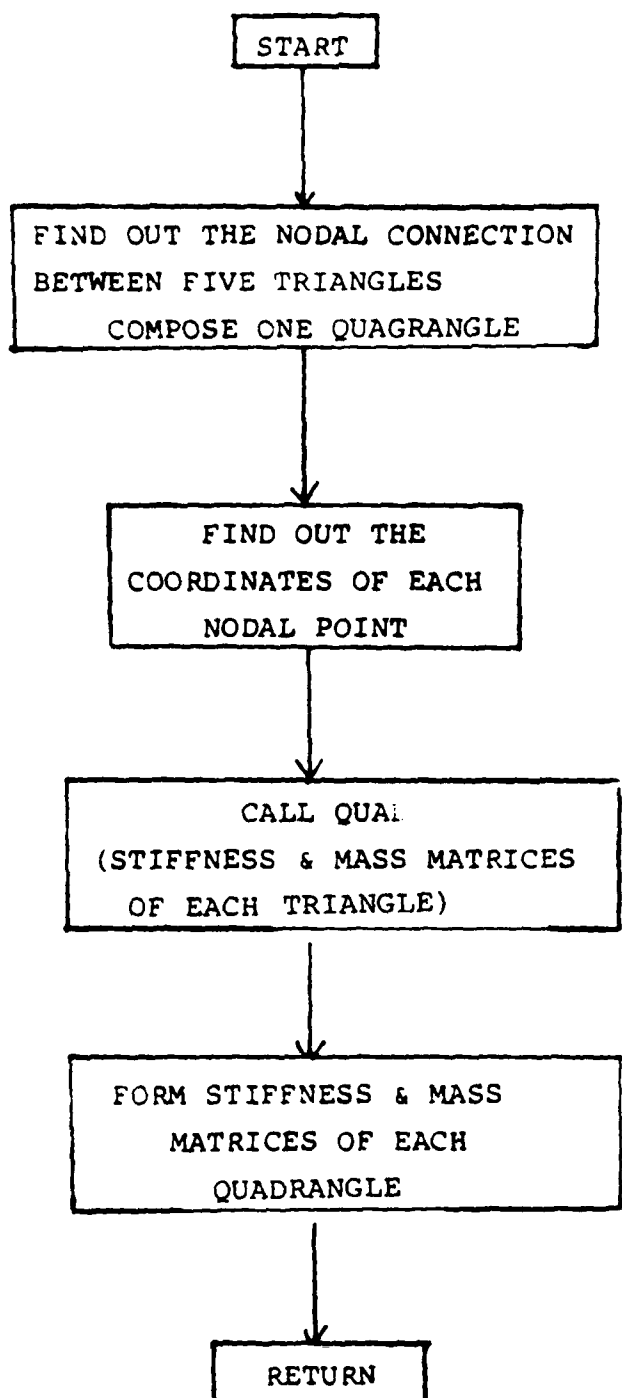
MAIN PROGRAM



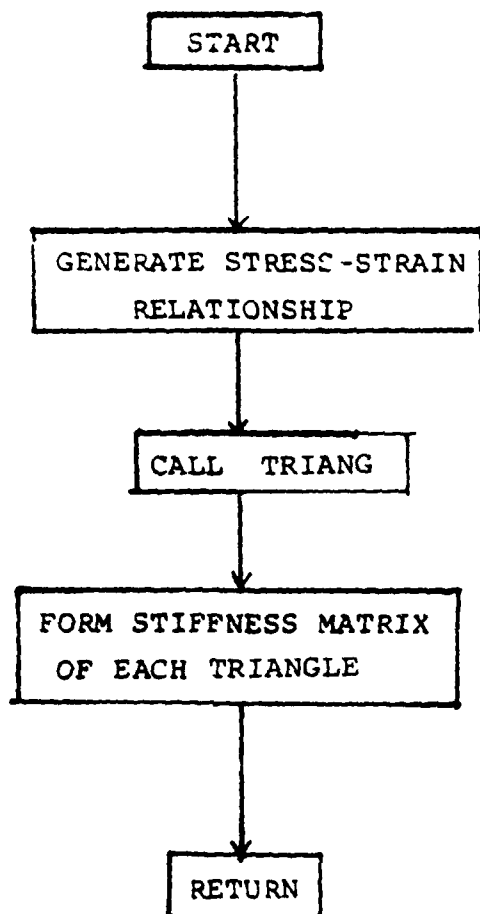
SUBROUTINE DATAIN



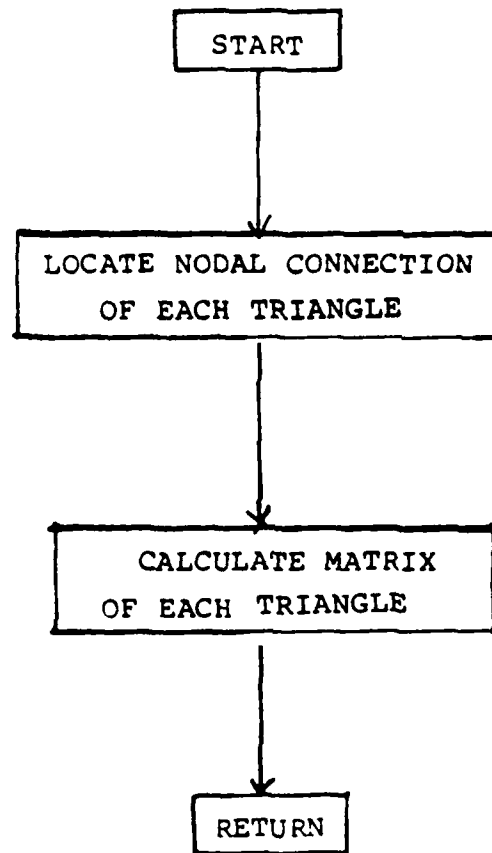
SUBROUTINE FRMSTF



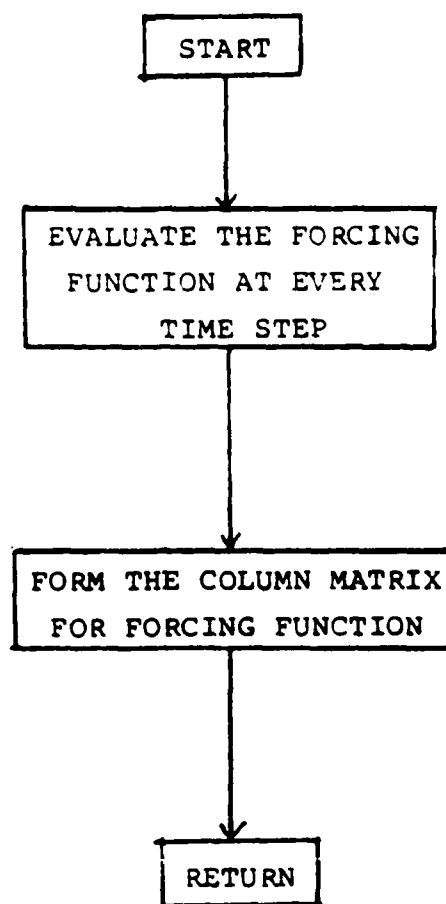
SUBROUTINE STIFT



SUBROUTINE QUAD



SUBROUTINE TRIANG



SUBROUTINE FORCE

APPENDIX

AN ANTICLINAL ELASTIC MODEL

(Demonstration of the Radiation Patterns Strongly
Depends on the Nature of Source)

In order to demonstrate the differences of a vertical forcing line source and an omni-directional line source, we consider a two-dimensional elastic anticlinal model as shown in Figure 1-A with the compressional velocities of each medium: $v_{p1} = 7,000$ ft/sec, $v_{p2} = 5,900$ ft/sec, and $v_{p3} = 6,400$ ft/sec, respectively, and the densities $\rho_1 = 2.1$ gm/cm³, $\rho_2 = 1.8$ gm/cm³, and $\rho_3 = 1.9$ gm/cm³. The Poisson's ratios are assumed to be 0.25 for each medium. The horizontal range is 2,000 ft, the depth to the top of the anticline is 1,000 ft. Two different kinds of source are applied to point S, namely, (i) a vertical force, and (ii) an omni-directional force. The source is located at a depth of 200 ft at the center of the horizontal range. The source function is taken to be the first derivative of Gaussian with a duration of 0.04928 sec. The center frequency of this source function is approximately 41 Hz. The magnitudes of all the forcing functions for a vertical and an omni-directional

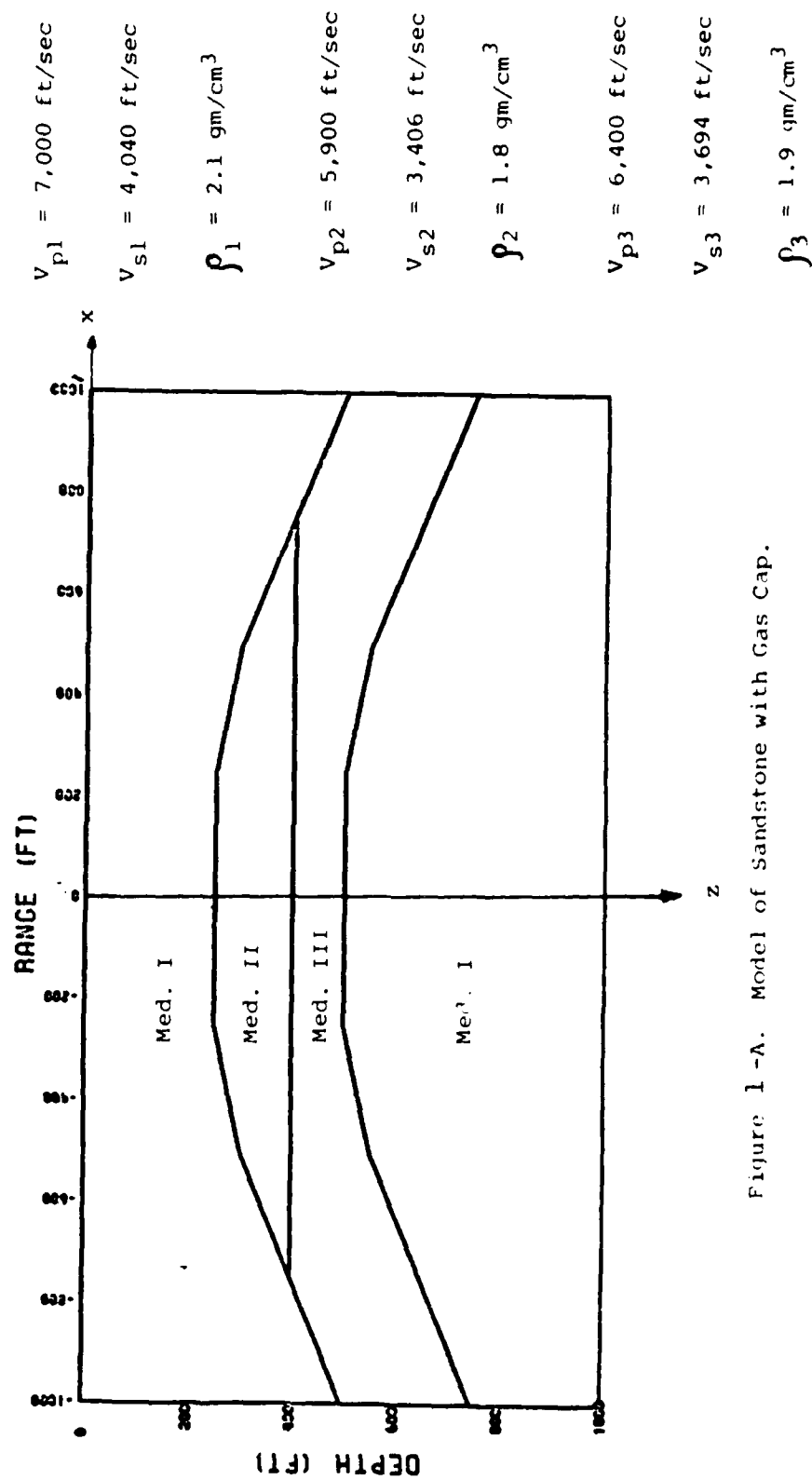


Figure 1-A. Model of Sandstone with Gas Cap.

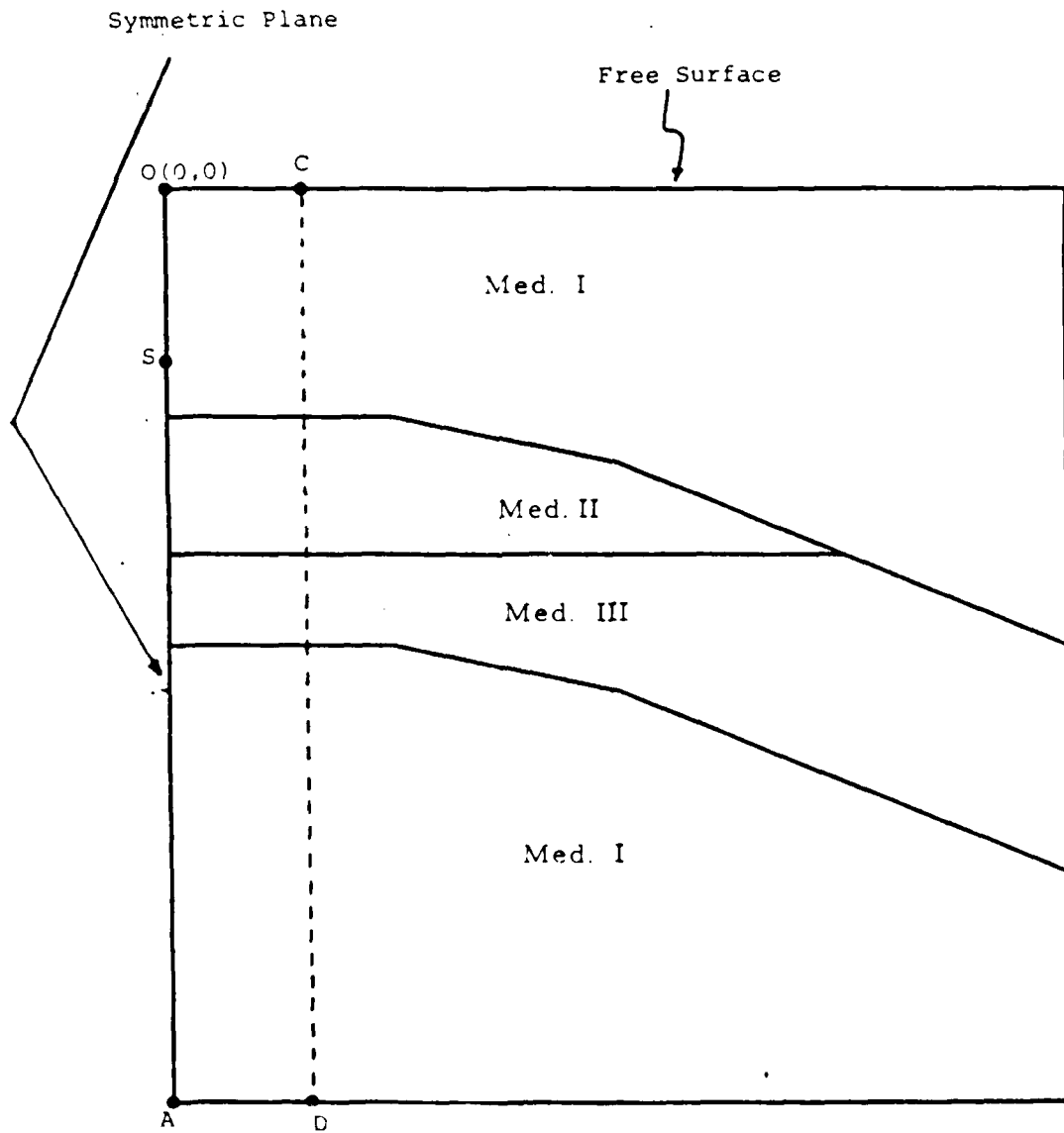


Figure 1-B. Half Size of the Sandstone Model.

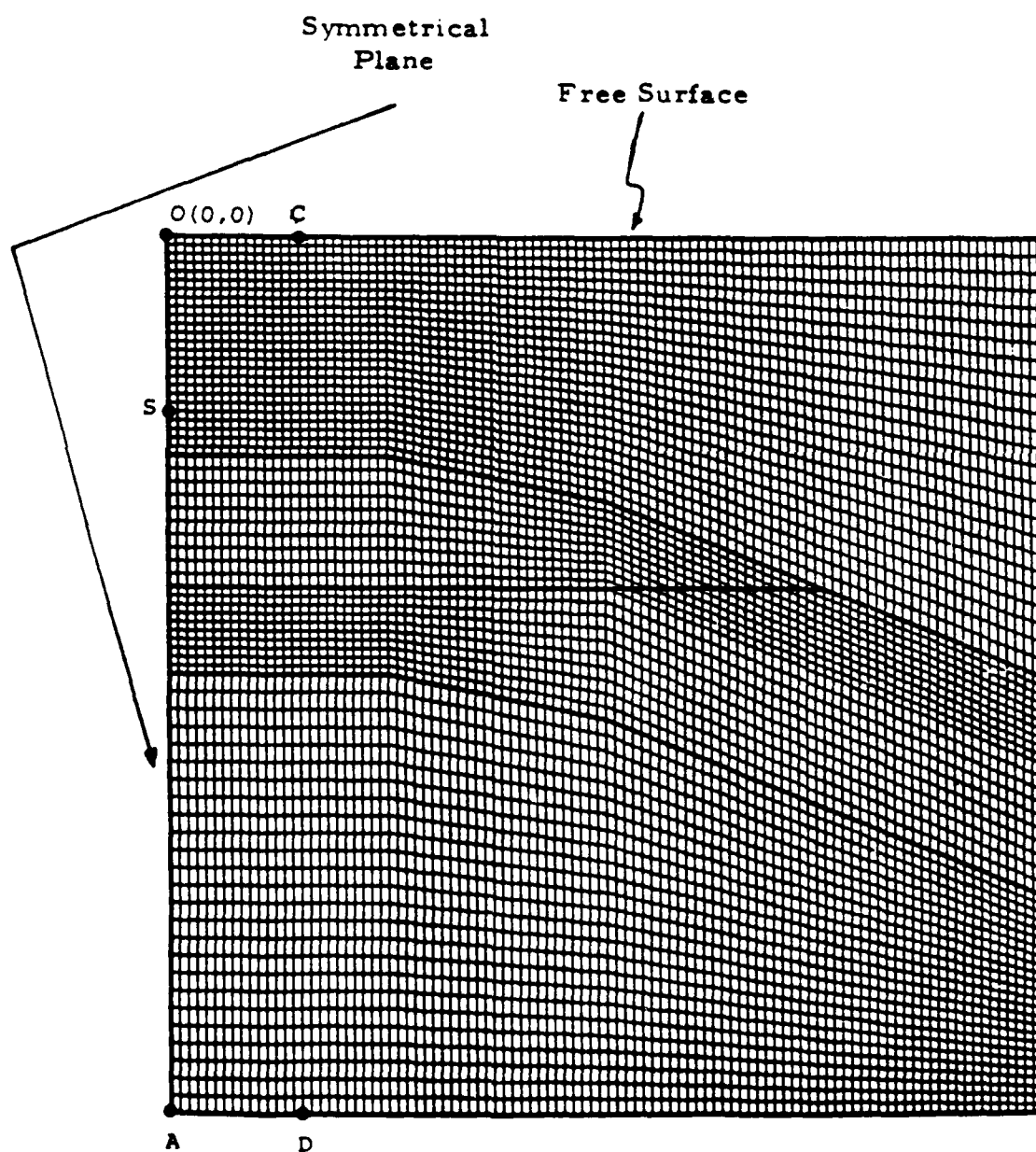


Figure 1-C. Finite Element Mesh for the Model.

line source used are the same. Taking the advantage of symmetry with respect to the z-axis, we use only one half of the model (Figure 1-B). The finite element mesh is automatically generated, and is given in Figure 1-C. The smallest element size, Δs , is 10 ft, and the time step, Δt , is taken to be 0.88 msec. Three synthetic seismograms for each case, one along the free surface, and two along the vertical planes OA and CD (see Figure 1-B) are recorded. Figures 2-A and 2-B are the vertical and horizontal-component displacements along the free surface for the vertical force line source problem. There are 101 traces plotted. Figures 3-A,B and 4-A,B are the vertical and horizontal components of the displacement along the vertical planes OA and CD for the vertical-force source problem, respectively. In Figures 3 and 4, there are 71 uneven spaced traces plotted, according to the actual finite element mesh locations. Figure 5, 6, and 7 are the vertical and horizontal-components of the displacements along the free surface, the vertical planes OA and CD, respectively for an omni-directional line source problem.

For interpretation, we adopt the following notations for the arrivals in Figures 2 to 7:

(1) subscripts denote medium, prime denotes the last medium.

(2) the arrival of compressional wave denotes P and that of shear wave S.

(3) the wave arrival from the source to the free surface is in l.c. P_1 .

(4) Reflected P once from source to surface, is denoted by P_1P_1 , and reflected again from the interface of medium I and II is $P_1P_1P_1$ and so on.

In Figures 2 and 5, the primary arrivals, P_1 , s_1P_1 -diffracted, S, Rayleigh, and the multi-reflected P waves from the bottom of medium I, labeled as P_1P_1 , $P_1P_1P_1P_1$, $P_1P_1P_1P_1P_1P_1$, have been identified. It is clearly seen that the responses of the free surface, and along the vertical planes OA and CD are significantly different between a vertical force line source and an omni-directional force line source. In Figure 2, the vertical displacement is dominated by Rayleigh waves, which also are major contributors to the horizontal displacement. The s_1P_1 -diffracted waves are masked by the arrivals of multiple P reflections. The s_1P_1 -diffracted waves start on the free surface around 150 ft away from point O with an approximate arrival time of 0.0618 sec after the initial detonation. In Figure 5, there are virtually no S waves arrivals before the waves reach any boundary. The predominant wave in this case is P wave.

Comparison of Figure 3-A with Figure 6-A, the vertical-components of the displacement along the plane OA due to a vertical-force line source (VFS) and an omni-directional line source (OLS), respectively shows that:

(1) not only wave forms are different, but also p_1 and P_1 are stronger for VFS than these for OLS.

(2) the late arrivals of $p_1 p_1 p_1 p_1$ and $p_1 p_1 p_1 p_1 \dots$ are clearer for OLS than these for VFS.

(3) except the wave forms are different, $p_1 p_1 p_2 p_3 p_1$ are clearly identifiable for both VFS and OLS.

(4) the initial displacements of $p_1 p_1 p_2 p_3 p_1$ are stronger for VFS than these for OLS

(5) since the plane OA contains the source S, there are no displacements in the horizontal-components.

Comparison of Figure 4-A with Figure 7-A, the vertical-components of the displacement along the vertical plane CD due to VSF, and OLS, respectively shows that:

(1) except shifted in the arrival times and smaller in magnitudes, the characteristics of the primary arrivals namely p_1 and P_1 , are virtually identical to these along the plane OA.

Figure 2-A. SYNTHETIC SEISMOGRAM ALONG FREE SURFACE
SUBJECTED TO A SOURCE OF VERTICAL FORCE

V-DISPLACEMENT

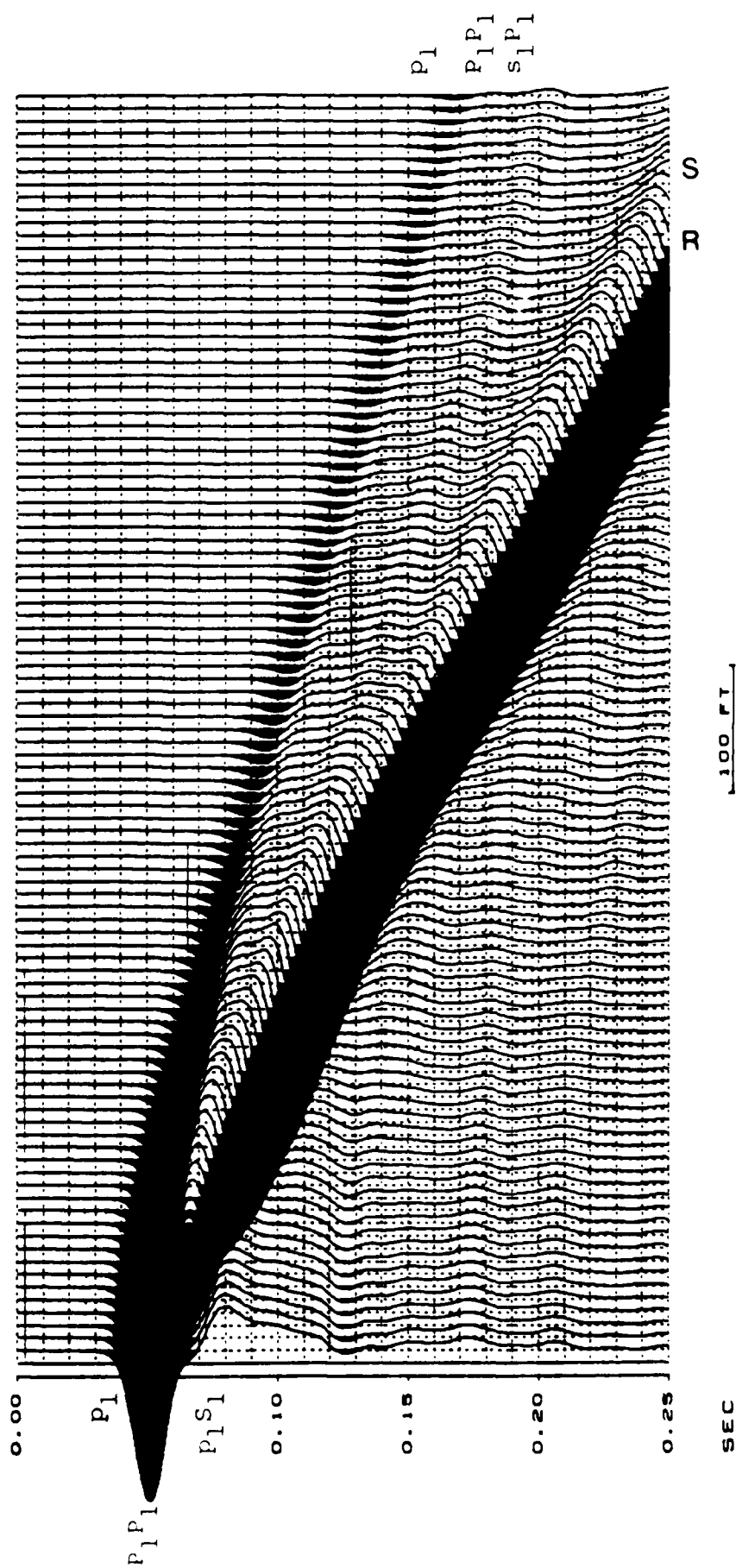


Figure 2-B. SYNTHETIC SEISMOGRAM ALONG FREE SURFACE
SUBJECTED TO A SOURCE OF VERTICAL FORCE

H-DISPLACEMENT

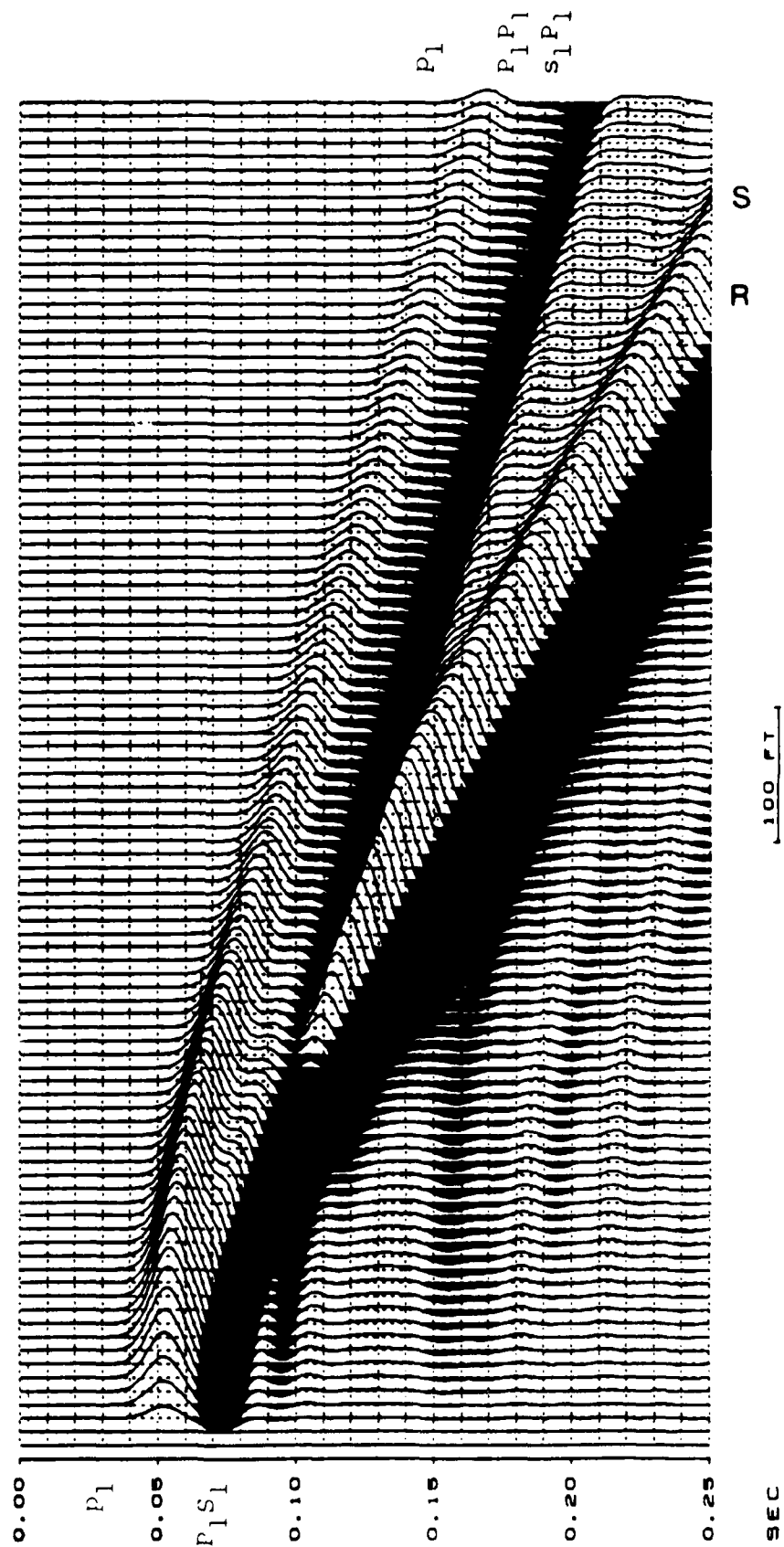


FIGURE 3 -A. SYNTHETIC SEISMOGRAM ALONG VERTICAL PLANE OR
SUBJECTED TO A SOURCE OF VERTICAL FORCE

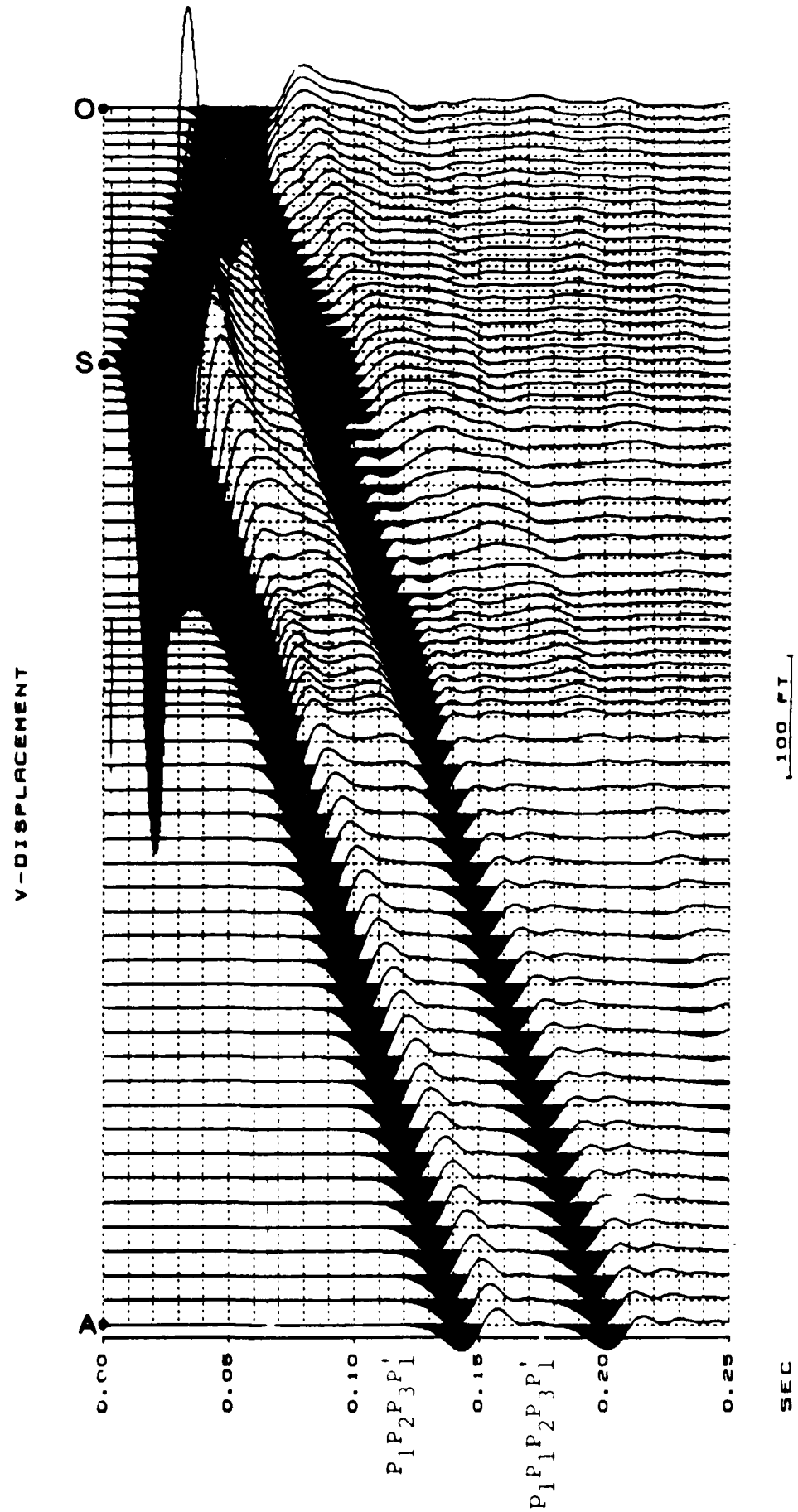


FIGURE 3-B. SYNTHETIC SEISMOGRAM ALONG VERTICAL PLANE OR
SUBJECTED TO A SOURCE OF VERTICAL FORCE

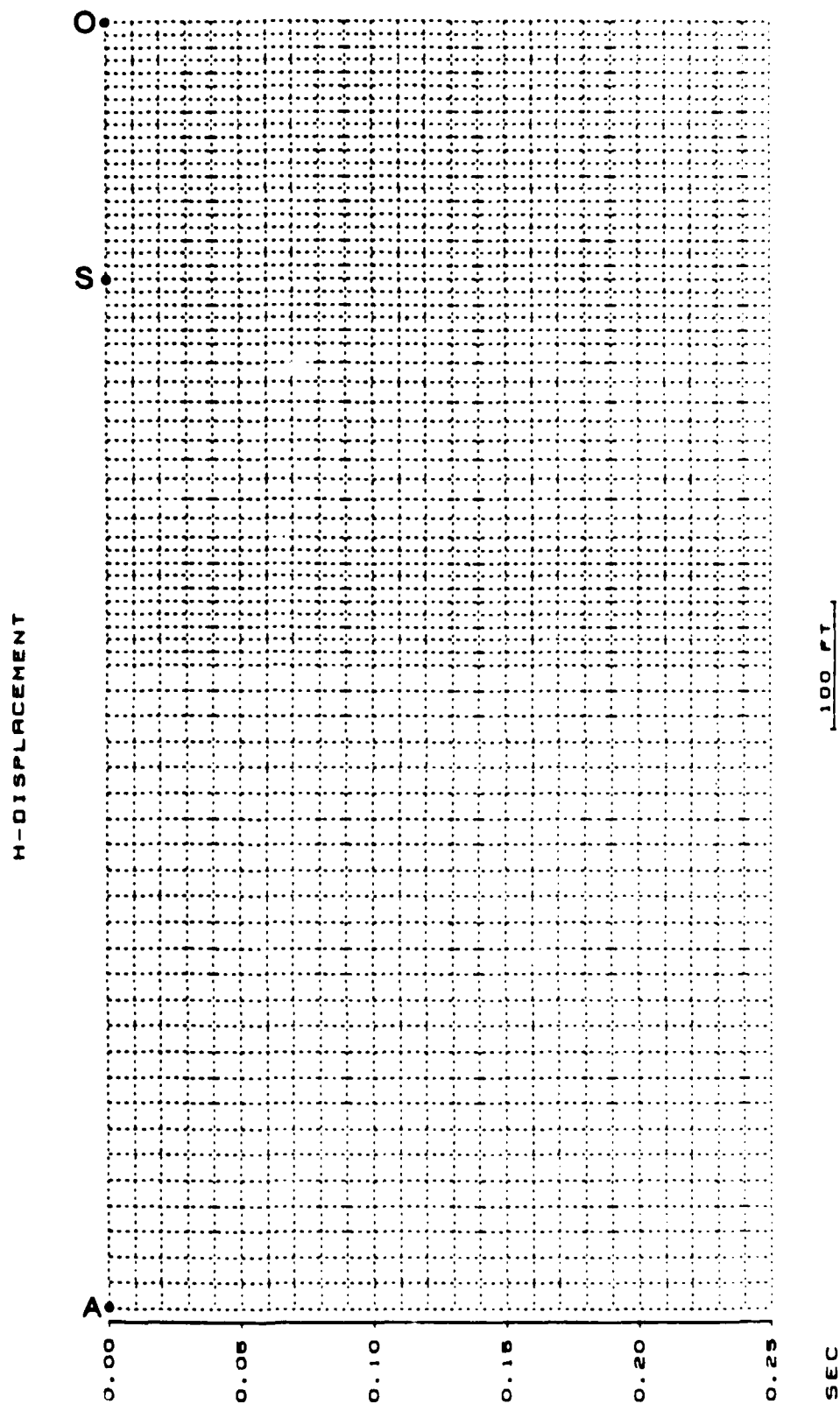


FIGURE 4 -A. SYNTHETIC SEISMOGRAM ALONG VERTICAL PLANE CD
SUBJECTED TO A SOURCE OF VERTICAL FORCE

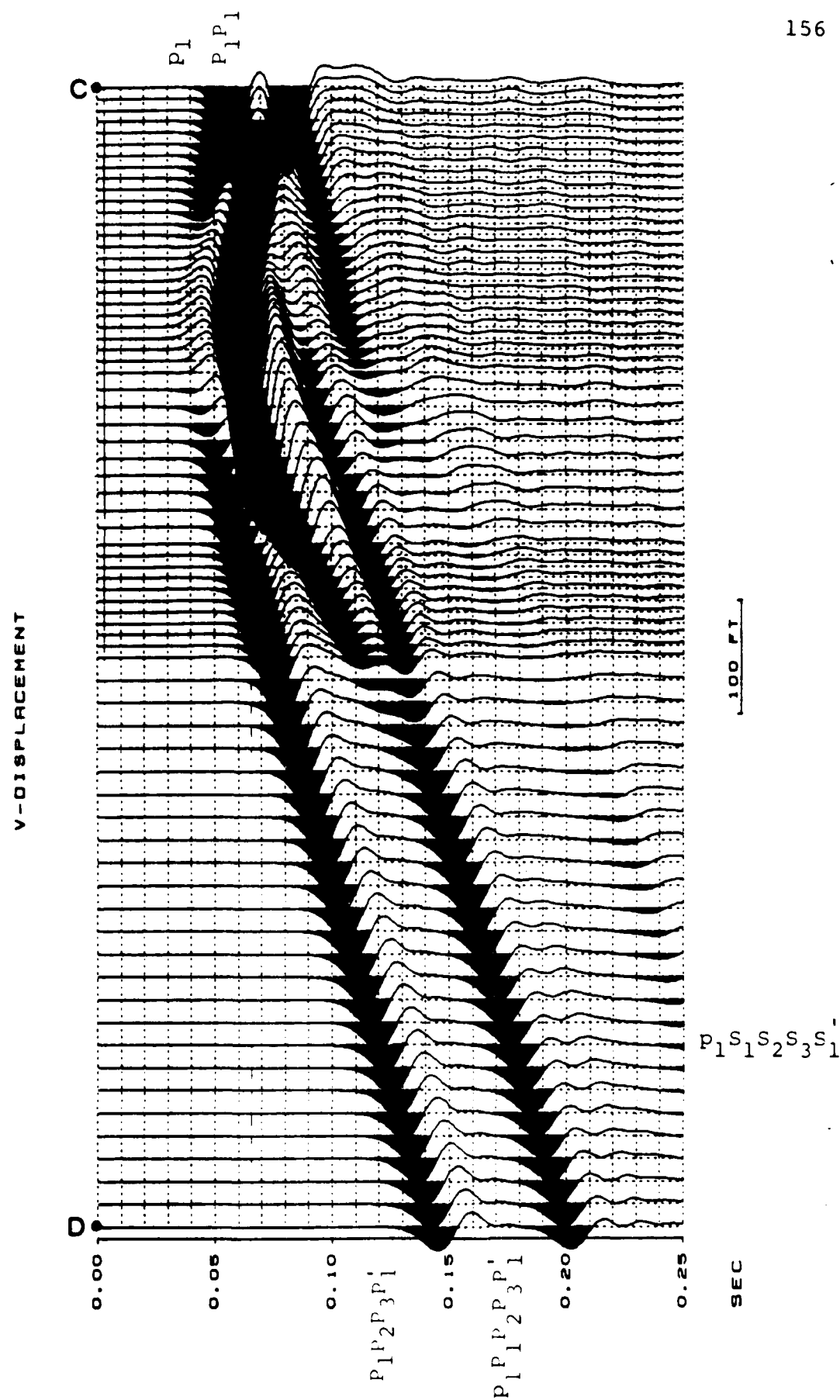


FIGURE 4-B. SYNTHETIC SEISMOGRAM ALONG VERTICAL PLANE CD
SUBJECTED TO A SOURCE OF VERTICAL FORCE

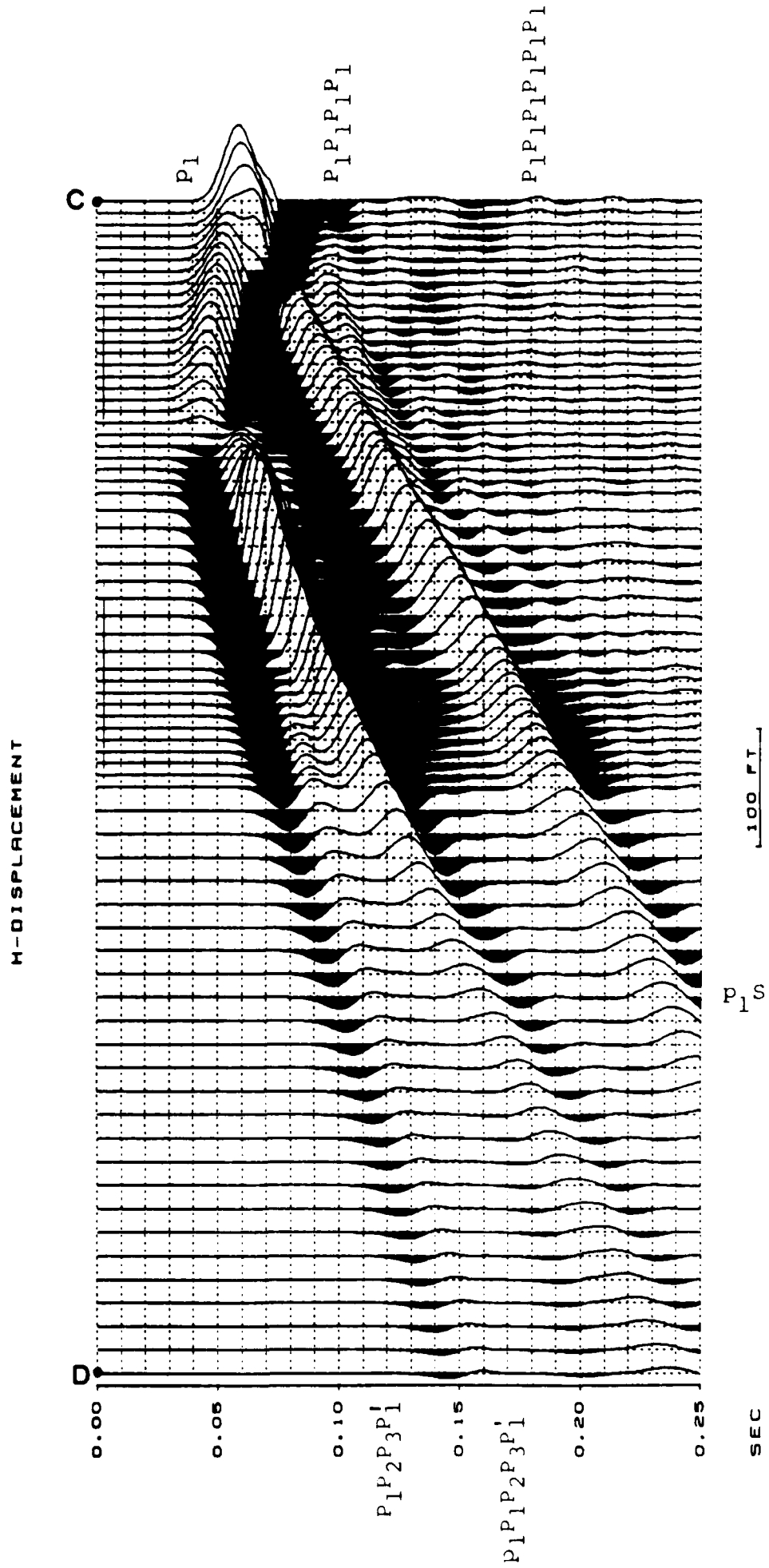


Figure 5-A. SYNTHETIC SEISMOGRAM ALONG FREE SURFACE
SUBJECTED TO AN OMNI-DIRECTIONAL POINT SOURCE

V-DISPLACEMENT

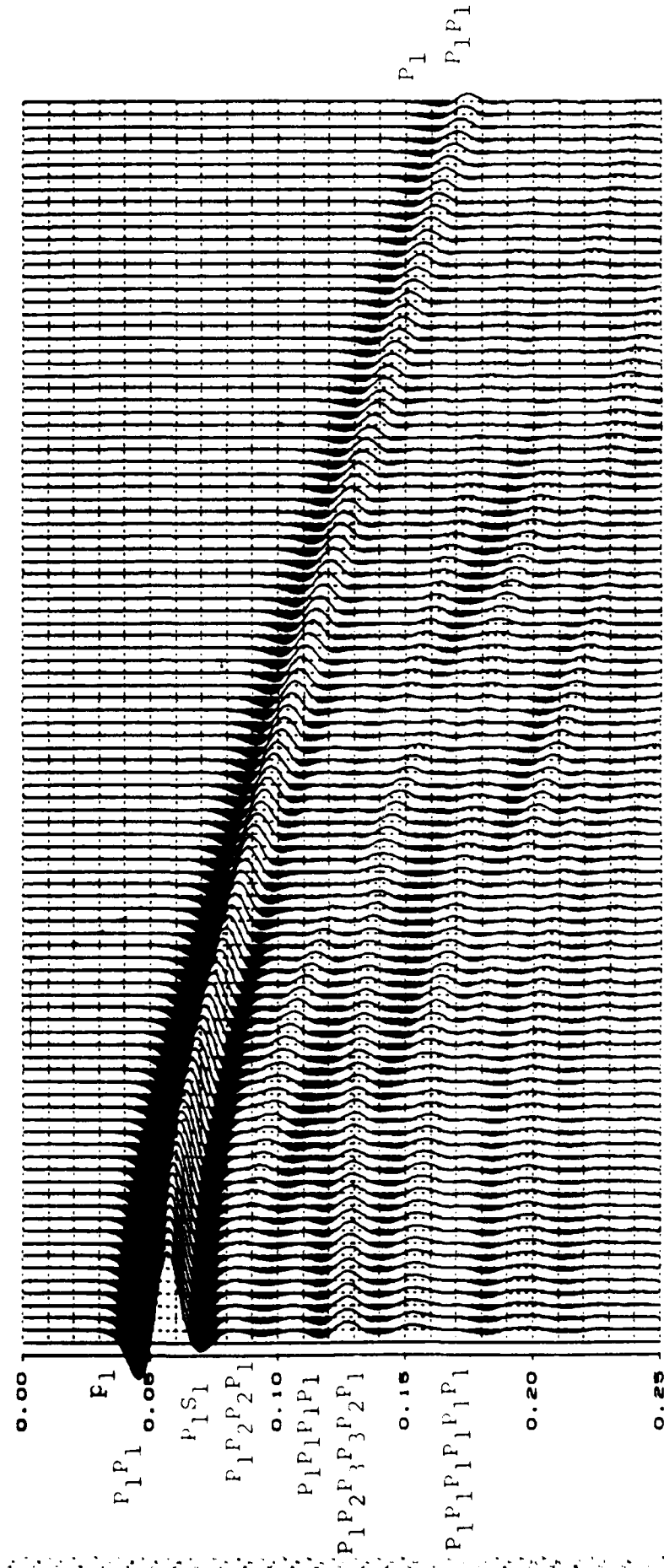


Figure 5-B. SYNTHETIC SEISMOGRAM ALONG FREE SURFACE
SUBJECTED TO AN OMNI-DIRECTIONAL POINT SOURCE

H-DISPLACEMENT

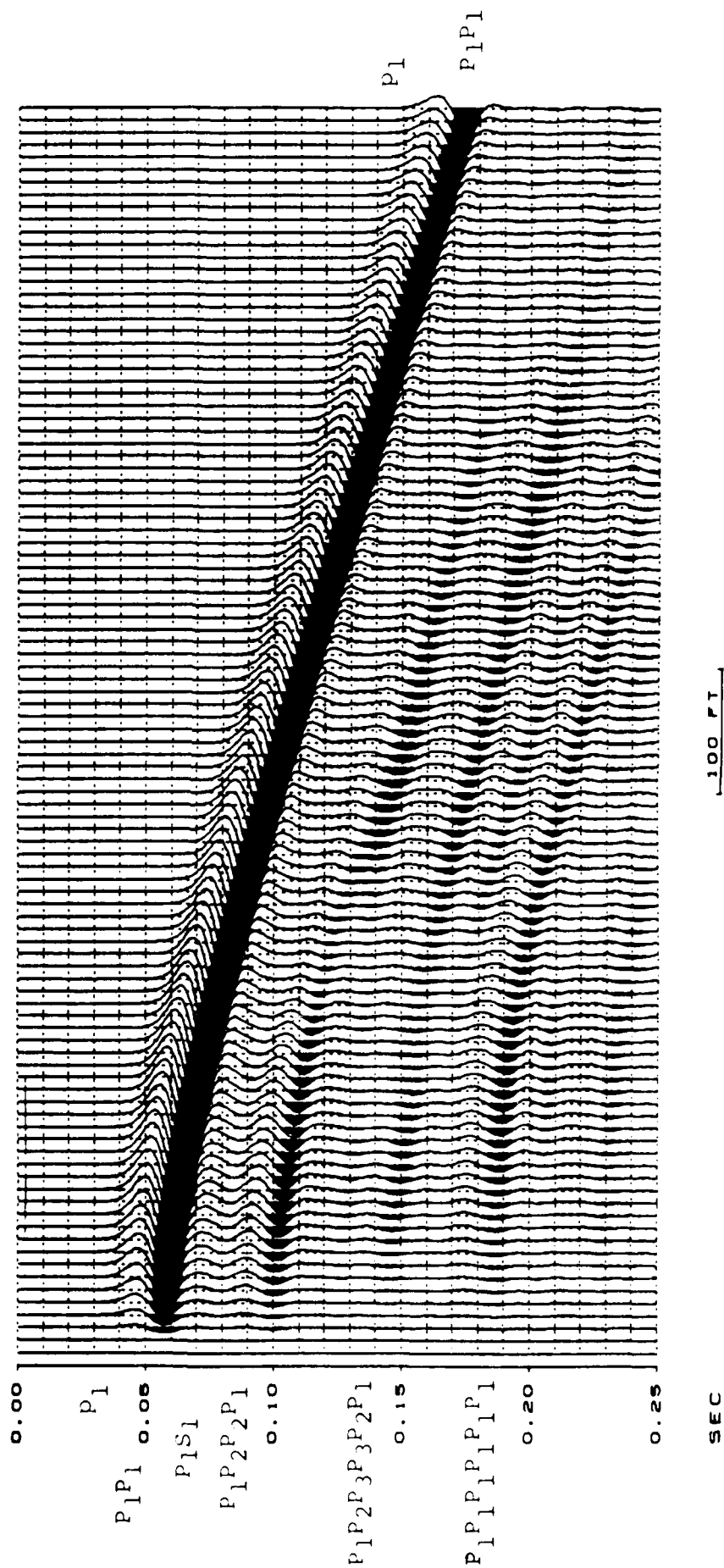


FIGURE 6 -A. SYNTHETIC SEISMOGRAM ALONG VERTICAL PLANE OR
SUBJECTED TO AN OMNI-DIRECTIONAL LINE SOURCE

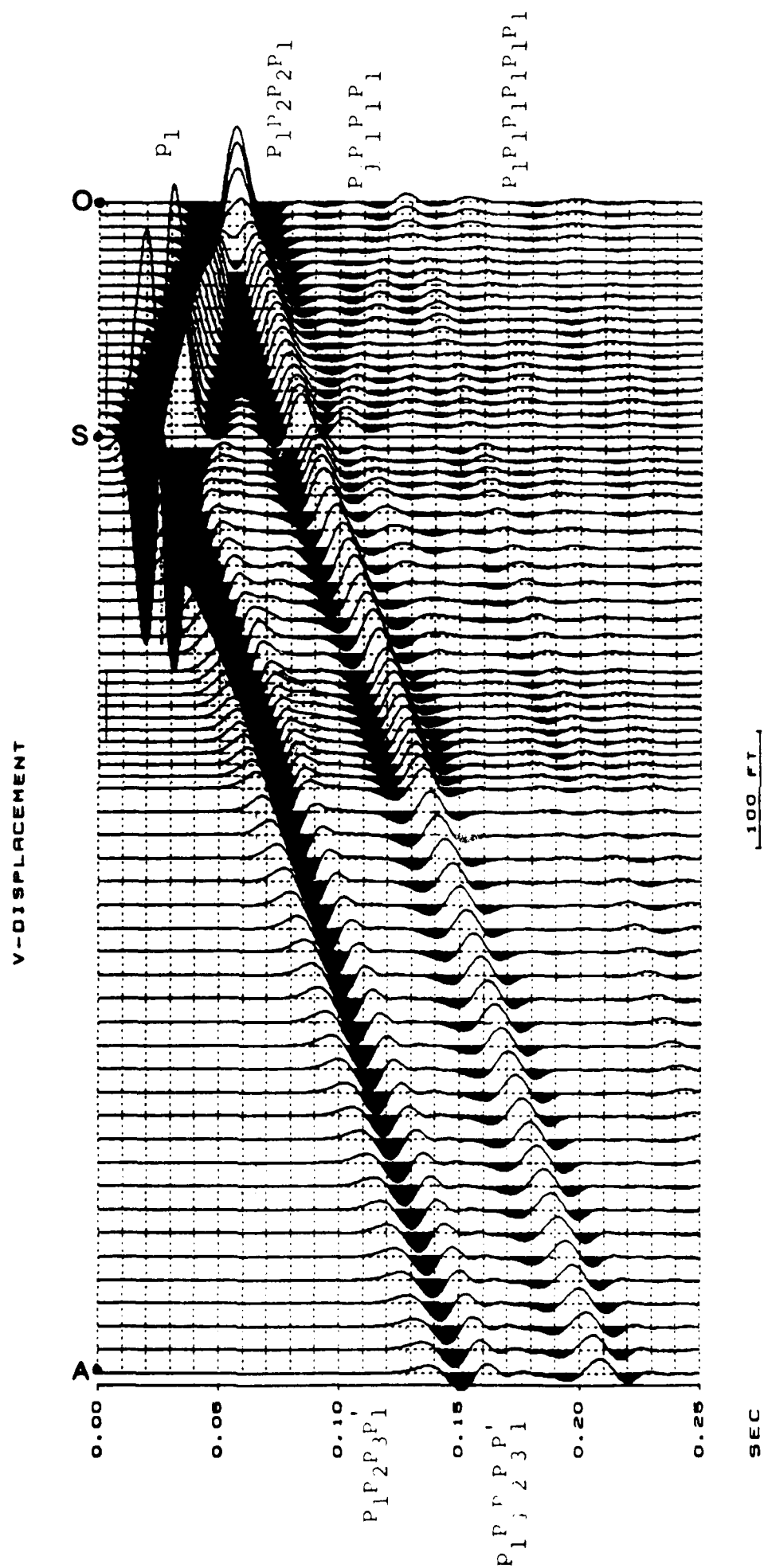


FIGURE 6-B. SYNTHETIC SEISMOGRAM ALONG VERTICAL PLANE OR
SUBJECTED TO AN OMNI-DIRECTIONAL LINE SOURCE

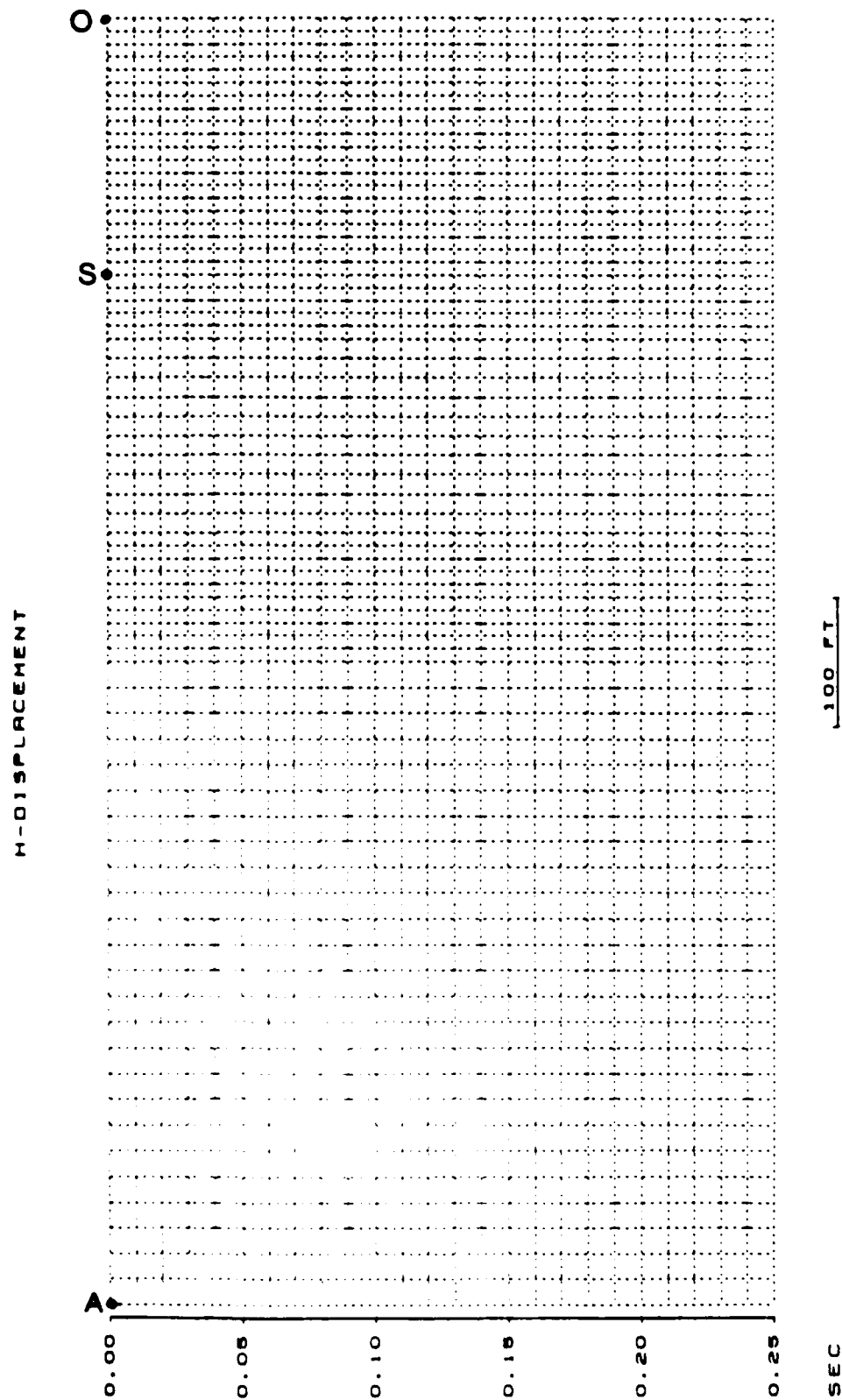


FIGURE 7 -A. SYNTHETIC SEISMOGRAM ALONG VERTICAL PLANE CD
SUBJECTED TO AN OMNI-DIRECTIONAL LINE SOURCE

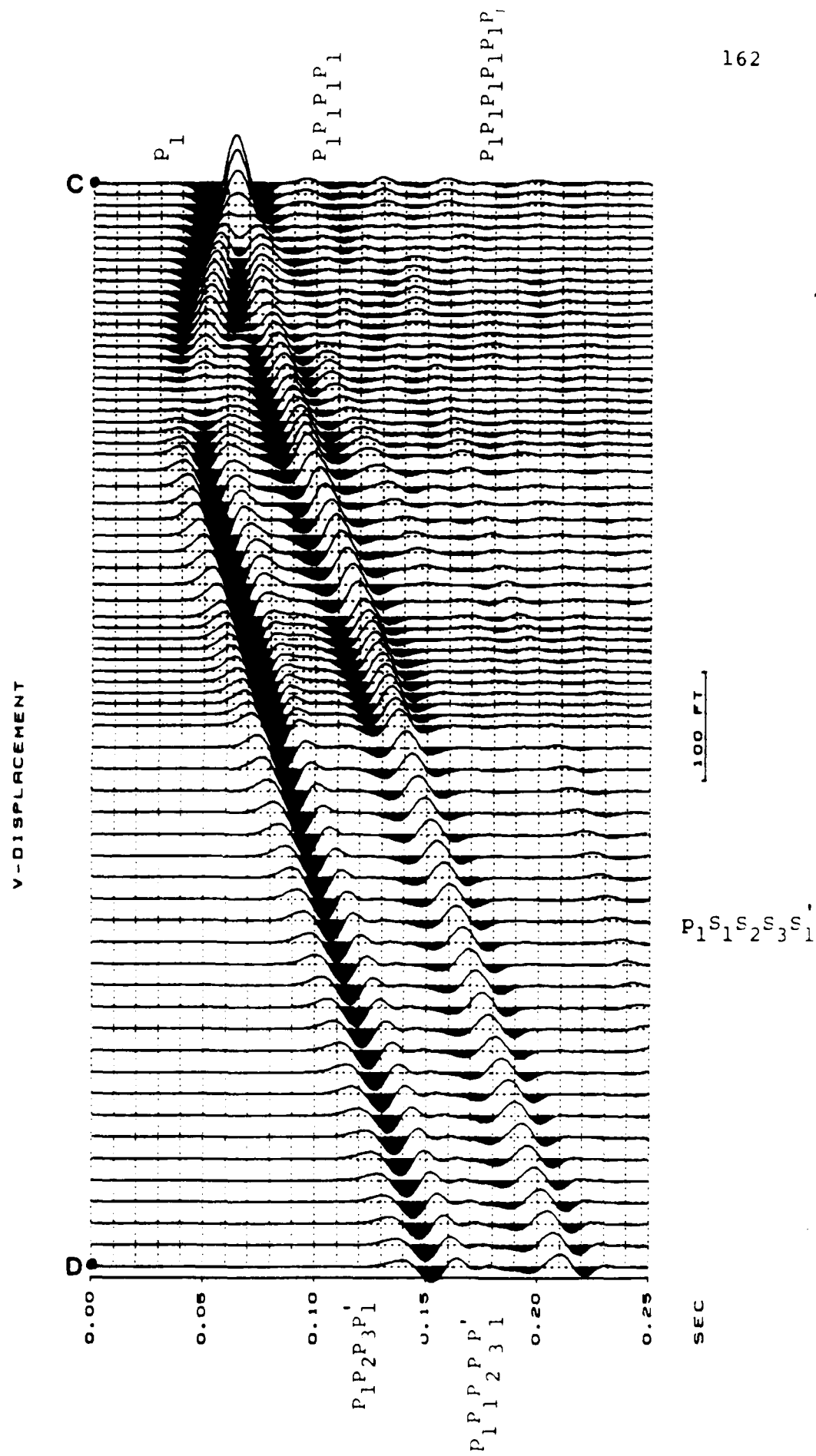
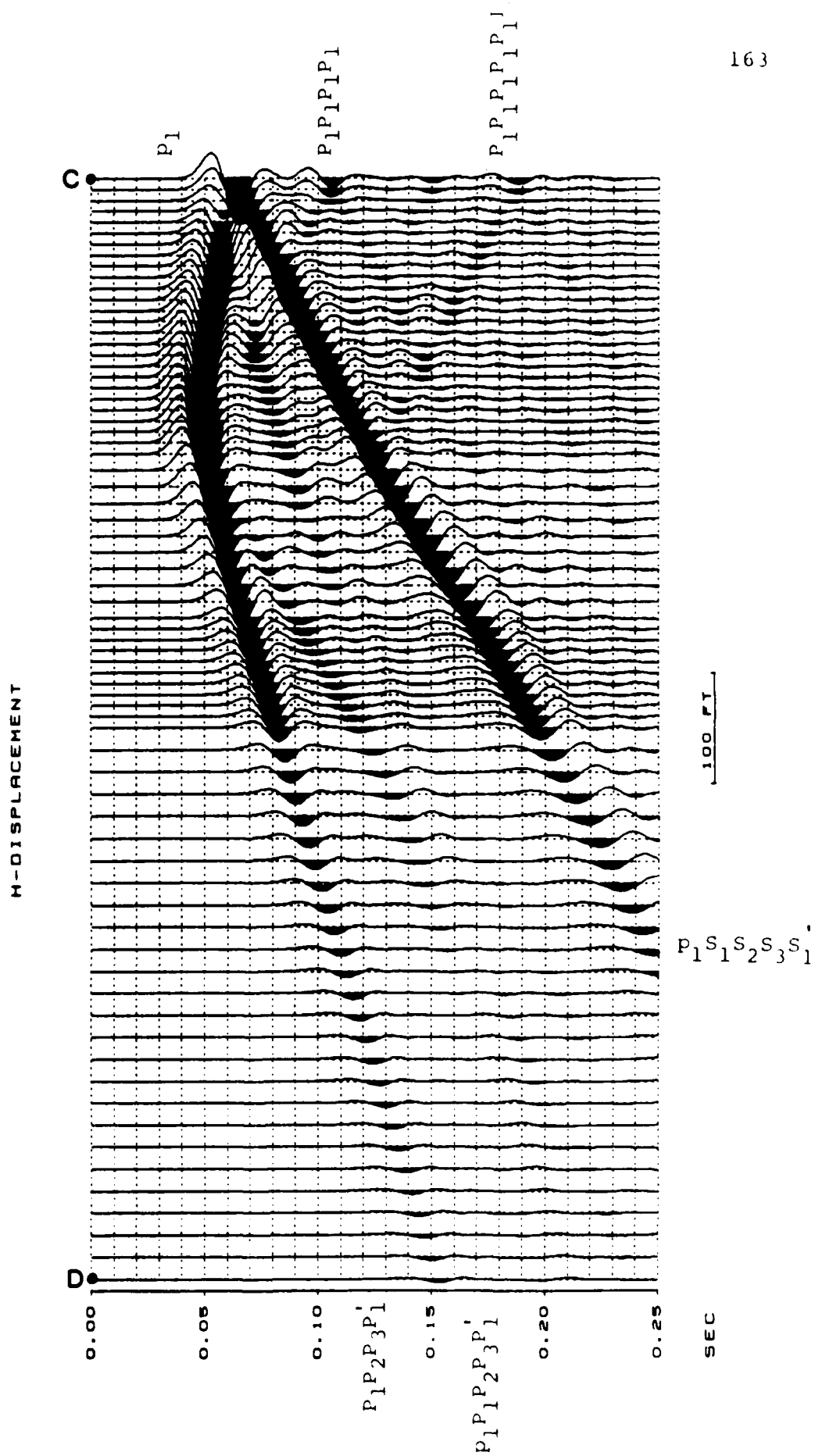


FIGURE 7-B. SYNTHETIC SEISMOGRAM ALONG VERTICAL PLANE CD
SUBJECTED TO AN OMNI-DIRECTIONAL LINE SOURCE



(2) because of CD is very close to OA, the vertical displacements of S waves are small and not clearly identifiable in either Figures 4-A or 7-A.

Comparison of Figure 4-B with Figure 7-B, the horizontal-components of the displacement due to VFS and OLS, shows that:

- (1) S waves are easily identifiable for both VFS and OLS.
- (2) S waves are stronger for VFS than these for OLS.
- (3) p_1s_1 and p_1p_1 are identifiable for OLS and only p_1p_1 is identifiable for VFS.
- (4) Mutiples, such as, $p_1p_1p_2p_3p_1'$, are quite clearly recorded for both VFS and OLS.

CONCLUSION

From the above results of the simulation of VFS and OLS, it is evident that seismic radiation patterns are strongly dependent on the nature of the source.

ACKNOWLEDGEMENT

The authors wish to express their deep appreciation to Dr. Kurt Marfurt, for using his snapshots subroutine, to Messers. Walter Brown, Ting-Fan Dai for their assistance in developing the plotting software.

The authors want to thank Mr. James Battis for his careful review of this manuscript. They again want to thank Mr. James Battis and also Dr. John Cipar of AFGL for their genuine cooperation and encouragement.

REFERENCES

Battis, J. C., "Seismic Velocity Models for Western Alluvial Basins" AFGL-TR-81-0139 Environmental Research Papers, No.740, ADA108153, 1981.

Honda, H., "Earthquake Mechanism and Seismic Waves", Journal of Physics of the Earth, 10(2): 1-97, 1962.

Kuo, J.T., Y.C.Teng, K.H.Chen, C.E.Shepherd, "Elastic and Viscoelastic Wave Scattering and Diffraction", Final Report of Air Force Contract F49620-77- 0139, 1981.

Kuo, J.T., and Y.C.Teng, Ground Response in Alluvial Basins Due to Seismic Disturbances, Scientific Report No.1, AFGL-TR-82-0279, ADA123683, 1982.

Kuo, J.T., and Y.C.Teng, Ground Response in Alluvial Basins Due to Seismic Disturbances, Scientific Report No.2, Air Force F19628-81-K-0012, 1983.

Lysmer, L., R.L.Kuhlemeyer, "Finite Dynamic Model for Infinite Media", J. Eng. Mech. Div., ASCE, 95, 859-877, 1969.

Smith, W., "A Non-Reflecting Plane Boundary for Wave Propagation Problems", J. Comp. Phys., 15, 492-503, 1973.

Zienkiewicz, O.C., The Finite Element Method- McGraw-Hill, Third Edition, 1977.

END

FILMED

2-86

DTIC